Using Infrared Spectroscopy and Ellipsometry to Study Fluorination and Ligand-Exchange Reactions During Etching of Oxides and Nitrides

by

Austin Mitchell Cano

BS in Chemistry, University of California Santa Barbara, 2015

A thesis submitted to the

Faculty of the Graduate School of the

University of Colorado in partial fulfillment

of the requirement for the degree of

Doctor of Philosophy

Department of Chemistry

2021

Committee Members:

Steven George

Sandeep Sharma

Niels Damrauer

Douglas Gin

Michael McGehee

Cano, Austin (Ph.D., Physical Chemistry; Department of Chemistry)

Infrared Spectroscopy and Ellipsometry Studies of Fluorination and Ligand-Exchange Reactions During Etching of Dielectric Materials

Thesis directed by Steven George

Over the last 60 years, the etching of materials has become a necessity for advancements in integrated circuits. As critical dimensions decrease it has become important to control the thicknesses of various features to the nanometer scale. Recently thermally based atomic layer etching systems have been developed for materials relevant for semiconductor manufacturing.

First, the fluorination reaction during the ALE of aluminum oxide with HF and BCl_3 is studied. Spectroscopic ellipsometry showed that the etch rate of Al_2O_3 can be controlled by increasing the pressure of the HF exposure. X-ray photoelectron spectroscopy (XPS) was used to model the fluoride thickness during HF fluorination and found good agreement between the fluoride thickness and etch rate. IR was also used to monitor the conversation of aluminum oxide to aluminum fluoride.

Etching of ALD grown AlN was done with sequential exposures of HF and BCl_3. Infrared difference spectra argued for fluorination and ligand exchange reactions. Single-crystal AlN was etched by XeF_2 and static exposures of BCl_3. XPS was used to monitor the Al 2p region as well as surface contaminants. Quadrupole mass spectrometry (QMS) was also used to study the volatile etch products. $AlCl_3$ was seen with BCl_xF_y compounds. The etching of Al_2O_3 was

investigated with HF and BCl_3. The etching of Al_2O_3 was observed using infrared spectroscopy. Initial exposures of BCl_3 showed a conversion reaction from Al_2O_3 to B_2O_3 but further cycles showed fluorination-ligand-exchange. QMS results showed the etch product $AlCl_3$ when cycling HF and BCl_3.

Spontaneous etching of B_2O_3 and TiO_2 are studied as well. IR was utilized to monitor the ALD growth of B_2O_3 with BCl_3 and H_2O. Etching was seen with sequential HF exposures. IR spectra during B_2O_3 etching showed there was B-F on the surface. B_2O_3 was able to be spontaneously etched down to 40ºC. Theory predicted etching at temperatures down to 110K. QMS studies observed BF_3 as the main volatile etch product. TiO_2 ALD was done with $TiCl_4$ and H_2O. Etching was seen at temperatures of 100ºC and greater. Surface Ti-F bonding was seen during the spontaneous etching. QMS showed TiF_4 was the main product during etching.

"*Big things are accomplished only through the perfection of minor details"*

-John Wooden

ACKNOWLEDGEMENTS

No one can finish the long journey to a PhD without the help of many people. There are too many people that have helped me in scientific ways and outside of academia to name. The first person I would like to acknowledge is my advisor, Steven George. Steve provided a great deal of support with the trials of graduate school. Steve has worked tirelessly to adapt to changing projects and funding while still finding time to work through the complicated chemistry with me. We have had many off-topic discussions and he has taught me many things about science and life that I will never forget. We have navigated fires and pandemics together and I can't say enough about the positive experience I have had with him as an advisor and for all these things and more I want to say thank you to him. I would like to thank Andrew Cavanagh. Andrew has become a necessity for our group at this point. He seems to have the answer to any question you might want to ask and always focuses on teaching so that we can understand what's happening. Also, for candy on Halloween and for nice discussions over the entire course of my work at CU.

I feel lucky to have been in the George group. I met many people that have made my thesis work feel fun and met many friends along the way. Thanks to Jaime Dumont who taught me how great a technique infrared spectroscopy can be. Thanks to Dave Zwyotko, Nicolas Johnson, and Tyler Myers for their friendship and for our crazy conversations on chemistry. Thanks to Jasmine Wallas for her friendship and all her podcast recommendations. Thanks to Diane Lancaster, Joel Clancy, Jonas Gretsch, Aziz Abdulagatov and, Younghee Lee for all they taught me with regards to atomic layer etching and other scientific topics. Thanks to Jessica Murdzek for putting up with all my questions about running and our many conversations leading

up to our calls with sponsors. I want to thank Eric Matson and Scott Clendening for being great sponsors of my work. Thanks to Simon Elliot and Suresh Natarajan for both being patient with me and their great work on the spontaneous etching of TiO_2 and B_2O_3. I would like to thank Matthew Bohn, all the EH&S crew, Jack Gaston, and the rest of the Chemistry Department management as they are all great people that have helped me on my Ph.D. journey.

Fortunately, I did not spend every minute thinking about atomic layer processing. Boulder has really turned into a home for me. I have been lucky enough to meet many people that I will always be friends with. I want to thank my friends Ryan K., Jesse, Nathan, JP, Christian, Alexa, Nikhar, Megan, Allie, Liz, James, Ryan D., Kate, and many more people that have influenced me throughout my time in Colorado. Without you all, my graduate work would not have been the same. I want to thank my ultimate frisbee team STMP, for being so welcoming to a transplant and for allowing me to overthrow people for 5 years. I especially want to thank my captains Nate Kenyon and Laura Johnson. You both are the best captains a chemist could ask for. I want to thank my parents and my sisters, Erica, and Heather, for all their help my entire life. Your love and support have influenced me in so many ways.

Lastly, I wanted to thank a very special thanks to my fiancé Lilly Bakker-Arkema for her unbelievable support of my PhD and for being the best friend a nerd can ask for. None of this would have been possible without her. I love you and I'm excited about our life together!

Table of Contents

LIST OF FIGURES

Introduction: Atomic Layer Processing

1.1 Etching

The idea of etching has been around for thousands of years and has been one of the most influential techniques for pattern creation. One of the first examples of etching can be traced back to the ancient Egyptians where hieroglyphics were created by carving into stone with primitive tools. This is etching because these Egyptians are removing material. Other examples of etching include wood engraving, metal etching, and wet chemical etching. Within the last 40 years, vapor phase etching (or dry etching) has become an important part of semiconductor manufacturing.[1-2] Plasma etching is among the most important etching techniques in history.[2]

The advancement of plasma etching can largely be attributed to the advancement of the integrated circuit. In 1965 Gordon Moore postulated that the number of transistors on a chip would double every two years.[3] This law has been amazingly true, all the way to 2021. The first integrated circuit made by Robert Noyce had only a few transistors on a chip in 1959. Now the same sized chip has billions of transistors. This has been due to the ever-decreasing node size, improving material properties, and changing architecture of devices.[3] To decrease the size of the transistor, etching and deposition techniques are needed to become precise in the removal and addition of material.

Plasma etching defines many of the features in the integrated circuit.[4] These plasma etching processes have been used to define many features due to the anisotropic nature of the technique. This means that nanoscale patterns can be created with the use of masks and anisotropic etching. Plasma etching was developed to replace wet chemical etching processes which used environmentally harmful solvents. Plasma processes began by flowing a process gas over a grounded wafer and applying an RF bias on an electrode which formed a plasma.[5-6] This

type of technique is known as reactive ion etching or RIE. This originally was all motivated to remove wet chemical solvent waste, but as critical dimensions decreased and the need for very selective etching techniques and anisotropic etching processes demanded the use of dry plasma etching. [4]

What RIE lacks is atomic layer control of how much material is removed, limitations on etching uniformity across a wafer, the introduction of surface roughness, and changes in surface composition.[4-5, 7-8] The need to combat these downfalls of classical plasma etching drives the research on atomic layer etching (ALE) processes. An ALE process requires self-limiting reactions done sequentially so that continuous etching does not occur. To achieve this a first half-reaction involves self-limiting modifications of the surface followed by removal of the modified layer. One example of this is silicon ALE where after an initial chlorination of silicon a low-energy plasma can remove the silicon chloride and thus an extremely thin amount of material is removed.[1-2]

No matter the field, technology has been driven by the demand for the size of devices to decrease, while the power of those devices to increase. This has led many fields to self-limiting atomic-scale processing techniques. Self-limiting is not always necessary, but control of thicknesses and material properties typically is. Self-limiting processes can sometimes be advantageous due to having thickness control built into the chemical nature of the technique. Two such techniques that meet these requirements are atomic layer deposition and atomic layer etching.

1.2 Atomic Layer Deposition

Atomic layer deposition (ALD) is a deposition technique based on sequential self-limiting surface reactions. Due to the self-limiting nature of each of the reactions in an ALD

cycle, a continuous and smooth film can be achieved. ALD commonly will consist of two different half-reactions that make up one ALD cycle. Each one of the chemicals used in the half-cycle requires self-limiting behavior and thus chemical selection is important. A representation of an ALD cycle is presented in Figure 1-1. The **A** half-cycle can react with the cone shaped void left in the surface. After the **A** chemical reacts with this surface it leaves new sites terminated on the surface that the A chemical can no longer react with. This would represent the self-limiting of the **A** half-cycle. The **B** half-cycle reacts similarly. The termination of the surface leaves a hole that the **B** chemical can react with until there are no more sites that the **B** chemical can fill. In between these exposures, there is a purge which removes all of the precurosor for the controlled chemical reactor. This would leave the surface terminated with the same groups that were there before the first A exposure. This represents one ALD cycle.

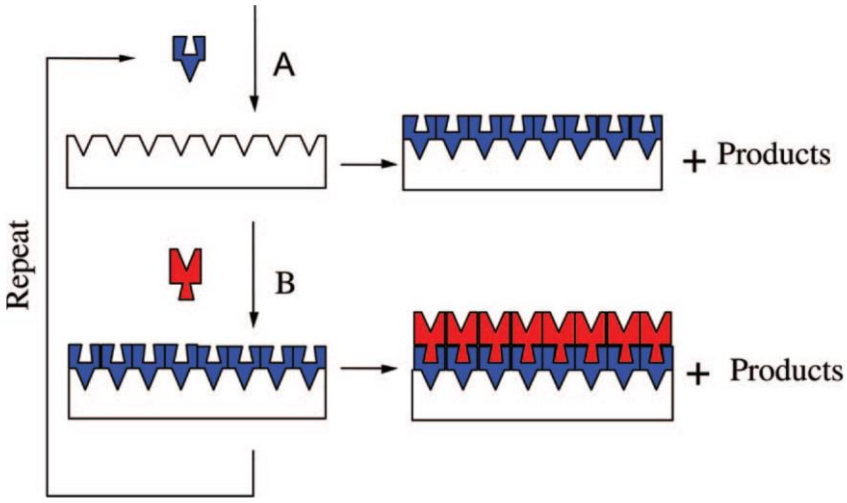

Figure 1-1: Schematic of an entire ALD cycle where after each half-cycle the precursor is unable to react with the surface termination[9]

ALD is typically done in a vacuum chamber. This is a chemical reactor where a mechanical pump removes most of the gasses to have a controlled environment. An ALD cycle starts in a chamber with a pressure on the order of 1 Torr (~0.001 atmospheres). Firstly, the A precursor is exposed to the deposition substrate for some dose time. Following the exposure, a purge is required. Typically, with a purge gas that helps remove any leftover A precursor so that the following B reactant will not react with A in the gas phase. Then the B reactant is pulsed into the vacuum chamber, is let to react with the substrate after which a second purge is required. There are many different process variables that go into successful ALD such as substrate temperature, chemical vapor pressure, vacuum pressure, purge gas, reactant exposure, and many more.

The model system for ALD is the deposition of aluminum oxide with trimethyl aluminum and water. Typical substrates are often initially terminated in hydroxyl groups due to atmospheric water. This is a good place to start for aluminum oxide ALD. The surface hydroxyl groups first react with the methyl groups in TMA.

$$Al(CH_3)_{3(g)} + -OH^* \rightarrow -OAl(CH_3)_2{}^* + CH_{4(g)}$$

Where (*) denotes a surface group. Once the hydroxyl group is consumed, subsequent TMA molecules will not have any reaction site and will leave the surface without reacting. This is what makes ALD reactions self-limiting. The second part of this ALD chemistry is the water exposure. Now that there are methyl groups terminating the surface when water is pulsed into the reactor, it can react with the methyl termination to make methane and recreate those hydroxyl groups that were on the surface originally. This reaction can be understood schematically in Figure 1-2.

$$-OAl(CH_3)_2{}^* + H_2O_{(g)} \rightarrow -OAl(OH)_2{}^* + CH_{4(g)}$$

Atomic layer deposition is important and has been used in transistor design more frequently thanks to the extreme precision of the thickness change needed as well as the conformality and anisotropic nature of ALD. One example is the dielectric in both planar and FinFET designs. The larger the gap between the gate and channel in a transistor the higher the supplied voltage will need to be to create

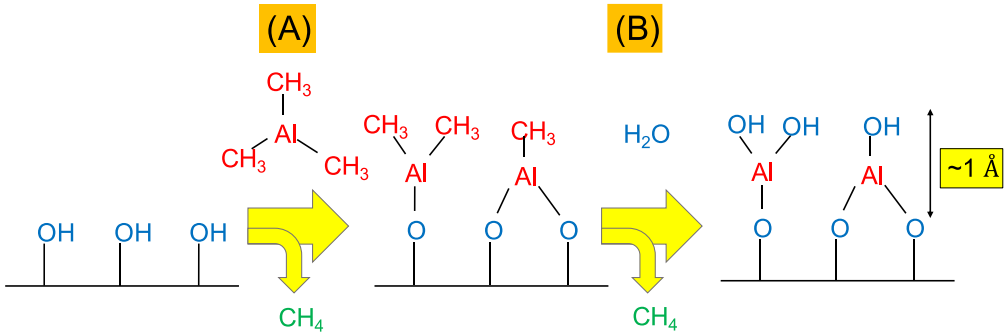

Figure 1-2: A schematic representation of a single aluminum oxide ALD cycle with TMA (A) and H_2O (B)

ALD is mostly considered an expensive deposition technique due to the conditions required and the very slow growth rates in comparison to other deposition techniques such as chemical vapor deposition and physical vapor deposition. ALD is used in most cases when a conformal thin film is necessary. This makes ALD useful in areas such as gate dielectrics, via fills, and in high surface area substrates. One area where ALD shines is in computer processor manufacturing. Figure 1-3 shows the increase in the usage of ALD and ALE systems in next-generation processors. Each generation of new and smaller processors from Samsung, TSMC, and Intel have more steps that involve ALD and ALE. When the node size was between 20 and 30nm there was not as much need for ALD systems. As the processors shrank to node sizes

below 10 nm ALD systems became increasingly important with the 10 nm Intel chip using approximately 70 different ALD steps during chip manufacturing.

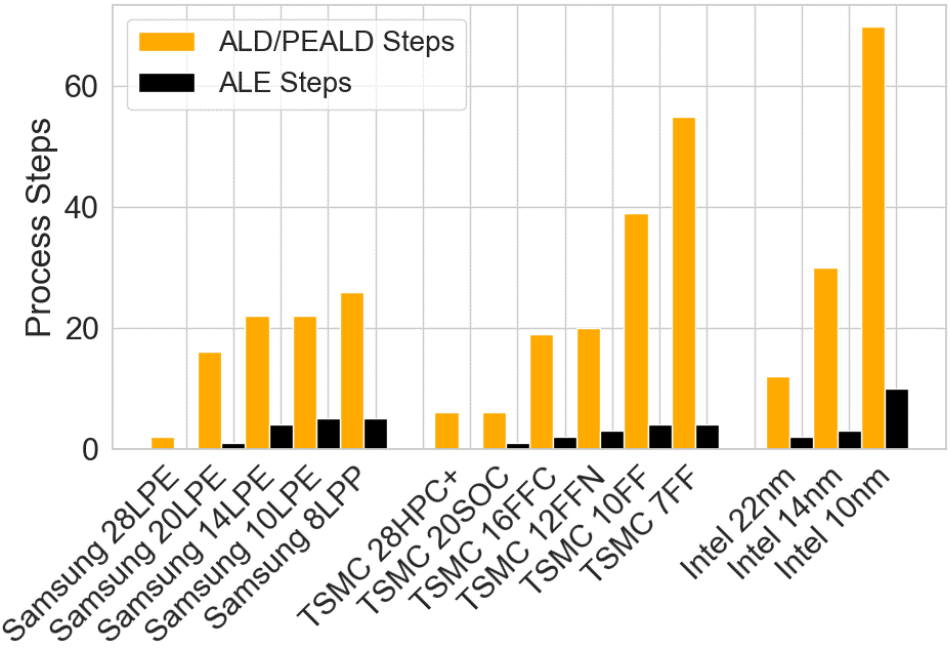

Figure 1-3: The number of ALD and ALE processes used in state-of-the-art processers from the three largest semiconductor manufacturers Samsung, TSMC and Intel (TechInsights)

1.3 Atomic Layer Etching

Thermal and plasma atomic layer etching is a still-developing process which has already begun to be used in chip production. Figure 1-3 also shows how ALE has emerged in recent chips. There were minimal steps that involved ALE processes when the node size was ~20nm but as the features decrease in size, ALE has begun to be utilized with approximately 10 different ALE steps in Intel's 10nm processors. As critical dimensions continue to decrease, it is likely that there will be more involvement of ALE systems in integrated circuit manufacturing. ALE is used currently to etch fin-type channels to desired thicknesses as well as cleaning the surface

after plasma processes. Understanding the capabilities of ALE systems has quickly become crucial as size constraints have demanded the deployment of atomic layer processes across the integrated circuit line.

Figure **1-4** shows how ALE systems have been more studied recently. In 1988 there were only a few manuscripts that described ALE systems.[1] The most important and early etching processes involved using plasmas as the energy source to drive etching reactions. Plasmas include neutral species (includes radicals), ionized species of the neutrals, and electrons. Plasma etching was critical in the invention and development of integrated circuits and now with decreasing feature size, plasma processes are key to driving some ALE reactions as well. All species in plasmas are in high energy states and can react with the etching substrate with many more reaction pathways than the chemical vapor form. These plasma species can make new bonds, and new interactions, with the surface that would otherwise be too unfavorable.

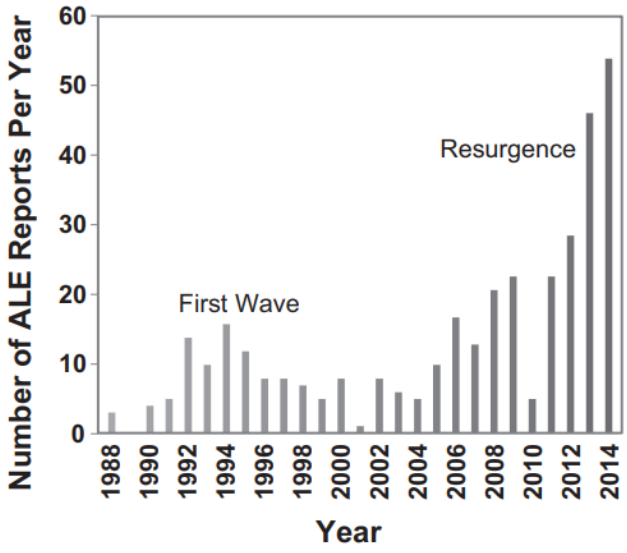

Figure 1-4: Number of ALE publications from 1988 to 2014[1]

Just as in ALD, atomic layer etching (ALE) also works under the principle of sequential self-limiting exposures surface reactions. ALE is sometimes coined as the reverse of ALD. ALE is typically done by introducing a surface modification reagent followed by a precursor which can react with the surface to create volatile products.[1, 10] Each one of the chemicals used in the half-cycle is mostly self-limiting because it is more difficult to modify the subsurface than the outermost surface. The co-reactant typically only reacts with the modification done in the first half-cycle. This creates a very controllable etching system.[11] Some ALE methods are based on plasma techniques that utilize sequential surface modification and removal reactions.[1, 11-12] The surface modification can involve surface chlorination or oxidation. The removal is accomplished with ions or energetic neutral atoms to obtain etching.[1-2]

In thermal ALE, the modification step is usually done by a fluorination reaction.[10] Hydrogen fluoride (HF) is the most used fluorination source due to its high vapor pressure at room temperature, and high reactivity with metal oxides. This fluorination chemistry is heavily discussed in Chapter 3. This fluorination can also be done with numerous other reactants such as SF_4, XeF_2, WF_6.[13-15] An alternative to the fluorination is chlorination with a reactant such as SO_2Cl_2 when the fluoride is either unstable or possible volatile. To remove the modified layer, a second chemical is then pulsed into the vacuum chamber. This second chemical is chosen to react with the modified layer to volatilize the fluoride. This is typically done by a ligand-exchange reaction where the ligands on the precursor can exchange with the surface fluoride to get multiple volatile products.

There have been other methods of achieving atomic layer etching. “Conversion-etch” chemistry was first shown in the etching of zinc oxide with hydrogen fluoride (HF) and trimethyl aluminum (TMA).[16] This involved the modification being done with trimethyl aluminum instead

of HF. The zinc oxide was first 'converted' to aluminum oxide by trimethyl aluminum before being able to fluorinate and then ligand exchange to remove the fluorinated material. Soon after another paper was published which showed a similar "conversion" reaction on silicon oxide.[17] Another method of etching, used in the etching of silicon and silicon nitride, was based on oxidation-etch where the surface was first oxidized to create a substrate that was then able to be etched.[18-19] While no thermal process existed for the etching of pure silicon or silicon nitride, the oxidation process allows for the use of previously studied ALE systems, in this case, SiO_2.

Aluminum oxide is a model system for thermal ALE. This system is done with HF as the fluorination source and trimethyl aluminum as the co-reactant. This process can also be seen on Figure 1-5. Firstly, HF is pulsed into the chemical reactor. This allows the initial surface to undergo a small amount of fluorination. The fluorination reaction can be represented with the balanced chemical equation:

$$Al_2O_{3(s)} + 6HF_{(g)} \rightarrow 2AlF_{3(s)} + 3H_2O_{(g)}$$

This reaction is pseudo-self-limiting as the thickness of the fluoride can be controlled by changing process conditions like the exposure time and temperature.[20] There is an initial fluorination followed by increase in the fluoride thickness which can be described as diffusion limiting. This is explored more in Chapter 3 and has also been studied in less depth previously.[20-22]

TMA is than used as the co-reactant. TMA can react with the AlF_3 surface to create volatile products. This was originally reaction is as follows:

$$AlF_{3(s)} + 2Al(CH_3)_3 \rightarrow 3AlF(CH_3)_{2(g)}$$

This was the original proposed reaction due to the expected volatility of $AlF(CH_3)_{2(g)}$ in comparison to $AlF_2(CH_3)_{(g)}$. To confirm this, mass spectrometry was done with TMA on an

AlF_3 powder. The resulting mass spectrum showed an abundance of dimers of aluminum, fluorine, and methyl groups.[23] This was primarily due to the stability of the dimer complex as well as the volatility.

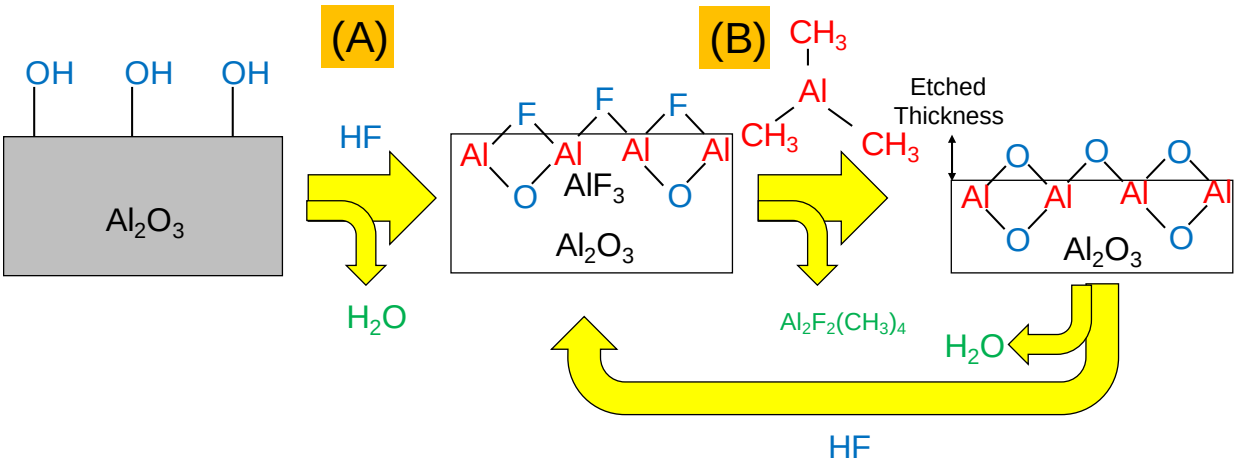

Figure 1-5: Schematic of aluminum oxide atomic layer etching where A) represents the fluorination of the surface, and B) which represents the ligand-exchange reaction that produces the volatile etch product

Thermal ALE has a few advantages over plasma-based ALE systems. Thermal ALE is completely isotropic, meaning that the etching rate is the same in all directions. Nanowire and nanosheet transistors are in development which requires etching and deposition in all directions. There are many steps in the backend of the line in IC development that will also require isotropic etching in high aspect ratio structures. Thermal ALE may also have other benefits such as smoothening surfaces,[2] using understood chemistries, metal etching,[12] high material selectivity and, removing damaged material from previous plasma steps.[24] A comprehensive list of thermal ALE systems can be found in Fischer et. al.[12]

To demonstrate the power of thermal ALE, the Jesús A. del Alamo group at MIT collaborated with the Steven George group at CU Boulder to create working transistor devices while using ALE as the tool for shaping device features.[25] Figure 1-6 shows a fin structure before and after 250 ALE cycles with HF and DMAC. Initially, the width of the Fin was 35nm in width. After ALE the fin was reduced to either 24nm or 4nm depending on the etched material. The etch rate differences are also important as selectivity in etching is often needed during etching processes.[24] This is an example of the promise and the power that ALE can provide in semiconductor manufacturing applications.

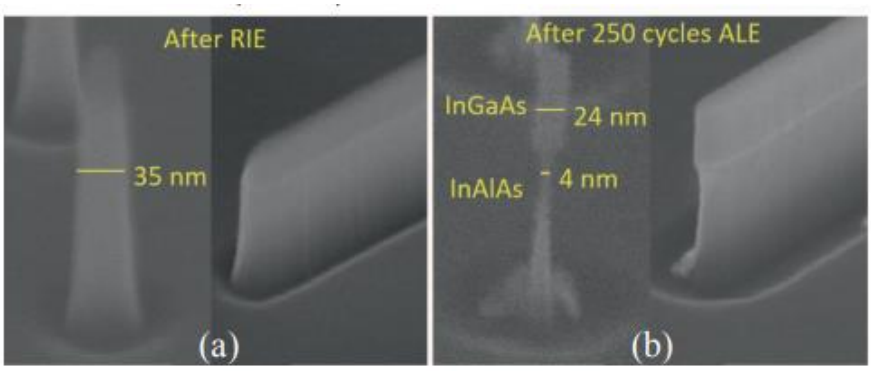

Figure 1-6: Image of a fin structure before and after 250 ALE cycles of DMAC and HF[25]

1.4 Introduction to modern integrated circuits

The fabrication of modern integrated circuits involves thousands of highly sensitive processes before a device can be packaged for use. There are nearly 10^{20} transistors made each year which is still not enough to satisfy the growing technological world. Now we buy cars, microwaves, and even toasters that are reliant on transistor fabrication, not to mention the ever-growing need for large-scale computing.[26] Since the first commercial transistor device there has

been a race for the development and deployment of newer and better processes to control all the different material properties inside an integrated circuit device. This miniaturization of devices has led to better thickness and material control during front end of the line transistor manufacturing. This is one area where techniques like ALE and ALD can shine as they are able to be controlled with extreme thickness precision.

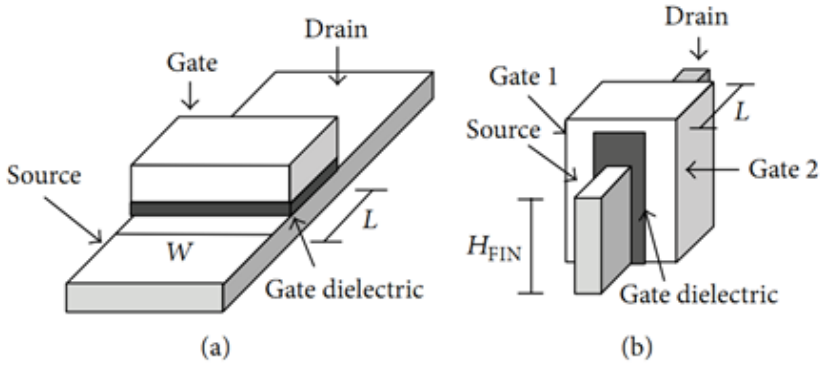

Figure 1-7: A) Design of a planar MOSFET and B) Design of the FinFET architecture[27]

A transistor is a device that can control the flow of current with an applied voltage. The basic planar transistor can be found in Figure 1-7a where there are three electrodes controller current flow. These three electrodes are called the source, where the electrical current comes from, the drain, where the electrical signal goes, and the gate which controls whether current flows from the source to the drain. In a MOSFET, the M stands for the gate metal, O for the oxide dielectric and, S for the silicon semiconducting channel material. The transistor is the most important region which lives in the integrated circuit. As seen in Figure 1-7 there are many parts to an operational MOSFET. The fabrication of these devices involves many steps of deposition, etching, and lithography. The basic principle is that when a voltage is applied to the gate electrode that is above a threshold voltage, the resulting electric field can modify a bit of the

underlying silicon's electronic properties to allow for a current to flow from the source to the drain. The dark layer in Figure 1-7a is called the gate dielectric and is what stops any electric short from the gate to the source or drain or the channel. This dielectric material was silicon oxide, due to the ease of creating silicon oxide on a silicon wafer but has changed to an atomic layer deposited high dielectric material such as hafnium oxide.[26, 28] The goal for a long time was to reduce the dimensions of all these components to increase the number of transistors per area. While decreasing transistor dimensions is beneficial for aspects like power consumption and processing power another way is to change MOSFET architecture. FinFETS describe a novel way to decrease transistor size and decrease the threshold voltage of the gate electrode.[26] This is shown in Figure 1-7b. The key advantage is decreasing the size of the channel while also having great control of the electric field in the channel. The jump to the third dimension does introduce the need for isotropic atomic layer processing techniques such as ALE and ALD.

Thicknesses of the front end of the line processing is so important, the node size is synonymous with the generation of technology. The state-of-the-art transistor technology is a 3-D architecture created by IBM which utilizes silicon in the form of nanosheets as the silicon channel. A cross-sectional transmission electron microscopy image can be found in Figure 1-8. This gives the gate electrode ultimate control of the electric field inside the silicon channel. These device structures are difficult to create and utilize more isotropic processes than the FinFET and planar MOSFETs that have come before it due to the gate dielectric needing to surround the channel. These complicated device architectures will require isotropic processes that can deposit and etch semiconductor-relevant material with unparalleled control.

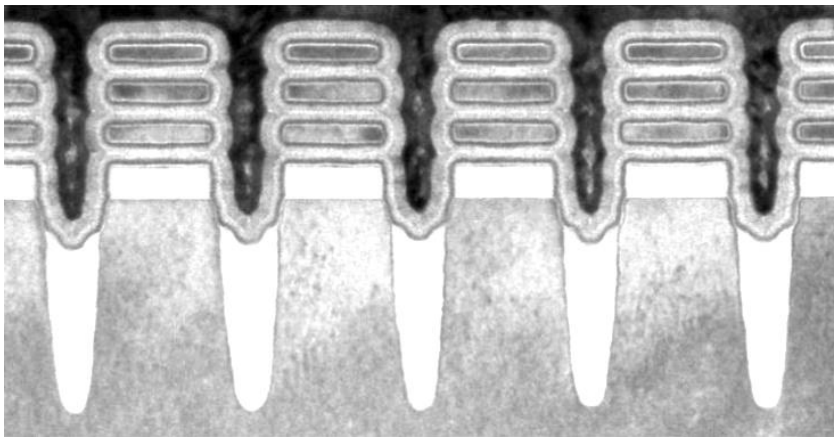

Figure 1-8: Transmission electron microscopy image of a novel transistor architecture showing trigate structures and is described as the world's first 2 nanometer node [29]

1.5 Statement of Purpose, Outline

The goal of this thesis is to help further understand atomic layer etching systems by employing in-situ techniques or ex-situ techniques that will help give more chemical information. When thermal atomic layer etching was first being explored, the goal was often to see if something was etched or not. Was there a loss of thickness? Was there a mass loss? This gave initial throughput and started to create a database for what could and could not be etched. In some initial studies, the mechanism behind ALE reactions was also explored. This thesis will hopefully extend the understanding of etching systems by utilizing many different techniques in unison. To obtain infrared difference spectra, ellipsometry thickness changes, volatile etch products and surface chemical composition gives a full understanding of what is happening during the etching.

In Chapter 2 I give an overview of the main techniques used in my thesis work. This will go over working principles and reactor designs for in-situ infrared spectroscopy as well as in-situ spectroscopic ellipsometry and x-ray photoelectron spectroscopy.

My first study in my graduate work was investigating the thermal ALE of aluminum oxide with HF and TMA. This has been done previously but the key to unlocking the full potential of thermal ALE is understanding the fluorination reaction. In Chapter 3, the focus will be on the understanding of the fluorination reaction with an emphasis on how pressure and time affect the etching rate and the thickness of created fluorides.

Aluminum nitride ALE was also investigated with HF or XeF_2 and BCl_3. Boron trichloride is a promising precursor in thermal ALE as it may undergo conversion chemistry or ligand-exchange chemistry. There is good evidence for the ligand-exchange reaction being the

dominant pathway towards etching. BCl_3 was used with a fluorination source to etch both low- and high-quality aluminum nitride. This study is presented in Chapter 4.

HF and BCl_3 were also found to etch aluminum oxide. With aluminum nitride, there was good evidence of a ligand-exchange reaction but with aluminum oxide, initial exposures of BCl_3 show that there is more complicated chemistry involved. Although the etching pathway may be closer to fluorination and ligand exchange, the surface undergoes conversion chemistry on the surface, which was not expected based on thermochemical calculations. This reaction of BCl_3 on aluminum oxide as well as the ALE can be found in Chapter 5.

This thesis will also aim to develop new etching systems, like the spontaneous etching of TiO_2 and B_2O_3. There has been little to no literature on thermal spontaneous etching with fluorination sources. These reactions have enabled ALE systems by first converting WO_3 to B_2O_3 or TiN to TiO_2. It was important to understand the spontaneous etching reaction pathway and volatile etch products of this reaction. In addition, theoretical calculations and a simple theoretical framework were created to predict how HF reacts with metal oxides and metal nitrides. The work on B_2O_3 spontaneous etching can be found in Chapter 6 and the TiO_2 spontaneous etching can be found in Chapter 7.

To understand these novel etching pathways infrared spectroscopy is utilized. Fourier Transform Infrared Spectroscopy (FTIR) has the unique ability to monitor growth and etching by assigning bulk vibrational modes as well as surface features. The changes in the bulk vibrational features can show growth and etching of thin films, while changes in other vibrational modes can show the role each individual precursor used in etching is.

Spectroscopic ellipsometry (SE) is also utilized to measure film thickness changes and optical property changes during etching. This allows for the ability to monitor absolute thickness

changes during etching on planar substrates. In-situ ellipsometry also allows for the monitoring of thickness changes of substrates deposited by high-quality deposition techniques, such as MOCVD,[6] where FTIR etching experiments were solely done on ALD grown films.

Over the course of the last 6 years, I have had the opportunity to study a wide variety of etching systems and a few deposition systems. I have looked at the etching of Al_2O_3, AlN, VO_2, ZnO, ZrO_2, B_2O_3, SiO_2, SiN, TiO_2 and, GaN as well as the deposition chemistry of TiO_2 AlN, B_2O_3, VO_2, ZrO_2, ZnO, and Al_2O_3. Each one of these systems has a unique behavior when it comes to modification (fluorination/conversion) as well as ligand-exchange (or spontaneous etching) reagent. In-situ FTIR with spectroscopic ellipsometry, x-ray reflectivity and, x-ray photoelectron spectroscopy, we have been able to understand complex chemistry in many etching systems.

Experimental Methods

2.1 Introduction

The goal of this section is to inform the reader about the various techniques used in this thesis. Each section will give a brief introduction followed by some comments about important equations and understanding the technique from a user's perspective. The overarching technique used in this thesis is Fourier Transform Infrared Spectroscopy (FTIR). This technique can give chemical bonding information during ALD and ALE reactions. Spectroscopic ellipsometry (SE) is a technique that specializes in understanding nanoscale thickness changes and optical dispersion in thin films. X-ray photoelectron spectroscopy (XPS) is used frequently to understand the chemical environment that different elements are in. XPS can also give compositional information to show film purity and possible contaminants during some deposition or etching process.

2.2 Fourier Transform Infrared Spectroscopy

The absorption of infrared radiation in molecules leads to vibrations of the various bonds in that molecule or surface. To study the wide array of vibrations in molecules, infrared spectroscopy is often utilized. Infrared spectroscopy is a spectroscopic technique that measures the absorption of infrared radiation to analyze sample composition all non-destructively.[30-31] This had wide-ranging applications from food safety, to pharmaceuticals, to semiconductor quality assurance, or forensic science.[30] Most of these applications utilize infrared spectroscopy to analyze samples for possible contamination that could yield a product unusable or unsafe. This thesis will focus on infrared spectroscopy and its ability to see changes in the surface termination

and changes in the bulk absorbance of thin films, during the deposition and etching of various materials.

The foundation of infrared spectroscopy lies in a bond's absorption of infrared radiation, transferring the energy from a photon to a bond's vibration. When the frequency of the photon matches the resonant frequency of the bonds vibration an absorption event can occur. By measuring the absorption of a sample at many different wavelengths, a spectrum can be created which shows a samples absorption (or transmission) of light across the entire mid-infrared spectrum. There have been many published books and articles describing the absorbance of light for many materials. By matching the absorption seen in your sample with the absorption of studied materials, a conclusion can be made about the composition of the sample in question.

Infrared spectroscopy is a great way to investigate chemical bonds on surfaces during thin-film processing. Most chemical bonds have a vibration between 200 cm^{-1} and 4000 cm^{-1}. When looking at an infrared absorbance spectrum, a peak indicates the presence of a chemical species that has a vibration at that frequency. The vibration of a chemical bond is much like the vibration of two masses connected by a spring. A chemical vibration can be estimated by Hook's law:

$$\nu = \sqrt{k/\mu}$$

Where ν is the vibrational frequency, k is the force constant, and μ is the reduced mass which is equal to $\mu = m_1 m_2/(m_1 + m_2)$ where m_1 and m_2 are the masses of the respective atoms. In general, as the masses of m_1 and m_2 increase, the frequency of the infrared vibration decreases. The force constant, k, describes the bond strength, or bond "stiffness". One important criterion necessary to absorb infrared light is a change in the dipole moment of a molecule as you change the nuclear coordinates of the vibrating atoms. For example, a molecule like O_2 does not have a

net dipole change as you change the locations of each oxygen atom. While this limitation does not often affect spectra of solid-phase materials it is still an important note to consider in vibrational spectroscopy.

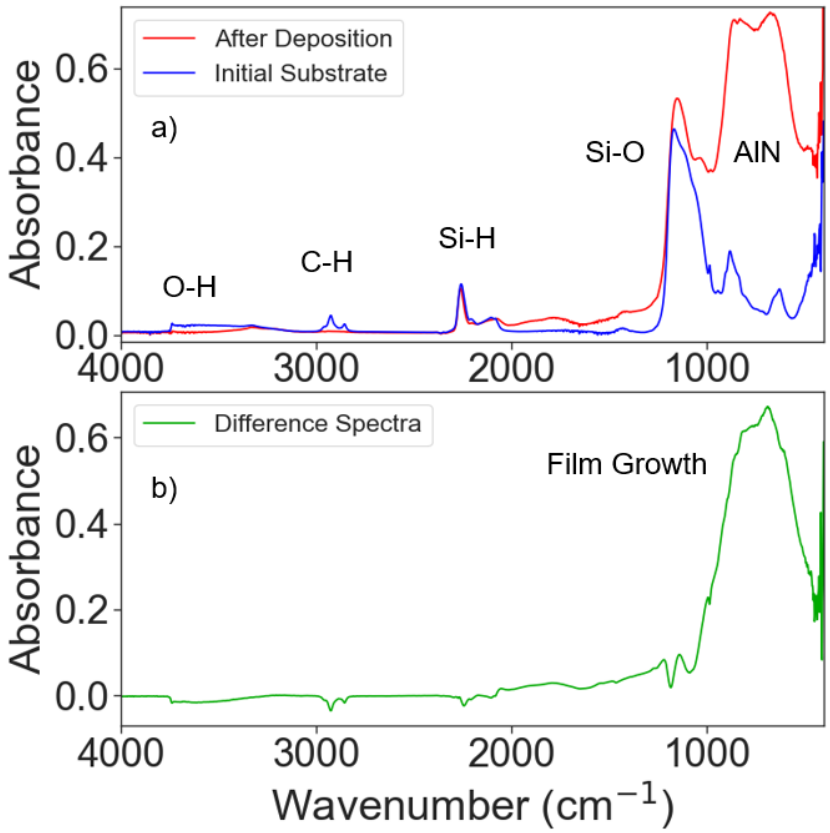

Figure 2-1: An example of the silicon substrate used in this thesis along with the spectra after a deposition (a) along with the difference spectra between these two spectra (b)

An example of the silicon substrate used in this thesis is presented in Figure 2-1a along with an example deposition. The blue line is a representative silicon substrate. Here we can see examples of vibrational features. There is a small increase in absorbance at 3700 cm^{-1} which corresponds to O-H stretching. This is expected because of the oxidized nature of many samples before a vacuum experiment is done. The O-H vibration is one of the most studied vibrational

features. The sharp onset of the O-H stretch is isolated O-H groups. The broad red shifting of the hydroxyl peak is due to surface-wide hydrogen bonding of O-H groups to each other.[32] Around 2900 cm^{-1} there is another grouping of peaks which is the C-H stretching of adventitious carbon on the surface. This is also something common among all substrates due to there being some carbon adsorbed on everything.[33] The multiple peaks represent different normal modes of the terminal -CH_3 species. These terminal groups on surfaces will often have narrow line shapes than species found in the bulk of materials. This can be a useful tool when analyzing what a peak environment may lie. At 2100 cm^{-1} there are two peaks that represent the different Si-H vibrations present on the silicon substrate. There are two peaks because some of the silicon here is back-bonded to oxygens and some are bonded to more silicon which creates a different frequency of vibration for the Si-H feature.[34] Finally, we have a large mode at 1200 cm^{-1} which is the LO phonon mode of silicon oxide.[35] A phonon mode is a frequency that is of a bulk solid, like that of a wave in an ocean, which all vibrates together. This Si-O feature is expected because the silicon nanopowder substrate is oxidized from the atmosphere before entering the vacuum chamber.

In Figure 2-1a, we can also see a spectrum taken after an aluminum nitride deposition. The resulting spectrum gives a large increase in absorbance centered at 650 cm^{-1} which is consistent with literature Al-N values.[36-37] When analyzing what features changed during a deposition or etching experiment (or even just half-cycles during those experiments) we can utilize difference spectra. To do this we use one spectrum as a reference, in this case, the blue spectrum, and subtract that from another spectrum that is taken after some treatment, the red spectrum. The resulting spectrum is shown Figure 2-1b in green. This difference spectra now only shows the change in the vibrational nature of the film without the spectra being disturbed by

the various other vibrational features that are unchanged. This allows for the analysis of slight changes in the spectrum.

A picture of the FTIR apparatus is shown in Figure 2-2. Figure 2-2a shows the reactor on the optics table. The precursor manifold on the right side of the image feeds into the main flow tube reactor surrounded by the custom white ceramic heater. The chemicals then flow to the pump and the exhaust. The left side of the image shows the infrared spectrometer. This is an IS-50R purchased from thermofisher. Figure 2-2b shows a diagram of the figure in Figure 2-2a. Infrared light is first generated in the spectrometer. This includes the light's initial creation by a Glow-Bar source, its path through the beam splitter and interferometer and, its exit from the spectrometer.[30] It is then reflected off a flat mirror before reflecting on a 3" parabolic off-axis gold plated mirror with a focal length of 8.1". This allows for the infrared red light to be focused on the powder sample. Before hitting the sample, the light passes through a KBr (or CsI) window which is kept clean during depositions with a gate valve. The light is then passed through the powder sample before passing through another KBr window. The light is focused again by a parabolic off-axis mirror with a short focal length which focuses the light on the MCT-B detector. The spectrometer as well as the external portions of the beam are purged with a purge gas, free of CO_2 and H_2O which are common infrared light absorbers. H_2O can also damage the infrared optics so keeping a positive pressure is key to the optics longevity. This purge gas is generated by a Parker purge gas generator which is fed by house air.

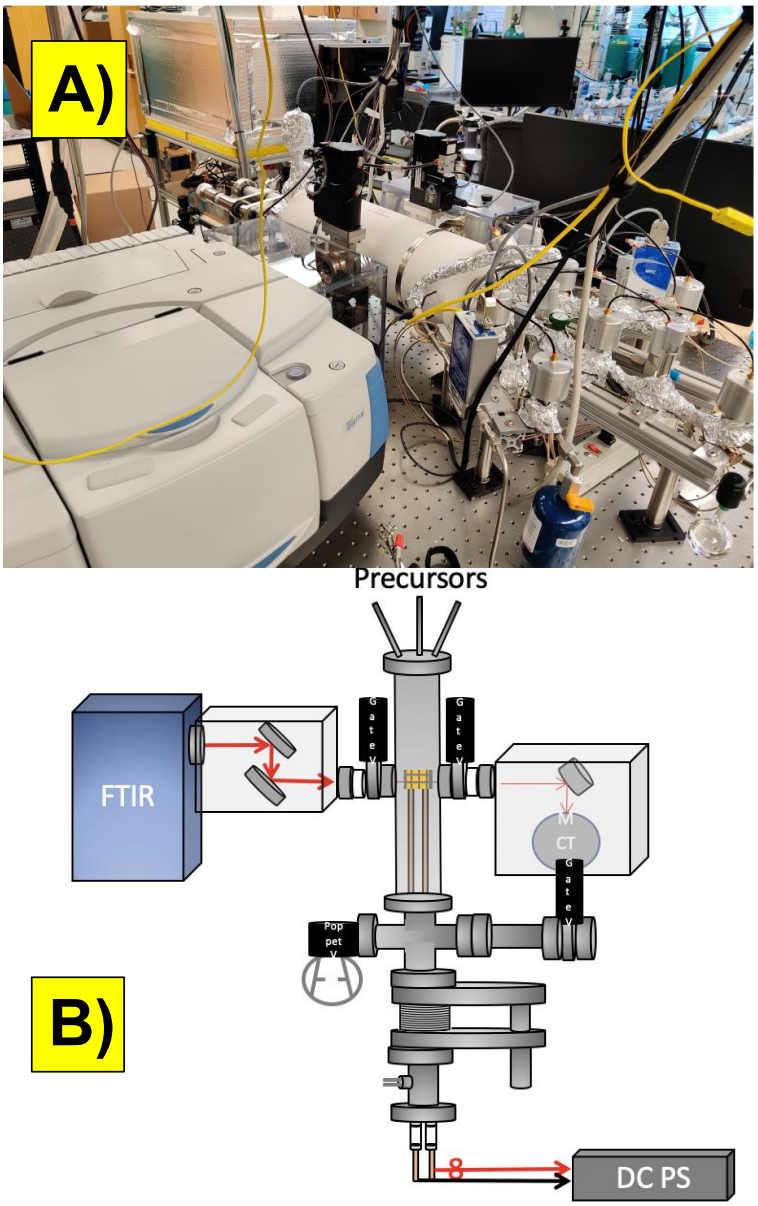

Figure 2-2: A) A picture of the *in-situ* FTIR apparatus used in these experiments and B) a cartoon of the top-down view of the FTIR apparatus

The sample can be heated in two different ways. The sample temperature is controlled by the ceramic heater and by a direct current power supply which can resistively heat the sample. Resistively heating the sample allows for temperatures above 800ºC to be reached. Due to the

gate valves which are very close to the sample, the sample must be cooled periodically so that the gate valves do not reach 204ºC. This power supply is a HP 6268B. The heating is controlled with an external PID 16B Love Controller. This heating was changed to a PID controller within the LabView virtual instrument which controls the rest of the process parameters during an experiment.

The powder is created in the setup described in Figure 2-3. First, a mesh grid is created by cutting out a tungsten mesh into a rectangle with rough dimensions, 1.7 cm by 2.8 cm. This grid has 5-micron spacings and 100 gridlines per inch. Tungsten was chosen for this due to its high chemical stability, thermal stability, and low resistivity. On the short ends of the sample, tantalum foil is spot welded on the tungsten grid. This allows for solid contact to the power lines which are connected to the DC power supply. Silicon nano-powder, purchased from US Research Nanomaterials, is then pressed into the grid using a die setup shown in Figure 2-3a. This die setup is then pressed using a large die press. The finished powder grid sample is then finished by adding an insulating epoxy (Cermabond 571) which has a type-k thermocouple attached shown in Figure 2-3b. This is the temperature reading that is used when controlling the DC power supply output voltage. The insulating epoxy needs to be cured at room temperature for a minimum of two hours then cured at a temperature of 120ºC for three hours. The second epoxy cure was always done in vacuum as well.

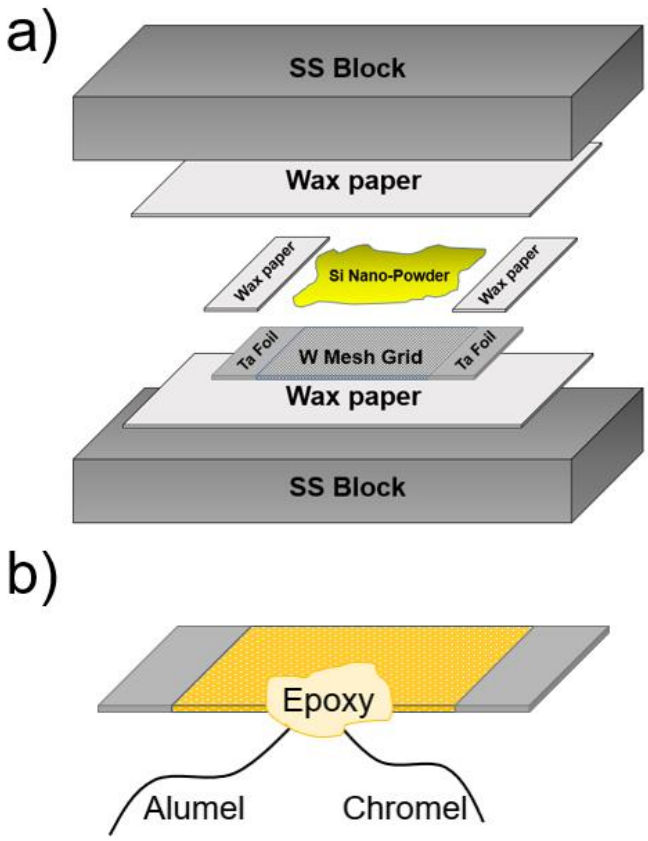

Figure 2-3: a) The setup for pressing silicon nano-powder into a tungsten grid and b) the sample after adding a thermocouple with expoxy to the sample.

One last note on infrared spectroscopy and the setup involved with its implementation here is the detector used. Figure 2-4 shows the wavelength range of various light sources and detectors. The mid to far infrared region which spans 4000 to 200 cm^{-1} or 2.5 microns to 50 microns which is where many chemical vibrations absorb light. The light source is simple in that the silicon carbide ceramic filament is the best white light for this region. This is what the Glow-Bar source filament. The two main detectors used in infrared detection is the mercury cadmium telluride (MCT) detector and the deuterated triglycine sulfonate (DTGS or commonly referred to

as TGS) detector.[31] MCT is a low band-gap semiconductor (~0.1 eV) so that when an infrared photon hits the detector there is an electron that is promoted from the valence band to the conduction band and thus creates an electrical current proportional to the intensity of the infrared light. MCT detectors have great sensitivity to infrared light but can saturate quickly, need to be liquid nitrogen cooled and cannot easily detect far-infrared light.[31, 38] DTGS detectors are room temperature detectors which can operate on the principle that infrared light hitting the detector will create a small change in the temperature of the material, which changes the dielectric constant and thus the capacitance which can be measured. These are cheap but very insensitive. DTGS detectors also can measure far infrared light when made with CsI windows instead of KBr windows. The far-infrared is something that will become useful as our understanding of ALE reactions becomes better due to the relevance of chlorine-based precursors and metal chlorine vibrational bands residing from 400-50 cm^{-1}.

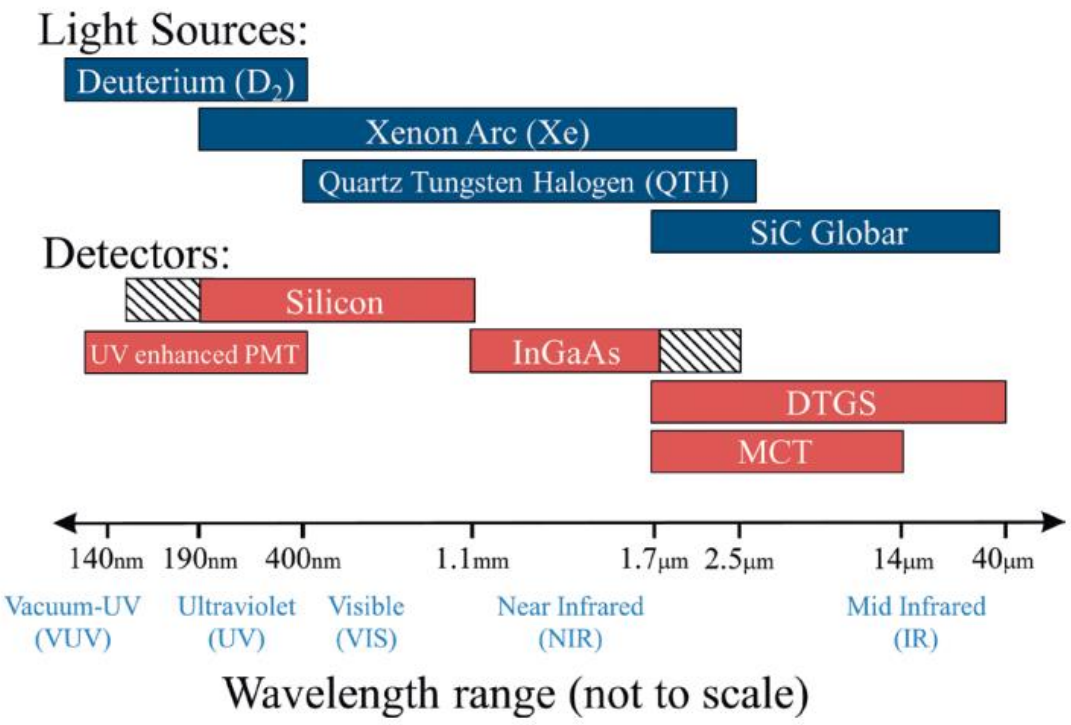

Figure 2-4: List of light sources and Detectors from ultra violet to mid infrared light Reproduced[39]

2.3 Spectroscopic Ellipsometry

When analyzing thin films, one important aspect is simply understanding the thickness changes during some thin-film process. One technique that has been heavily utilized in thin films processing is spectroscopic ellipsometry (SE). SE uses polarized light in the UV and visible range to measure the optical properties of surfaces. When polarized light interacts with surfaces it can change both the change in phase and amplitude of the polarized light. This will result in measured parameters Δ, the change in phase between p and s polarized light, and Ψ, the change in amplitude of p and s polarized light. When linearly polarized light encounters a surface, the polarization changes the light to elliptically polarized light. This is why it is called ellipsometry!

Figure 2-5 shows a diagram of the different parts inside an ellipsometer. Initially, the light is created by an ideal source. This ideal source is typically quartz tungsten halogen and deuterium lamps seen in Figure 2-4. The difference between other light-based techniques that can measure thickness and ellipsometry is that ellipsometry needs to measure not only the light intensity but also light polarization. In order to see the change in the polarization of light, the exact polarization needs to be known.[39] It be circularly polarized or linearly polarized but it just needs to be known. This is done by the polarization state generator, which filters the light through successive polarizers and compensators. When the light interacts with the sample, the polarization, and the intensity change. Now the ellipsometer must know the exact change in the polarization. It does this through the polarization state detector, which is a polarization analyzer. After which the light hits the detector where the intensity of the light is measured.

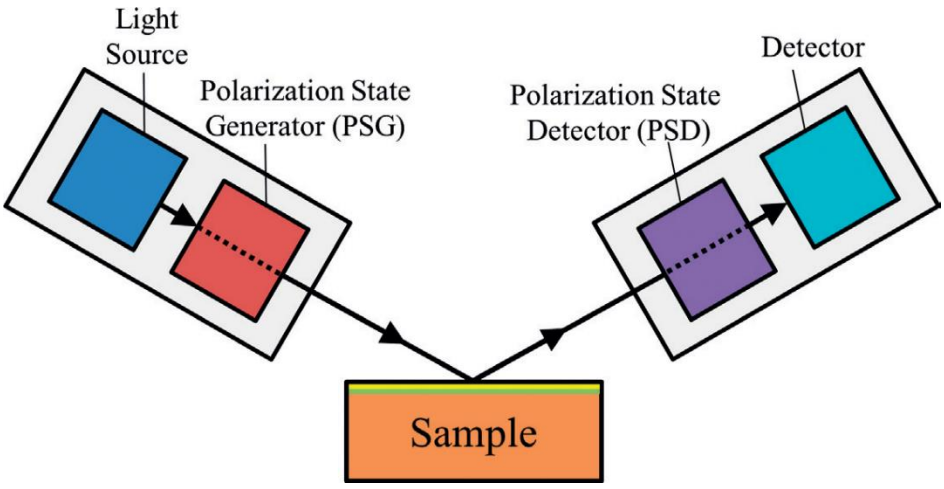

Figure 2-5: A Schematic of a typical optical setup in spectroscopic ellipsometers. [39]

There are also a variety of advantages in using SE for the investigation of etching and growth of films. Ellipsometry's main advantage is the ability to measure the thickness and

optical properties wavelength-dependent properties of multiple layers. This allows for the analysis of a stack shown in Figure 2-6a. There are a few layers here, including a roughness layer, an aluminum nitride layer, and a sapphire substrate in this example. We can use an SE (in this case it is a Woollam M-2000) to take Ψ , and Δ measurements at many wavelengths (this is what makes it spectroscopic) and produces the spectra shown in Figure 2-6b. Ψ and Δ are defined as $\Delta = \delta_1 - \delta_2$ where δ_1 is the phase difference between the wave parallel to the plane of incidence and the wave perpendicular in the incident light, and δ_2 is the phase difference between the parallel and perpendicular waves for the outgoing waves. Ψ is defined by $tan\,\Psi = \frac{|R^p|}{|R^s|}$ which is the tangent of the ratio in the reflectance of light parallel to the plane of incidence and the reflectance of the light perpendicular to the plane of incidence.

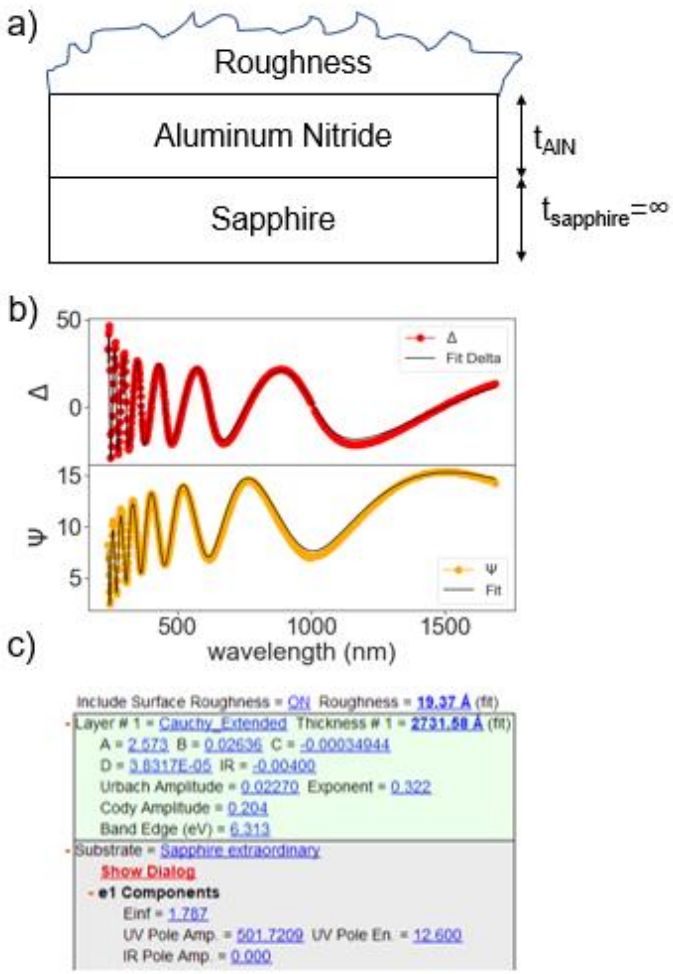

Figure 2-6: a) A diagram of a possible surface b) the ellipsometry measurements of the surface in a) and c) the model used to describe the material. This gives a small idea behind having an idea of the substrate to finding the optical properties of the film

The user can then carefully choose a model to describe the optical dispersion. Figure 2-6c shows a screenshot from the ellipsometry software CompleteEase, where a model has been chosen and the lines in Figure 2-6b have been fit shown in the black lines. SE modeling can calculate both the thickness of these layers and the optical properties of this layer stack in this example There are around two nanometers of roughness of an aluminum nitride film (modeled with a Cauchy layer with Urbach coefficients to help model the semiconducting nature of

aluminum nitride) with finally a substrate of sapphire. The index of refraction (n) and the extinction coefficient (k) for both the aluminum nitride and the sapphire are shown in Figure 2-7. Dielectrics like sapphire will always have an k value of zero, whereas due to aluminum nitrides bandgap at ~6 eV there is a non-zero value for k which increases as the wavelength of light gets closer to the aluminum nitride optical bandgap.

A diagram of the chemical reactor with in-situ capabilities used in this thesis is presented in Figure 2-8. Here we see a picture of the reactor in the real world on the top part of Figure 2-8. This shows the computer used on this tool on the left. On the right there is the light source which is at a 75^{o} angle relative to the surface normal. This light then travels through a quartz window and then is directed towards a substrate that is housed inside the vacuum chamber. The reflected light goes back outside of the vacuum chamber by passing through another quartz window and then hits a detector. There is a simple diagram of this reactor shown on the bottom. This tool can measure the optical properties and thickness changes of multiple layers without having to break vacuum to do so, enabled by the quartz windows and the gate valves protecting the windows during chemical exposure. This tool also allows for the thickness to be measured after each half-cycle during an ALE and ALD type reaction. This allows for angstrom level precision of etching rates and changes in optical properties during an experiment.

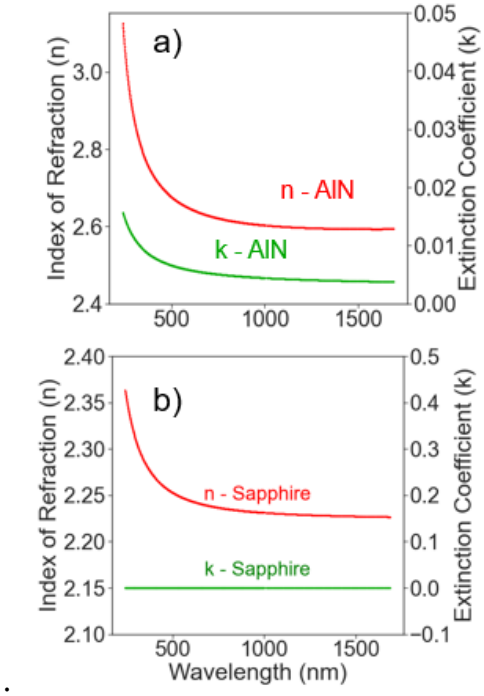

Figure 2-7: n and k values for a) aluminum nitride and b) sapphire associated with the layer stack and fitted optical properties in Figure 2-6.

The Woollam-M2000 spectroscopic ellipsometer is also a great choice for ellipsometry measurements due to its wide range of wavelengths used. Two lamps illuminate the sample, a deuterium lamp, and a quartz tungsten halogen lamp (QTH). These light sources can also be seen in Figure 2-4. The deuterium lamp can create light in the UV region. This accounts for the light from 230nm to 500nm. The rest of the spectrum uses the light from a QTH lamp which can emit light from ~400nm to 1800nm which spans the entire visible spectrum and the near-infrared spectrum as well. Having a wide range of wavelength measurements can help understand the film optical properties better and can be useful to allow for a wider range of fitted wavelengths to better understand your fitted models.

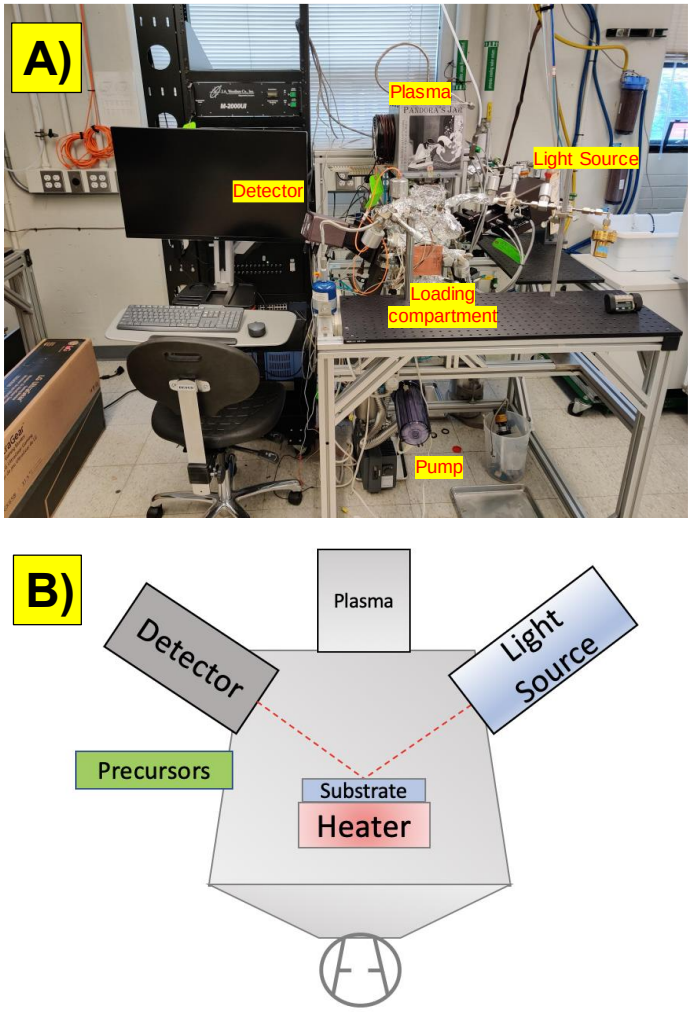

Figure 2-8: A) A picture depicting the reactor in use for all in-situ spectroscopic ellipsometry measurements and B) a cartoon of the in-situ setup

2.4 X-Ray Photoelectron Spectroscopy

X-ray photoelectron spectroscopy (XPS) is a technique that is capable of a great deal of surface information. This non-destructive technique can give chemical environment information sensitive to only to top 10 nanometers as well as compositional analysis. This can help understand not only what metals are in this film but also if they are bonded to oxygen or nitrogen

on fluorine and in what amounts.[20, 33, 40-42] XPS can tell you about not only the quantities of various elements but can give an idea about their chemical nature.[43]

XPS uses the photoelectron effect to obtain a spectrum of surface binding energies. First, a soft x-ray photon with defined energy and narrow energy line width is subjected to a surface. The x-ray interacts with core electrons and then emits them as per the photoelectric effect. This emitted electron is then analyzed for its kinetic energy. The difference between the energy in the incident x-ray and the kinetic energy of the emitted electron gives rise to peaks that resemble atomic core electron binding energies. This is represented with the equation:

$$E_b = \hbar \cdot \nu + E_k + \Phi$$

where $\hbar\nu$ is the energy of the x-ray, E_k is the kinetic energy of the emitted electron, and Φ is the work function of the detector. This way we can find the binding energies of core shell electrons as a function of the kinetic energy of the electrons that hit the detector.

There are many capabilities that XPS can also be utilized for such as peak fitting which can be useful for deconvolving metal fluoride and oxide peaks for example. Examples of this can be found in 3.4.1 and 4.4. There are many factors in which to be careful to not overfit in XPS such as the full width at half max (or sometimes σ in some distribution equations) or the ratio between the Gaussian content and Lorentzian content in a Voigt distribution. Commonly in this thesis, as well as in other literature, the background will be subtracted by using either a Shirley correction or a Tougaard correction.[43] There can be a lot of information in the background such as qualitatively where the element in interest is located in the film stack. Another ability in XPS is being able to use thickogram modeling to try to find the thickness of various films. A thorough example of this can be found in 3.4.2.[20]

Effect of HF Pressure on Thermal Al_2O_3 Atomic Layer Etch Rates and Al_2O_3 Fluorination

Austin M. Cano, Amy E. Marquardt, Jaime W. DuMont and Steven M. George

Department of Chemistry, University of Colorado, Boulder, Colorado 80309-0215

3.1 Abstract

Thermal Al_2O_3 atomic layer etching (ALE) can be accomplished using sequential fluorination and ligand-exchange reactions. HF can be employed as the fluorination reactant and $Al(CH_3)_3$ can be utilized as the metal precursor for ligand-exchange. This study explored the effect of HF pressure on the Al_2O_3 etch rates and Al_2O_3 fluorination. Different HF pressures ranging from 0.07 Torr to 9.0 Torr were employed for Al_2O_3 fluorination. Using *ex situ* spectroscopic ellipsometry (SE) measurements, the Al_2O_3 etch rates increased with HF pressures and then leveled out at the highest HF pressures. Al_2O_3 etch rates of 0.6, 1.6, 2.0, 2.4, 2.5 Å/cycle were obtained at 300°C for HF pressures of 0.17, 0.5, 1.0, 5.0, and 8.0 Torr, respectively. The thicknesses of the corresponding fluoride layers were also measured using x-ray photoelectron spectroscopy (XPS). Assuming an Al_2OF_4 layer on the Al_2O_3 surface, the fluoride thicknesses increased with HF pressures and reached saturation values at the highest HF pressures. Fluoride thicknesses of 2.0, 3.5, 5.2 and 5.5 Å were obtained for HF pressures of 0.15, 1.0, 4.0 and 8.0 Torr, respectively. There was an excellent correlation between the Al_2O_3 etch rates and fluoride layer thicknesses versus HF pressure. In addition, *in situ* Fourier Transform Infrared Spectroscopy (FTIR) vibrational studies were used to characterize the time

dependence and magnitude of the Al_2O_3 fluorination. These FTIR studies observed the fluorination of Al_2O_3 to AlF_3 or AlO_xF_y by monitoring the infrared absorbance from the Al-O and Al-F stretching vibrations. The time dependence of the Al_2O_3 fluorination was explained in terms of rapid fluorination of the Al_2O_3 surface for initial HF exposures and slower fluorination into the Al_2O_3 near surface region that levels off at longer HF exposures times. Fluorination into the Al_2O_3 near surface region was described by parabolic law behavior. The self-limiting fluorination of Al_2O_3 suggests that the fluoride layer on the Al_2O_3 surface acts as a diffusion barrier to slow the fluorination of the underlying Al_2O_3 bulk. For equal fluorination times, higher HF pressures achieve larger fluoride thicknesses.

3.2 Intro

Atomic layer etching (ALE) is based on sequential, self-limiting surface reactions that can remove material from surfaces with atomic layer control.[1] Some ALE methods are based on plasma techniques that utilize sequential surface modification and removal reactions.[1] The surface modification can involve surface chlorination or oxidation. The removal is accomplished with ions or energetic neutral atoms to obtain etching. These plasma ALE processes can achieve anisotropic etching. Examples of plasma ALE include Si,[44-46] Ge,[47] GaAs,[48] SiO_2,[49-50] HfO_2,[51] Si_3N_4,[52] graphite[53] and polymer[54] ALE.

Other ALE methods are based on thermal chemistry.[55] These thermal ALE processes are also performed using surface modification and removal reactions. The surface modification can be accomplished by surface fluorination or oxidation. For thermal ALE, the removal reaction is a thermal reaction such as ligand-exchange[55-56] or fluorination to a volatile fluoride.[57] These

thermal ALE processes can achieve isotropic etching. Examples of thermal ALE include Al_2O_3,[21-22, 55, 58-59] HfO_2,[28, 60] SiO_2,[17] ZnO,[16] TiO_2,[13] WO_3,[61] W,[61-62] TiN[57] and AlN[63] ALE.

Many thermal ALE processes are based on sequential fluorination and ligand-exchange reactions.[55-56] In this etching process for a metal oxide, the surface of the metal oxide is first fluorinated to form a thin metal fluoride layer on the metal oxide. [55, 59] Subsequently, the thin metal fluoride layer is removed with a ligand-exchange reaction.[55, 59] During this ligand-exchange reaction, a metal precursor accepts fluorine from the metal fluoride and concurrently transfers one of its ligands to the metal fluoride. The ligand-exchange reaction can produce reaction products from the metal fluoride that desorb into the gas phase. The sequential application of fluorination and ligand-exchange reactions progressively removes the metal oxide. This thermal ALE is viewed as the reverse of atomic layer deposition (ALD).[64-65]

Thermal Al_2O_3 ALE using HF and $Al(CH_3)_3$ as the reactants is an example of thermal ALE using fluorination and ligand-exchange.[22, 58] HF is known to fluorinate Al_2O_3 to form an AlF_3 or AlF_xO_y layer on the Al_2O_3 surface.[22, 58] The $Al(CH_3)_3$ then undergoes a ligand-exchange reaction with the fluorinated layer. $Al(CH_3)_3$ accepts fluorine from the fluorinated layer and donates methyl ligands to the surface. This ligand-exchange reaction allows the Al in the fluorinated Al_2O_3 layer to desorb as a volatile product. Recent quadrupole mass spectrometer studies have identified the etch product as $AlF(CH_3)_2$.[23] This etch product either appears as a dimer with itself ($AlF(CH_3)_2 \bullet AlF(CH_3)_2$) or with $Al(CH_3)_3$ ($AlF(CH_3)_2 \bullet Al(CH_{3)3}$).[23]

This study explored the effect of the HF pressure on the Al_2O_3 etch rate during thermal Al_2O_3 ALE and the Al_2O_3 fluorination. The Al_2O_3 etch rates were determined using spectroscopic ellipsometry (SE) measurements. The fluoride layer thicknesses were measured using x-ray photoelectron spectroscopy (XPS). The time dependence and magnitude of the fluorination of Al_2O_3 were also examined using Fourier Transform Infrared (FTIR) vibrational studies. These studies help to understand HF fluorination of Al_2O_3 during Al_2O_3 ALE and the effect of the fluorination thickness on the Al_2O_3 etch rate.

This study also complements previous theoretical and experimental examinations of the fluorination of Al_2O_3. Earlier theoretical investigations have studied the fluorination of θ-Al_2O_3 by HF using density functional theory (DFT) methods.[66-67] Recent theoretical investigations have also examined the fluorination of θ-Al_2O_3 surfaces by HF and compared the fluorination to measured etch rates during Al_2O_3 ALE.[68] Many experimental studies have also explored the fluorination of Al_2O_3 because of the effect of fluorination on heterogeneous catalysis.[69-70] Fluorination is known to create strong Lewis acid sites that are important in a variety of reactions.

3.3 Experimental Section

The ALD and ALE reactions were performed in a hot-walled, viscous and static flow reactor.[71] A proportional-integral-derivative (PID) temperature controller (2604, Eurotherm) maintained the reactor temperatures of 200, 250, and 300 °C. The temperature was controlled to within ±0.04°C of the set point. A bakeable capacitance manometer (Baratron 660A, MKS) monitored the reactor pressure.

ALD and ALE reactions were completed under static conditions in the reactor. Al_2O_3 ALD films were grown using sequential exposures of trimethylaluminium (TMA, 97% Sigma-Aldrich) and H_2O (Chromasolv for HPLC, Sigma-Aldrich) at 300°C. Al_2O_3 ALE was performed using sequential exposures of HF derived from HF-pyridine (70 wt% HF, Sigma-Aldrich) and TMA as the reactants. A gold-plated stainless-steel bubbler was used to contain the HF-pyridine and prevent corrosion. Ultra-high purity (UHP) N_2 gas was used to purge the reactor between reactant exposures during ALD and ALE. UHP N_2 was delivered to the reactor via a mass flow controller at a flow rate of 200 sccm that produced a N_2 pressure of 1.0 Torr. The TMA, H_2O and HF-pyridine precursors were all maintained at room temperature.

Static dosing was used for the ALD and ALE reactions. Before the precursors entered the reactor, the N_2 gas flow was stopped, and the reactor was pumped down to the base pressure of ~30 mTorr. The reactor was then isolated from the mechanical pump and the reactant valves opened to allow the pressure to reach a partial pressure between 0.07 and 9.0 Torr. The reactant valves were closed after reaching the desired pressure. The pressures were held statically for 20 seconds for the ALD or ALE reactions. Viscous N_2 gas flows then purged the reactor for 20 seconds. Subsequently, the chamber was filled with N_2 with the gate valve closed and then the chamber was pumped down to the base pressure. This purging and pumping sequence after the reactant exposures was employed for both ALD and ALE reactions.

Al_2O_3 ALD films were grown on Si coupons using 200 Al_2O_3 ALD cycles and used as the substrates. Si (100) wafers (University Wafers) were cut into 1 cm x 1 cm coupons using a diamond scribe prior to the Al_2O_3 ALD. The Al_2O_3 film thicknesses were characterized using spectroscopic ellipsometry (SE). The initial Al_2O_3 ALD film thicknesses were between 18 and 20 nm.

The thickness of the Al_2O_3 film after ALD and ALE was measured using a spectroscopic ellipsometer (M-2000, J. A. Woollam). The spectroscopic ellipsometer had a spectral range from 240 to 1700 nm and utilized an incidence angle of 70°. The Ψ and Δ parameters were analyzed using a Cauchy model with the CompleteEASE software package (J. A. Woollam).

X-ray photoelectron spectroscopy (XPS) (PHI 5600, RBD Instruments) measured the film composition. A monochromatic Al Kα x-ray source (1486.6 eV) was used to collect survey scans with a pass energy of 93.9 eV and step size of 0.400 eV. Auger Scan software package (Auger Scan, RBD Instruments) was employed to collect the data. Casa XPS software (Casa XPS, Casa Software) determined the surface concentrations using the peak areas for the C 1s, O 1s, Al 2p and F 1s XPS signals and the corresponding sensitivity factors. All peak energies were calibrated to the adventitious C 1s peak centered at 284.8 eV.

The fluorination of Al_2O_3 ALD films at 300 °C during sequential exposures of HF derived from HF-Pyridine was studied using *in situ* FTIR spectroscopy. The *in situ* FTIR studies were performed in a reactor equipped with an FTIR spectrometer that has been described previously.[72] The FTIR experiments employed high surface area Si nanoparticles (>98%, US Research Nanomaterials) with an average diameter of 20 – 30 nm.

The Si nanoparticles were mechanically pressed into a tungsten grid to facilitate the transmission FTIR measurements. The tungsten grid was 2 × 3 cm^2, 50 μm thick, with 100 grid lines per inch. The tungsten grid was resistively heated using a DC power supply (6268B, 20V/ 20A, Hewlett-Packard). The voltage output of the power supply was controlled by a PID temperature controller (Love Controls 16B, Dwyer Instruments). A type K thermocouple was attached at the bottom of the tungsten grid with epoxy (Ceramabond 571, Aremco). The epoxy also electrically isolated the thermocouple from the tungsten grid.

The Al_2O_3 film was grown using Al_2O_3 ALD using TMA and H_2O. Both the TMA and H_2O precursors were maintained at room temperature. Subsequently, the tungsten grid was resistively heated to 300°C and the Al_2O_3 ALD coating was exposed to HF at various pressures before recording the absorbance changes. The gold-coated bubbler for HF-pyridine was maintained at room temperature.

3.4 Results and Discussion

The Al_2O_3 ALD films were etched using HF and TMA at different reactant exposures and different temperatures. Both the HF and TMA reactants were at the same pressure. Figure 3-1 shows the Al_2O_3 thickness change after 20 ALE cycles using exposures of 20 seconds for HF and TMA followed by purging after each reactant exposure. The initial Al_2O_3 ALD film thickness was between 180 - 200 Å.

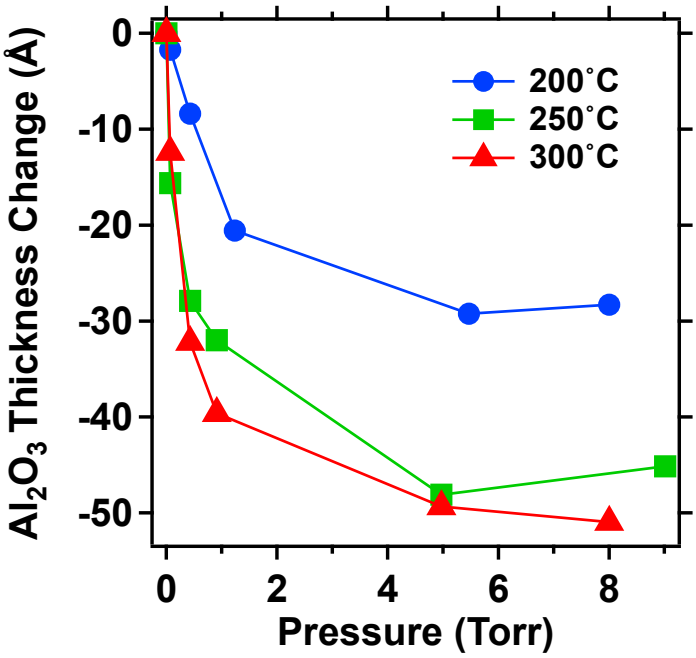

Figure 3-1: Al_2O_3 thickness change after 20 Al_2O_3 ALE cycles versus reactant pressure at 200°C, 250°C, and 300°C

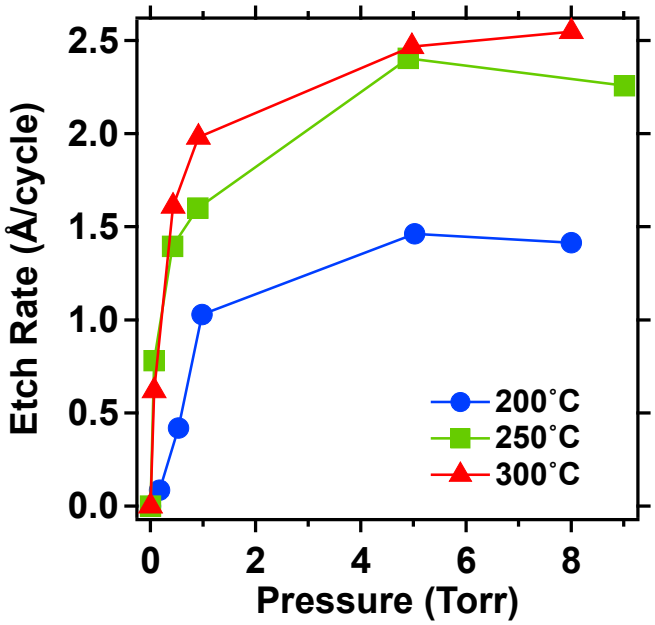

Figure 3-2: Al_2O_3 etch rate after 20 Al_2O_3 ALE cycles versus reactant pressure at 200°C, 250°C, and 300°C

Figure 3-1 reveals that the Al_2O_3 thickness change after 20 ALE cycles is larger at both higher temperatures and higher HF pressures. The Al_2O_3 thickness changes vary more rapidly at the lower HF pressures. The Al_2O_3 thickness change after 20 ALE cycles begins to reach saturation values at the higher HF pressures. The Al_2O_3 thickness changes after 20 ALE cycles are larger at the higher temperatures in this saturation regime.

Figure 3-2 displays the Al_2O_3 etch rates corresponding to the Al_2O_3 thickness changes after 20 ALE cycles in Figure 1. The etch rates were calculated from the difference in the Al_2O_3 film thickness before and after ALE divided by the 20 ALE cycles. The Al_2O_3 etch rates are higher at higher reactant pressures. The higher temperatures also display higher Al_2O_3 etch rates. Similar results have been obtained earlier for the Al_2O_3 etch rate versus HF exposure and substrate temperature.[21] Figure 3-2 shows that the etch rates reach nearly self-limiting values at

higher HF pressures. The Al_2O_3 etch rates are approximately 1.45, 2.30 and 2.50 Å/cycle at 200, 250 and 300 °C at higher HF pressures between 6-8 Torr.

The saturation behavior observed in Figure 3-1 and Figure 3-2 suggests that the HF fluorination of Al_2O_3 reaches self-limiting fluoride thicknesses at higher HF pressures. This behavior is like the oxidation of silicon surfaces. For the same oxidation time during silicon oxidation, higher silicon oxide thicknesses are observed at higher O_2 pressures.[73-74] In addition, the silicon oxidation rates are progressively reduced at longer oxidation times in accordance with parabolic rate law behavior.[74] This silicon oxidation behavior is described by Deal-Grove oxidation kinetics.[75] A model for Al_2O_3 fluorination will be described later.

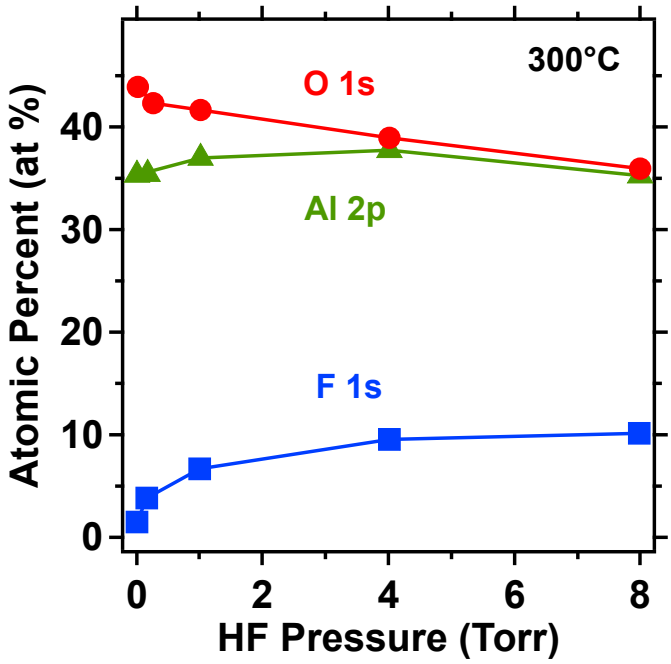

Figure 3-3: XPS measurements of atomic percent (atom %) of Al_2O_3 ALD film after HF exposures at various HF pressures for 30 s at 300°C

3.4.1 XPS Measurement of Al_2O_3 Fluorination

XPS analysis was used to characterize the fluorination of Al_2O_3. Al_2O_3 ALD films on Si wafers were exposed to HF exposures for 30 s at HF pressures of 0.15, 1.0, 4.0, and 8.0 Torr at 300 °C. After the HF exposures, the samples were immediately transferred to the XPS chamber to minimize atmospheric exposure. High resolution scans were recorded that included the Al 2p, O 1s, F 1s, and C 1s XPS peaks. The XPS spectra were then evaluated using analysis software (CasaXPS) to determine the surface composition.

Figure 3-3 shows the atomic percentages from the Al 2p, O 1s, and F 1s peaks after the HF exposures for 30 s at HF pressures of 0, 0.15, 1.0, 4.0 and 8.0 Torr at 300 °C. Figure 3 reveals that the oxygen percentage decreases and the fluorine percentage increases at the higher HF pressures. In contrast, the aluminum percentage remains nearly constant for the various HF pressures. The loss of oxygen and the gain of fluorine agrees with the fluorination reaction to produce AlF_3 or AlF_xO_y. The reaction for AlF_3 production is $Al_2O_3 + 6\ HF \rightarrow 2\ AlF_3 + 3H_2O$. The reaction for AlF_xO_y production is $Al_2O_3 + zHF \rightarrow 2AlO_{(6-z)/4}F_{z/2} + (z/2)H_2O$.

The Al 2p XPS core-level spectra of an initial Al_2O_3 ALD film is displayed in Figure 3-4a. The initial Al_2O_3 ALD film grown on a Si wafer is consistent with pristine Al_2O_3 with a peak at 74.3 eV and a full width at half maximum (FWHM) of 2.0 eV. This peak serves as a calibration reference for the fluorinated Al_2O_3 samples. An Al_2O_3 ALD film after exposure to HF pressure for 30 s at 4.0 Torr at 300°C is shown in Figure 3-4b.

The fluorination of Al_2O_3 leads to the growth of a higher energy shoulder in Figure 4b at a binding energy of 75.5 eV. This binding energy is lower than the reported binding energies of 77.3 eV and 77.5 eV for θ-AlF_3 and Δ-AlF_3.[33] A binding energy for Al 2p that is intermediate between 74.3 eV for Al_2O_3 and 77.3-77.5 eV for AlF_3 is consistent with an aluminum

oxyfluoride.[33, 41] This aluminum oxyfluoride layer is consistent with recent theoretical calculations of the aluminum fluoride layer on the surface of θ-Al_2O_3 after HF exposures.[68] HF exposure to λ-Al_2O_3 produced a dissociated F coverage of 7.1 ± 0.3 F/nm^2 after saturation HF exposures.[68] This F coverage is consistent with 1.5 F atoms bound to each surface Al atom.[68]

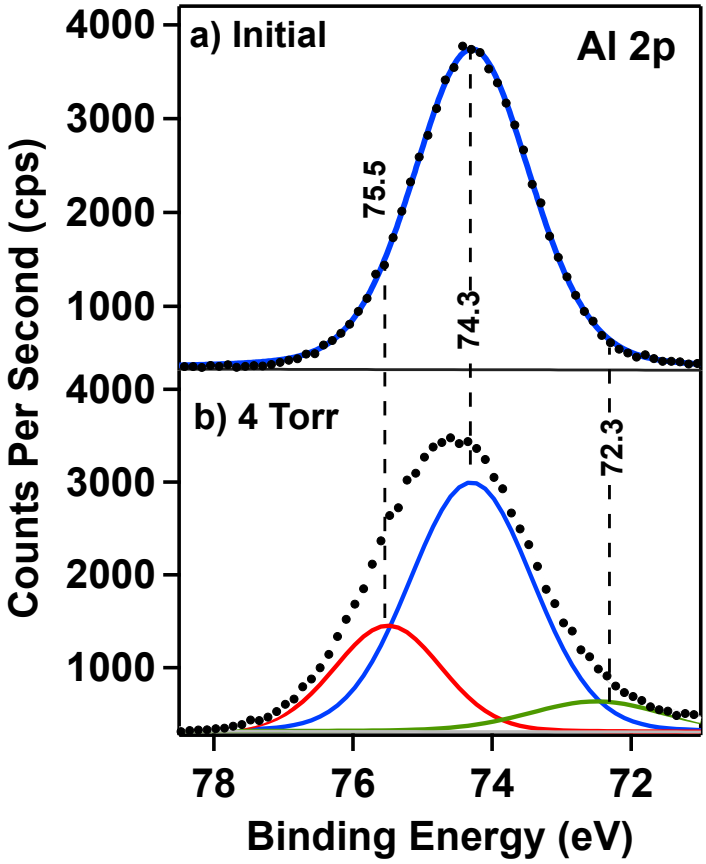

Figure 3-4: High resolution scan of the Al 2p XPS peak for (a) initial Al_2O_3 ALD film after HF exposure for 30 s at 3 Torr and 300°C

Some Al 2p XPS peak intensity also shifts to lower energies. Fitting of this shoulder at lower energy requires the addition of a small XPS peak at 72.3 eV. An Al 2p XPS peak at 72.3 eV is consistent with metallic aluminum.[41, 76] This apparent reduction may result from the

presence of H_2 in the HF. The H_2 is formed when HF is in contact with the stainless-steel walls of the gas lines for extended times. Mass spectrometer experiments confirmed that HF slowly reacts with the stainless-steel walls and produces H_2. This H_2 could then lead to the reduction of Al_2O_3, AlO_xF_y or AlOH species during the initial HF exposure at 300°C. However, this explanation is speculative because thermochemical calculations indicate that H_2 reduction of Al_2O_3, AlF_3 or $Al(OH)_3$ is not favorable.

3.4.2 Determination of Fluoride Layer Thickness

The thickness of the fluoride layer was also determined using XPS measurements. The sample was assumed to have a uniform layered structure composed of an Al_2O_3 substrate, an aluminum fluoride layer of varying thickness, and a 6 Å thick adventitious carbon layer at the sample-air interface.[77] The XPS results in Figure 4b indicate that the fluoride layer is an aluminum oxyfluoride. However, the exact composition of the aluminum oxyfluoride is not known. This XPS analysis considered fluoride layers with compositions of AlF_3, Al_2OF_4 and AlOF. The analysis assuming an aluminum oxyfluoride with a composition of Al_2OF_4 is given below.

The XPS electrons are derived from the C, Al, F and O in the three layers. XPS quantification requires analysis of the attenuation of photoelectron propagation in their source layers. In addition, the photoelectron propagation is also attenuated by each layer that covers the source layer.[78-79] For example, the C signal is derived from the top adventitious carbon layer.[77] The C photoelectrons will be attenuated by propagation in the carbon layer according to $\exp[-t/\lambda_C]$ where t is the thickness of the carbon layer at the source of the C photoelectron and λ_C = 30.2 Å is the inelastic mean free path (IMFP) of the C XPS photoelectron at 1202 eV in the carbon layer.[80]

The C XPS signal is proportional to λ_c, the carbon number density in the carbon layer times the integral of exp[-t/λ_C] from 0 to 6 Å.[77] This integral describes the effect of attenuation by the carbon layer on all the C XPS electrons from various thicknesses in the carbon layer. The C XPS signal can be determined by solving the integral of exp[-t/λ_C] from 0 to 6 Å and then multiplying by λ_c. The intensity of the C XPS signal is:

$$I_c = \rho_c \int_0^6 e^{-t/\lambda_c}\, dt$$

The fluorine signal is derived from F in the Al_2OF_4 layer under the carbon layer. The F signal is proportional to ρ_{F,Al_2OF_4} the fluorine number density in the Al_2OF_4 layer, times the integral of exp[-t/λ_F] from 0 to t_F, the thickness of the Al_2OF_4 layer. This integral describes the effect of attenuation by the Al_2OF_4 layer on the F XPS electrons. λ_F = 27.1 Å is the inelastic mean free path (IMFP) for the F XPS electrons at 801 eV.[80] The F XPS signal can be determined by solving the integral of exp[-t/λ_F] from 0 to t_F, the total thickness of the Al_2OF_4 layer, and then multiplying by λ_F. These F XPS electrons are then attenuated by the overlying carbon layer. The intensity of the F XPS signal is:

$$I_F = \rho_F e^{-6/\lambda_F} \int_0^{t_F} e^{-t/\lambda_F}\, \mathrm{dt}$$

The aluminum signal is derived from Al in the Al_2O_3 and Al in the Al_2OF_4 layer under the carbon layer. For the Al in the Al_2O_3 layer, the Al signal is proportional to ρ_{Al,Al_2O_3} the aluminum number density in the Al_2O_3 layer times the integral of exp[-t/$\lambda_{Al,Al2O3}$] from 0 to ∞. For the Al in the Al_2OF_4 layer, the Al signal is proportional to ρ_{Al,Al_2OF_4}, the aluminum number density in the Al_2OF_4 layer times the integral of exp[-t/$\lambda_{Al,Al2OF4}$] from 0 to t_F, the thickness of the

Al_2OF_4 layer. $\lambda_{Al,\ Al2O3} = \lambda_{Al,\ Al2OF4} = 27.7$ Å is the inelastic mean free path (IMFP) of the Al XPS electrons at 1412 eV.[81] The intensity of the Al XPS signal is::

$$I_{Al} = \rho_{Al,Al_2OF_4} e^{-6/\lambda_{Al}} \int_0^{t_f} e^{-t/\lambda_{Al}}\, dt + \rho_{Al,Al_2O_3} e^{-6/\lambda_{Al}} e^{-t_f/\lambda_{Al}} \int_0^{inf} e^{-t/\lambda_{Al}}\, dt$$

Lastly, the oxygen signal is derived from O in the Al_2O_3 layer under the carbon and Al_2OF_4 layers. $\lambda_O = 20.5$ Å is the inelastic mean free path (IMFP) in Angstroms for the O XPS electrons at 956 eV.[81] Following a similar treatment, the intensity of O XPS signal is::

$$` I_O = \rho_{O,C} \int_0^6 e^{-t/\lambda_O} dt + \rho_{O,Al_2OF_4} e^{-6/\lambda_O} \int_0^{t_F} e^{-t/\lambda_O} + \rho_{O,Al_2O_3} e^{-6/\lambda_O} e^{-t_F/\lambda_O} \int_0^{\infty} e^{-t/\lambda_O}$$

The total XPS signal is the sum of all the individual XPS electrons produced by the Al_2O_3, Al_2OF_4 and carbon layers and their attenuation during propagation. The thickness of the Al_2OF_4 layer was determined by varying t_F and determining the t_F value that was consistent with the observed C, Al, F, and O XPS signals. The number density for carbon in the adventitious carbon was 5 x 10^{22} cm^{-3}. The number densities for Al, F, and O in the Al_2OF_4 layer were 2.5 x 10^{22} cm^{-3}, 4.9 x 10^{22} x cm^{-3} and 1.2 x10^{22} cm^{-3}, respectively. The number densities for Al and O in the Al_2O_3 substrate were 3.66 x 10^{22} cm^{-3} and 5.5 x10^{22} cm^{-3}, respectively.

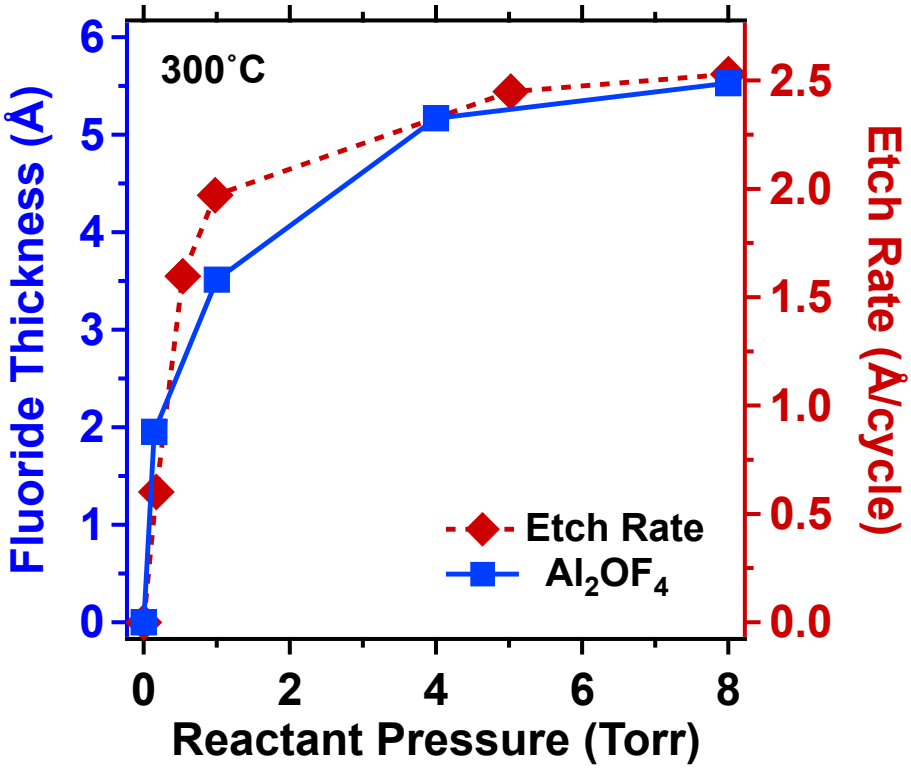

Figure 3-5: Comparison of fluoride thickness and etch rate during Al_2O_3 ALE versus reactant pressure. Fluoride thickness was measured by XPS analysis assuming a composition of Al_2OF_4 after HF exposure for 30 s at 300°C. Etch rate was measured for Al_2O_3 ALE at 300°C using reactant exposures of 30 s at various reactant pressures.

The thickness of the Al_2OF_4 layer as a function of HF pressure determined by the XPS measurements is displayed in Figure 3-5. The Al_2OF_4 fluoride layer thicknesses were 2.0, 3.5, 5.2 and 5.5 Å for HF pressures of 0.15, 1.0, 4.0 and 8.0 Torr, respectively. XPS analysis assuming fluoride layers with compositions of AlF_3 and AlOF yielded fluoride thicknesses with a similar functional form versus HF pressure to the results shown in Figure 3-5. However, the absolute fluoride thicknesses varied for the different aluminum fluorides. At an HF pressure of 8 Torr, the fluoride thicknesses were 4.5, 5.5 and 10.2 Å when the aluminum fluoride layer was assumed to be AlF_3, Al_2OF_4 and AlOF, respectively.

Figure 3-5 also compares the fluoride layer thicknesses with the Al_2O_3 etch rates obtained at the same HF pressures. The TMA pressure during the Al_2O_3 ALE was equivalent to the HF pressure. Figure 5 shows that there is excellent correspondence between the fluoride layer thicknesses and the Al_2O_3 etch rates. This correlation argues that the ligand-exchange reaction between TMA and the aluminum fluoride layer during Al_2O_3 ALE is removing Al_2O_3 at a rate that is proportional to the aluminum fluoride thickness.

Figure 3-6 shows the Al_2O_3 etch rate versus the fluoride layer thickness for reactant pressures between 0 - 8.0 Torr. The reactant pressures correspond to both the HF and TMA pressures during Al_2O_3 ALE. Higher reactant pressures increase both the fluoride layer thickness and the Al_2O_3 etch rate. The linear relationship between the etch rate and fluoride layer again indicates that the etch rate is proportional to the thickness of the fluoride layer.

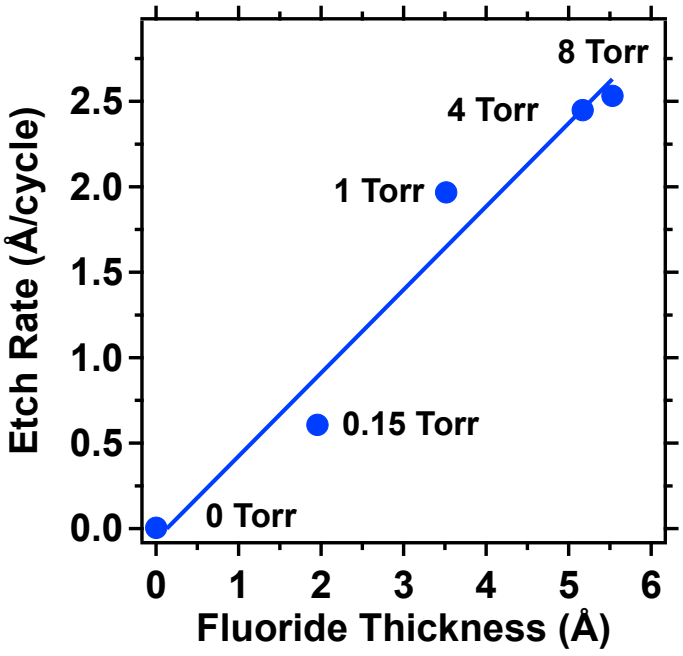

Figure 3-6: Correlation of etch rate for Al_2O_3 ALE and fluoride thickness assuming a composition of Al_2OF_4 for various reactant pressures.

3.4.3 FTIR Spectroscopy Measurements of Al_2O_3 Fluorination

FTIR spectroscopy was also used to monitor the fluorination of Al_2O_3. These fluorination experiments could be performed in situ without atmospheric exposures after the fluorination. Figure 3-7 shows the original Al_2O_3 ALD film and the same Al_2O_3 ALD film after subsequent consecutive HF exposures at 0.5 Torr under static conditions with the gate valve closed to the pump. The HF pressure was held for 15 seconds before purging the reactor. Results are displayed after 2, 4, 6, 8 and 10 HF exposures.

The absorbance peak at 850 cm^{-1} corresponds with the Al-O stretching vibration in Al_2O_3.[82] The absorbance peak at 700 cm^{-1} corresponds to the Al-F stretching vibration in AlF_3 or AlF_xO_y.[58] The absorbance progressively converts between Al-O stretching vibrations to Al-F stretching vibrations versus the consecutive HF exposures. The absorbance for the Al-O stretching vibration is reduced and the absorbance for the Al-F stretching vibrations is increased versus HF exposures. These results are consistent with the conversion of Al_2O_3 to AlF_3 or AlO_xF_y by the reactions $Al_2O_3 + 6HF \rightarrow 2AlF_3 + 3H_2O$ or $Al_2O_3 + zHF \rightarrow 2AlO_{(6-z)/4}F_{z/2} + (z/2)H_2O$.

An apparent isosbestic point exists in Figure 3-7 between the absorbance peaks for the Al-O and Al-F stretching vibrations. The isosbestic point occurs at 779 cm^{-1}. This isosbestic point argues for direct conversion of the aluminum oxide to aluminum fluoride. The Al-O and Al-F vibrations act nearly separately and independently of each other as the Al_2O_3 film is progressively fluorinated.

Figure 3-8 shows the difference spectra versus sequential HF exposures at 0.5 Torr and 300°C for 15 s. The results are shown after 1, 2, 4, 6, 8 and 10 HF exposures. These difference

spectra are all referenced to the initial Al_2O_3 ALD film on the silicon particles. The absorbance loss for the Al-O stretching vibration is centered at 850 cm^{-1} and the absorbance gain for the Al-F stretching vibration is centered at 700 cm^{-1}. The isosbestic point between the gain and loss of the absorbance peaks again occurs at 779 cm^{-1}.

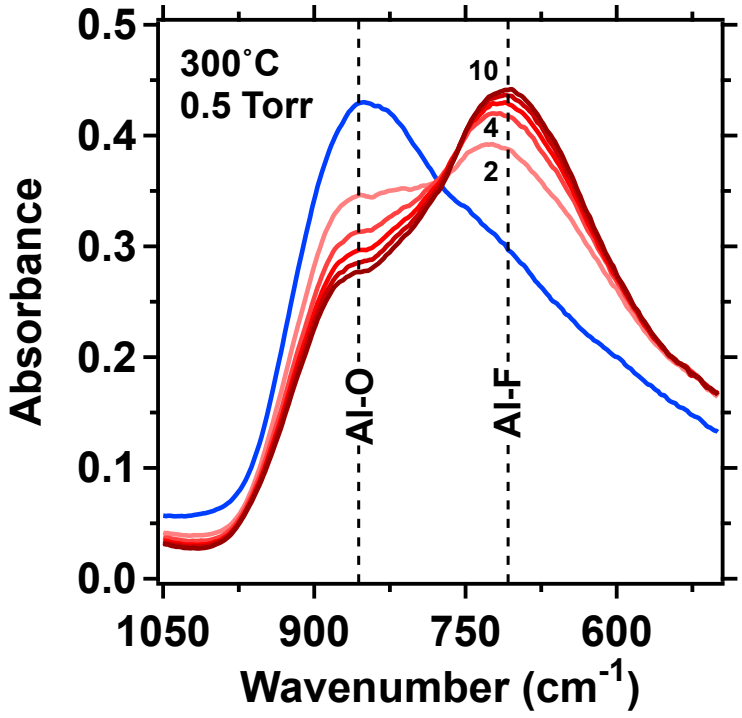

Figure 3-7: Integrated absorbance change for the Al-F stretching vibration versus HF exposure in units of Torr s during the fluorination of Al_2O_3 by HF at 300°C. The HF pressure was varied from 0.5 Torr to 8.0 Torr.

Difference spectra facilitate the determination of the integrated absorbance change of the Al-O and Al-F stretching vibrations versus HF exposure. Figure 3-9 shows the integrated absorbance change of the Al-O and Al-F stretching vibrations. The integrated absorbance changes were defined from the difference spectra displayed in Figure 8. Integration was

performed from the isosbestic point to 1100 cm^{-1} for the Al-O stretching vibration and from 500 to the isosbestic point for the Al-F stretching vibration. There is a correlation between the loss of absorbance for the Al-O stretching vibration and gain of absorbance for the Al-F stretching vibrations with HF exposure. Similar behavior was observed in Figure 3 when monitoring the XPS O 1s and F 1s peaks.

The conversion of aluminum oxide to aluminum fluoride is also dependent on the HF pressure. Figure 3-10 shows the initial spectrum for Al_2O_3 obtained after 15 cycles of Al_2O_3 ALD at 155°C referenced to the Si particles. The spectra are also shown for the Al_2O_3 ALD film after static HF exposures at 0.5 and 4.0 Torr, respectively. The spectra were recorded after 6 HF exposures for 15 s at both pressures at 300°C. After the 6 HF exposures, the spectra have nearly reached saturation levels where the absorbance changes become negligible with subsequent HF exposures. The results in Figure 3-10 indicate that the HF pressure increases the saturation level for the fluorination of Al_2O_3.

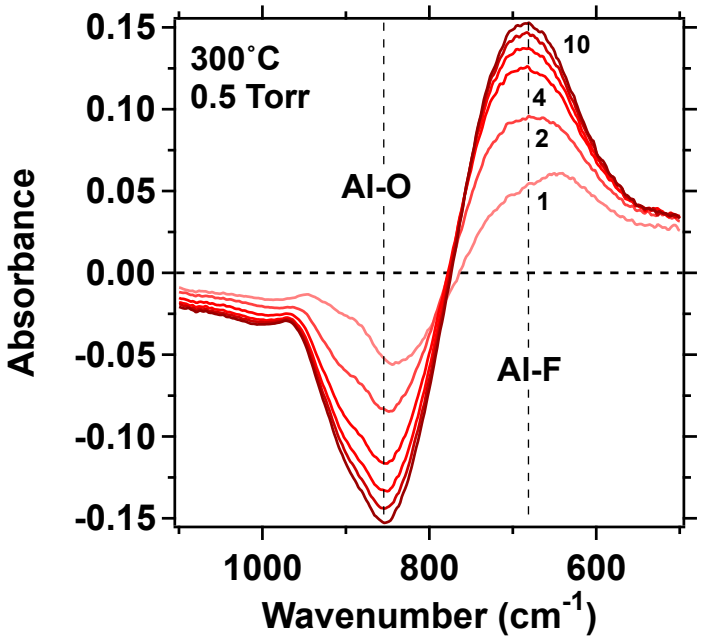

Figure 3-8: Difference spectra showing the absorbance of the Al-O and Al-F stretching vibrations during the fluorination of Al_2O_3 by HF at 300°C. The successive HF exposures from 1 to 20 HF exposures were defined by HF pressures of 4.0 Torr for 15 s.

Figure 3-11 shows the difference spectra versus sequential HF exposures for 15 s at 4 Torr and 300°C. The results are shown after 1, 2, 5, 10 and 20 HF exposures. The absorbance loss for the Al-O stretching vibration is centered at 940 cm^{-1} and the absorbance gain for the Al-F stretching vibration is peaked at 760 cm^{-1}. The absorbance changes at 4 Torr in Figure 3-11 are larger than the absorbance changes at 0.5 Torr in Figure 8. In addition, the frequency of the absorbance loss and gain are shifted to higher frequencies at HF pressures of 4 Torr.

The higher frequencies for the absorbance loss and gain at HF pressures of 4 Torr may be related to the vibrations lost and gained versus HF pressure. At low HF pressures of 0.5 Torr, the fluoride thickness is ~2.5 Å according to Figure 5 and fluorination is more confined to the Al_2O_3 surface region. At higher HF pressures of 4 Torr, the fluoride thickness is ~5.2 Å

according to Figure 5 and the fluorination occurs deeper into the Al_2O_3 bulk. Al-O bonds in the surface region that are lost during fluorination may have lower frequencies than the Al-O bonds located further into the Al_2O_3 bulk. Likewise, the Al-F bonds formed in the surface region may have lower frequencies than the Al-F bonds that are formed deeper into the Al_2O_3 bulk. As a result of these frequency shifts with HF pressure, the isosbestic points were also dependent on HF pressure. The isosbestic points were 779, 836, 840, and 842 cm^{-1} for HF pressures of 0.5, 1.0, 4.0 and 8.0 Torr respectively.

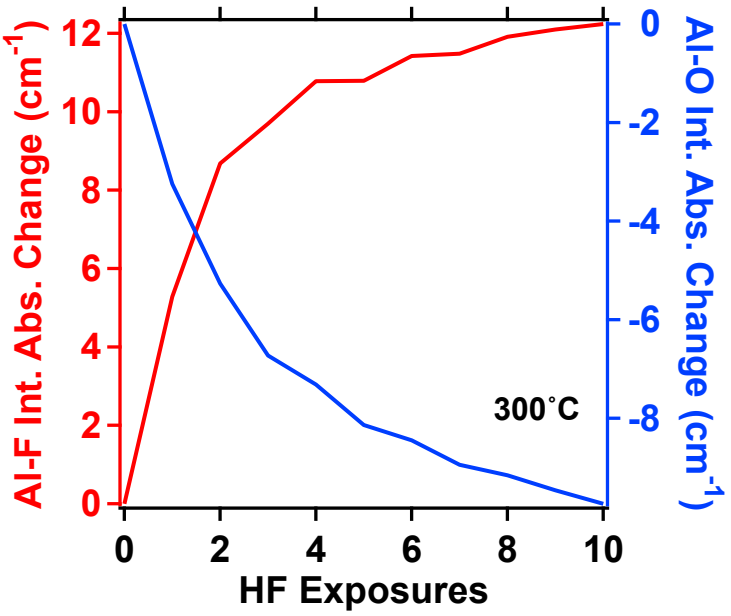

Figure 3-9: Integrated absorbance change for the Al-F stretching vibration during the fluorination of Al_2O_3 by HF at 300°C. The HF pressure was varied from 0.5 Torr to 8.0 Torr. Each HF exposure was performed for 15 s.

Figure 3-12 shows the integrated absorbance change of the Al-F stretching vibration as a function of HF exposures for HF pressures of 0.5, 1.0, 4.0 and 8.0 Torr. This integrated absorbance change was defined from 500 cm^{-1} to the isosbestic point for the difference spectra at

various HF pressures. The integrated absorbance change initially increases rapidly for the first several HF exposures. The integrated absorbance change then begins to level off after multiple HF exposures. The saturation levels are dependent on the HF pressure. Higher HF pressures produce larger integrated absorbance changes for the Al-F stretching vibrations.

Figure 3-13 shows the integrated absorbance change for the Al-F stretching vibration as a function of HF exposure in units of Torr s. These results illustrate that HF exposure defines the initial integrated absorbance change independent of the actual HF pressure. This regime is associated with the fluorination of the Al_2O_3 surface. At an integrated absorbance change >10 cm^{-1}, the integrated absorbance change is somewhat dependent on the HF pressure. HF exposures obtained using higher HF pressures have slightly higher integrated absorbance changes.

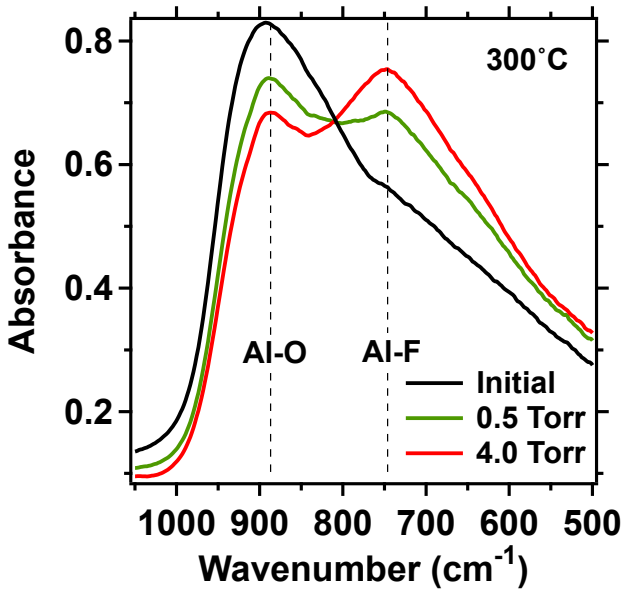

Figure 3-10: Absorbance for the Al-O and Al-F stretching vibrations during the fluorination of Al_2O_3 by HF at 300°C. The HF exposures were defined by HF pressures of 0.5 Torr and then 4.0 Torr for 15 s.

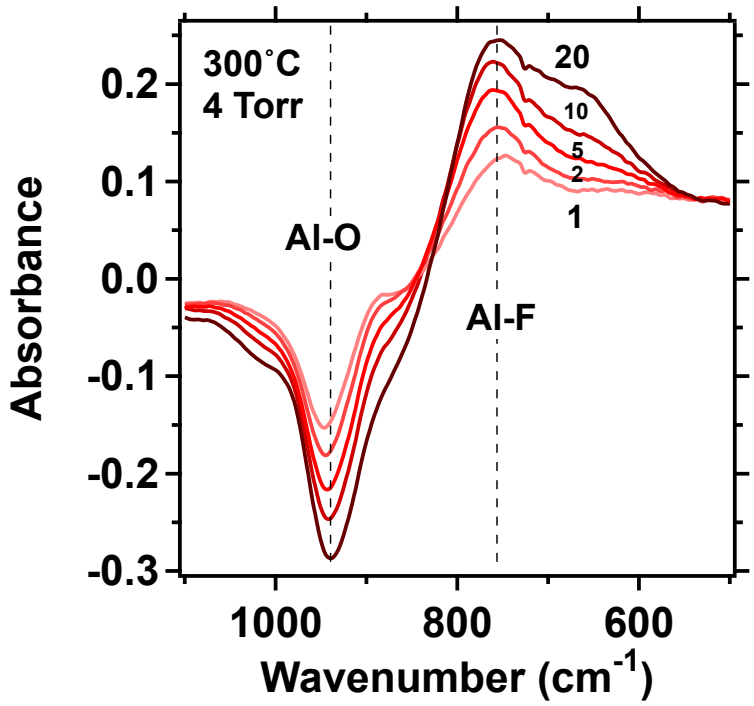

Figure 3-11: Difference spectra showing the absorbance of the Al-O and Al-F stretching vibrations during the fluorination of Al_2O_3 by HF at 300°C. The successive HF exposures from 1 to 20 HF exposures were defined by HF pressures of 4.0 Torr for 15 s.

3.4.4 Mechanism for Fluorination of Al_2O_3

The results in Figure 3-12 and Figure 3-13 suggest a mechanism for Al_2O_3 fluorination based on rapid fluorination of the Al_2O_3 surface and then slower fluorination of the near surface region. The Al_2O_3 surface is fluorinated based on site availability consistent with Langmuir adsorption. The rate of surface fluorination is expected to follow Langmuir adsorption kinetics given by $d\theta/dt = b(1-\theta_s)$ where b is a rate constant that is proportional to HF pressure and θ_s is the saturated fluorine coverage. Integration of this rate equation predicts that $\theta(t) = \theta_s [1- \exp(-bt)]$.

In comparison, fluorination of the near surface region is expected to produce a fluoride thickness, x, that grows according to dx/dt = k/x. k is a constant that is dependent on the HF pressure, $k = k_0P$. The inverse dependence of dx/dt on x is consistent with a fluoride thickness that acts as a diffusion barrier for subsequent fluorination. Integration of this rate equation yields $x(t)^2 = 2kt$. This equation is known as the parabolic law.[83]

Mathematically combining the surface and near surface fluorination rates into one composite expression is difficult. An approximation that allows for derivation of a composite solution assumes that the surface fluorination rate can be treated as $dx/dt = ck/x\ (\exp(-t/\lambda))$ where c is a constant and λ is inversely proportional to the HF pressure, $\tau = \tau_0/P$. Integration of this rate equation yields $x(t)^2 = ck\tau[1-\exp(-t/\lambda)]$. This integrated rate equation is similar in form to the integration of the Langmuir adsorption rate expression. However, the square of the fluoride thickness is present instead of the linear fluorine coverage.

Treating the surface fluorination as $dx/dt = ck/x\ (\exp(-t/\lambda))$ leads to a composite expression for the surface and near surface fluorination rates:

$$\frac{dx}{dt} = \frac{k}{x}[1 + ce^{-t/\tau}]$$

After rearrangement, the integrals can be written as:

$$\int_0^x x'dx' = k\int_0^t (1 - ce^{-\frac{t'}{\tau}})dt'$$

Solving these integrals then leads to the expression for the fluoride thickness, x:

$$x(t)^2 = 2kt + M(1 - e^{-t/\tau_0})$$

where $M=2kc\tau$. The pressure dependence for $x(t)^2$ given by Equation 7 can then be highlighted by substituting for $k = k_0P$ and $\tau = \tau_0/P$. These substitutions yield:

$$x(t)^2 = (Pk_0)t + M\left(1 - e^{-Pt/\tau_0}\right)$$

Assuming that the Al-F integrated absorbance change measures the Al_2O_3 fluorination, Equation 8 can be used to fit the experimental results. Figure 3-14 shows the fits for $x(t)^2$ in Equation 8 to the square of the Al-F integrated absorbance change for HF pressures of 0.5, 1.0, 4.0 and 8.0 Torr. These fits used constant values of k_0= 0.2 $(cm^{-1})^2$/(Torr s), M=340 $(cm^{-1})^2$ and τ_0=144(Torr s) for all the HF pressures. k_0 and M have units of $(cm^{-1})^2$ because $x(t)^2$ in Equation 8 was fit to the Al-F integrated absorbance change in units of $(cm^{-1})^2$.

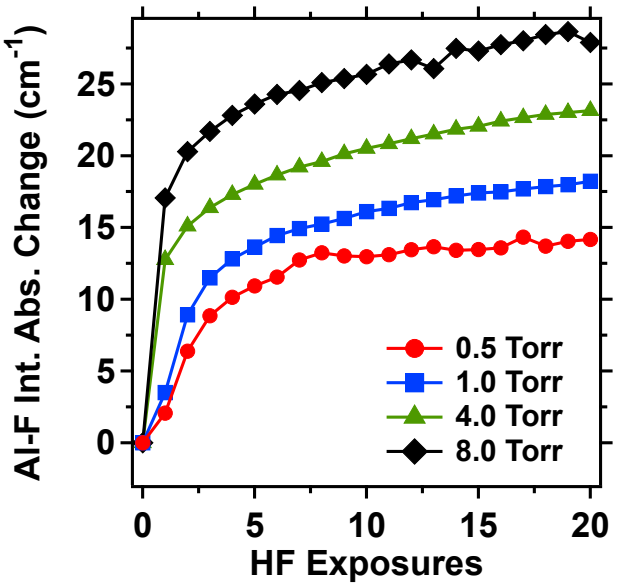

Figure 3-12: Integrated absorbance change for the Al-F stretching vibration during the fluorination of Al_2O_3 by HF at 300°C. The HF pressure was varied from 0.5 Torr to 8.0 Torr. Each HF exposure was performed for 15 s.

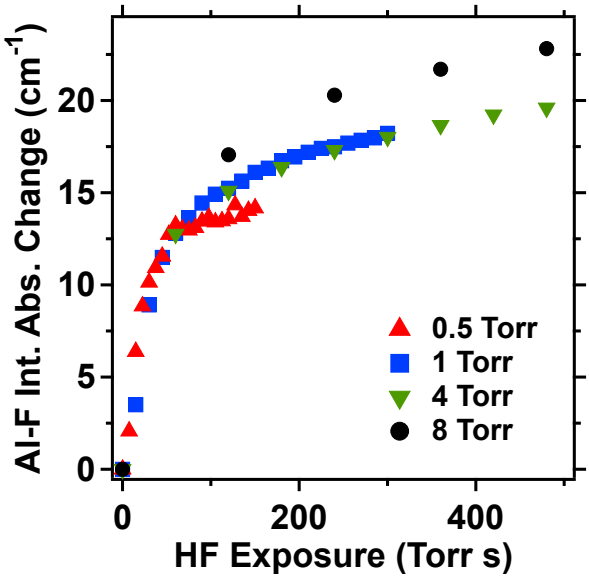

Figure 3-13: Integrated absorbance change for the Al-F stretching vibration versus HF exposure in units of Torr s during the fluorination of Al_2O_3 by HF at 300°C. The HF pressure was varied from 0.5 Torr to 8.0 Torr.

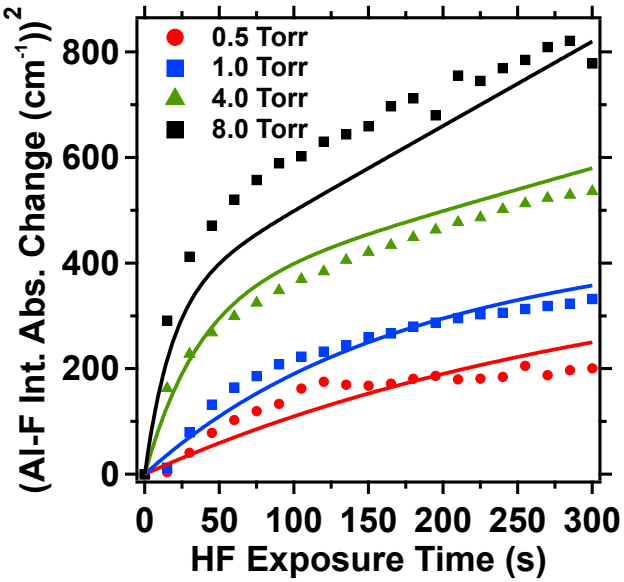

Figure 3-14: Comparison of $x(t)^2$ given by Equation 8 for the square of the fluoride thickness versus time for different HF pressures to the square of the Al-F integrated absorbance change versus HF exposure time at different HF pressures.

The $x(t)^2$ fits are in approximate agreement with the experimental data for the square of the Al-F integrated absorbance change for the various HF pressures. Equation 8 is close to capturing the pressure dependence in the surface and near surface fluorination rates of Al_2O_3. The initial fluorination of the Al_2O_3 surface is faster at the higher HF pressures. In addition, the magnitude of fluorination of the Al_2O_3 near surface region is also dependent on the HF pressure and displays the linear increase expected from the parabolic law.

This mechanism for the fluorination of Al_2O_3 is like the mechanism for silicon oxidation.[75, 84] For both systems, there are rapid surface kinetics followed by slower parabolic law kinetics for the near surface region. The surface kinetics can be understood in terms of surface site availability. The kinetics for the near surface region can be described according to transport through a growing diffusion barrier on the surface. Higher pressures provide a larger coverage gradient for transport through the surface diffusion barrier.

3.5 Conclusions

Thermal Al_2O_3 ALE can be achieved using a fluorination and ligand-exchange mechanism with HF and TMA as the reactants. This study explored the effect of HF pressure on the Al_2O_3 etching rate and Al_2O_3 fluorination. Using ex situ SE measurements, the Al_2O_3 etch rates at different temperatures were observed to increase with HF pressures and then level out at higher HF pressures. At 300 °C, Al_2O_3 etch rates of 0.6, 1.6, 2.0, 2.4 and 2.5 Å/cycle were measured for HF pressures of 0.17, 0.5, 1.0, 5.0 and 8.0 Torr, respectively. Assuming an Al_2OF_4 layer on the Al_2O_3 surface, the estimated fluoride thicknesses on Al_2O_3 also increased with HF pressures and reached saturation values at higher HF pressures. Fluoride thicknesses on Al_2O_3 of

2.0, 3.5, 5.2 and 5.5 Å were obtained for HF pressures of 0.15, 1.0, 4.0 and 8.0 Torr, respectively, at 300°C. There was a very good correlation between the Al_2O_3 etch rates and the fluoride layer thicknesses versus HF pressure.

The time dependence and magnitude of the Al_2O_3 fluorination was also analyzed using in situ FTIR vibrational studies by monitoring the infrared absorbance from the Al-O and Al-F stretching vibrations. The time dependence of the Al_2O_3 fluorination was understood by a mechanism involving the rapid fluorination of the Al_2O_3 surface at initial HF exposures and slower fluorination into the Al_2O_3 near surface region that begins to level off at longer HF exposures times. The pressure dependence of the Al_2O_3 fluorination was explained by facile adsorption on the initial available sites on the Al_2O_3 surface. This rapid fluorination is followed by slower diffusion into the near surface region of Al_2O_3 where the fluoride layer serves as a diffusion barrier to subsequent fluorination.

The fluoride layer acts as a diffusion barrier and yields parabolic law behavior. The higher HF pressures provide a higher coverage gradient for transport through the diffusion barrier and yield larger fluoride thicknesses for equal fluorination times. A kinetic model was developed that combined the rates of surface and near surface fluorination. The integration of the combined kinetic rate law yielded a solution for the fluoride thickness versus time as a function of HF pressure. This solution for the square of the fluoride thickness was in good agreement with the experimental results for the square of the Al-F integrated absorbance change for the various HF pressures.

Atomic Layer Etching of Aluminum Nitride with HF or XeF_2 and BCl_3

Austin Cano, Ann-Lii-Rosales, Steven M. George

Department of Chemistry, University of Colorado at Boulder, Colorado 80309, USA

4.1 Abstract

Thermal atomic layer etching (ALE) of amorphous and crystalline aluminum nitride is reported using hydrogen fluoride (HF) or xenon difluoride (XeF_2) as a fluorination source and boron trichloride (BCl_3) as a ligand exchange reagent. HF was used when etching atomic layer deposited (ALD) grown aluminum nitride and XeF_2 was needed when etching crystalline aluminum nitride. Infrared spectroscopy was utilized to study the growth of aluminum nitride with tris(dimethylamido)aluminum and ammonia. FTIR was then used to understand the etching system with HF and BCl_3. FTIR showed linear etching at temperatures at or greater than 250ºC with a mechanism which closely resembled ligand-exchange reactions. In-situ spectroscopic ellipsometry (SE) was used to investigate the etching of crystalline aluminum nitride. HF and BCl_3 was not able to etch aluminum nitride at available temperatures, therefore a stronger fluorination source of XeF_2 was used. Crystalline aluminum nitride was etched with XeF_2 and static exposures of BCl_3 with an etching rate varying from growth at 212ºC and 0.62 Å/cycle at 298ºC. X-ray photoelectron spectroscopy (XPS) showed aluminum fluoride being created during the XeF_2 exposure and removed after the BCl_3 exposure. A water exposure was utilized to remove surface contaminants after etching. Atomic force microscopy (AFM) showed the

aluminum nitride surface slightly smoothened after etching with XeF_2 and BCl_3 and slightly roughened after ending the etching experiments after a water exposure.

4.2 Introduction

Atomic layer etching (ALE) is a technique used to remove sub-nanometer amounts of material. This is done by using sequential exposures of reactants which produce a self-limiting etching cycle.[10, 85] ALE has been done by utilizing plasma technology as well as heat. Plasma etching uses energetic ions, radicals, and electrons to drive chemical reactions towards volatile etch species, is typically anisotropic and can be done at low temperatures. Thermal ALE uses heat and to drive chemical reactions, is isotropic and typically needs temperatures above 200ºC although etching systems exist at lower temperatures as well.[22, 28, 57, 59, 86]

There have been a variety of materials where thermal ALE has been studied. First reports of ligand-exchange reactions had taken place on Al_2O_3 etching systems.[22, 87-88] Ligand exchange was also reported as the mechanism for HfO_2, ZrO_2 and aluminum nitride etching.[28, 63, 89]. Although the dominant reaction mechanism in thermal ALE has been an initial modification of the surface by fluorination followed by ligand-exchange reactions, there have been other mechanisms that play a role in thermal ALE. One such mechanism involved a conversion of the surface oxide into another oxide which was able to be etched. This was the case with ZnO and SiO_2 systems.[16-17] There were also systems where the etching only took place when the surface was first oxidized and then was etched by an oxide etching system that had been studied previously such was the case with W, Si and SiN systems.[18-19, 61]

The first step in thermal ALE involves a surface modification of the substrate. In thermal ALE this is often a fluorination of the substrate.[85] This reaction also releases some volatile product as well such as H_2O or possibly NH_3 for oxides and nitrides respectively. The

modification step is followed by a removal of the modified surface to form volatile etch products. The modified layer is then removed by undergoing some chemical reaction to form volatile etch products. This is often done by ligand exchange reactions. The ligand-exchange reaction in thermal ALE is the process of donation of a ligand with the acceptance of a new ligand from the surface. Due to each reaction being self-limiting it is possible to control the thickness of etched material precisely.

Aluminum nitride is a dielectric material with great thermal properties. The thermal conductivity of aluminum nitride is high, and the thermal expansion is close to that of silicon which makes aluminum nitride a great choice for high power applications in integrated circuits. One of which is high electron mobility transistors (HEMT) where aluminum nitride is used as a good seed layer for growth of other III-V materials (mainly GaN) as well as a good diffusion barrier which is important during high temperature processes.[90] Aluminum nitrides fantastic thermal properties can enhance thermal management in next generation gallium nitride HEMT's. Etching of aluminum nitride has been studied before with applications in micro electromechanical resonators where thickness of aluminum nitride can be tuned for different applications in micro or nano devices.[91]

The etching of aluminum nitride is reported here. Atomic layer deposition of aluminum nitride is first done by alternating exposures of tris(dimethylamido)aluminum and ammonia. This film is then etched successfully with HF and BCl_3. The reaction pathway shows signs of fluorination and ligand exchange. The etching of single crystal aluminum nitride is then studied. There is no observable etching with HF and BCl_3. This led to explore stronger fluorination sources with XeF_2. When XeF_2 is flown in viscous flow and BCl_3 in static flow there was etching seen at temperatures as low as 212ºC. X-ray photoelectron spectroscopy showed evidence of

fluorination during the XeF_2 exposure and removal of the fluoride on the BCl_3 exposure. The volatile products were determined to be $AlCl_3$ and BF_xCl_y via mass spectrometry when flowing BCl_3 over AlF_3 powder.

4.3 Experimental Methods

FTIR experiments were carried out in a hot-walled, viscous flow reactor. A full explanation of this reactor can be found in previous work.[92] The reactor tube is heated by a custom Watlow heater. The heater was controlled by a custom PID controller. Silicon powder (US-Nano Research Materials) was pressed into a 3cm by 1.5cm tungsten grid with grid spacings of 50 μm with 100 gridlines per inch. The grid spacing was chosen to allow particles to fit into the grid without falling out. The silicon particles have an average diameter of 30-50nm. A small diameter nano-powder is needed to achieve the maximum signal to noise of thin films deposited on them. The grid was resistively heated by a Hewlett-Packard 626B power supply. with a supplied current of ~20 amps for s substrate temperature of 400°C. The substrate temperature was monitored by a type-k thermocouple which adheres to the grid with a nonconductive epoxy (Cermabond, Aremco 571).

Aluminum nitride deposition in the in-situ FTIR reactor was done with tris(dimethylamido)aluminum (TDMAA) obtained from Strem Chemicals. TDMAA was needed to be heated to get any appreciable amount of vapor. TDMAA was heated to 85°C-100°C and had a headspace flow of ~20-50 sccm to entrain as much TDMAA precursor as possible. Ammonia was used as the co-reagent in the aluminum nitride deposition and was purchased from Airgas (99%). To obtain the highest purity of ammonia, a purifying unit from Matheson was used to remove as much water from the line as possible. BCl_3 and HF-pyridine and XeF_2 were all used in the etching of aluminum nitride. Boron trichloride cylinder was purchased from Synquest

Chemicals (BCl_3, 99%). HF derived from HF-pyridine (70% HF, 30% pyridine) was purchased from Millipore-Sigma and was loaded into a bored out gold-plated bubbler to minimize corrosion on the stainless-steel container. Xenon difluoride was obtained from Strem Chemicals with a purity of 99.5% XeF_2. A carrier gas of UHP N_2 was used and FTIR experiments which had a flow of 50 sccm for a transient N_2 pressure of 1.0 Torr.

FTIR spectrum was obtained with a Nicolet 6700 or an iS50R Thermofisher spectrometer. The light was generated and split using a KBr beam splitter and then was redirected into a viscous flow tube where the light passed through the silicon powder sample. The light then was directed to outside the reactor to an MCT-B detector. Vacuum was maintained by two KBr windows which are separated from the etching and deposition chemistry by gate valves and only opened while obtaining a spectrum. Final spectra were averaged for 100 scans with a resolution of 4 cm^{-1} and data spacing of 0.482 cm^{-1}. Backgrounds were collected before each experiment was conducted.

In-situ ellipsometry experiments were done in a home built in-situ chemical reactor reported on previously.[61] The reactor is a warm walled with a resistive heater which elevates the sample temperature above that of its surroundings with a sample temperature limit of ~370ºC. The polarized light hits the sample at a 70° angle from normal and is fixed at this angle. A spectroscopic ellipsometer (M-2000, J. A. Woollam) was used for all ellipsometry experiments. Wavelengths from 240nm to 1700nm were used in the fitting of the film optical properties. The Ψ and Δ parameters were analyzed with the CompleteEASE software package (J. A. Woollam). Single crystal aluminum nitride wafers were purchased from Kyma Technologies. The thickness of the aluminum nitride ranged from 300nm to 400nm. To fit the wafer with ellipsometry models, an ordinary sapphire model was used to model the sapphire substrate. The aluminum

nitride layer was fit using an extended Cauchy model with an Urbach coefficients. This gave index of refraction which was close to 2.5. This is higher than previously reported for aluminum nitride index of refraction regardless of chosen model.[63, 93-94] A surface roughness model was also applied. The surface roughness has some correlation to top layer formation (such as a native oxide). Mean square errors (MSE) were consistently below 10.

Static exposures in the in-situ ellipsometry reactor were done by the following procedure. First the valve connecting the nitrogen carrier gas to the reactor body was closed and the gas of the chamber was allowed to be pumped out fully. Then the valve to the vacuum pump was closed after which the BCl_3 was flowed into the reactor body. Once a pressure setpoint was hit the valve to the precursor was closed and the BCl_3 was allowed to react within the reactor body for a period (the exposure time). Once the dosing time was reached the valve to the pump was opened and finally the valve to the nitrogen carrier gas was opened. A carrier gas of UHP N_2 was used and SE experiments which had a flow of 200 sccm for a transient N_2 pressure of 2.0 Torr.

Quadrupole mass spectrometry was done in a new reactor described previously. The volatile etch products were observed using quadrupole mass spectrometer (Extrel, MAX-QMS Flanged Mounted System. An electron ionization energy of 70 eV was used for these experiments. To minimize exposures to corrosive gaseous species the ionizer and analyzer were positioned perpendicular to the incoming molecular beam. AlF_3 powder was purchased from US-Nano Research Materials (99.5%).

X-ray photoelectron spectroscopy (XPS) (PHI 5600, RBD Instruments) measured the film composition. A monochromatic Al Kα x-ray source (1486.6 eV) was used to collect survey scans with a pass energy of 93.9 eV and step size of 0.400 eV. Casa XPS software (Casa XPS, Casa Software) determined the surface concentrations using the peak areas for the C 1s, O 1s, Al

2p N 1s F 1s and B 2p XPS signals and the corresponding sensitivity factors. All peaks were calibrated to the adventitious carbon C 1s peak centered at 284.8 eV.

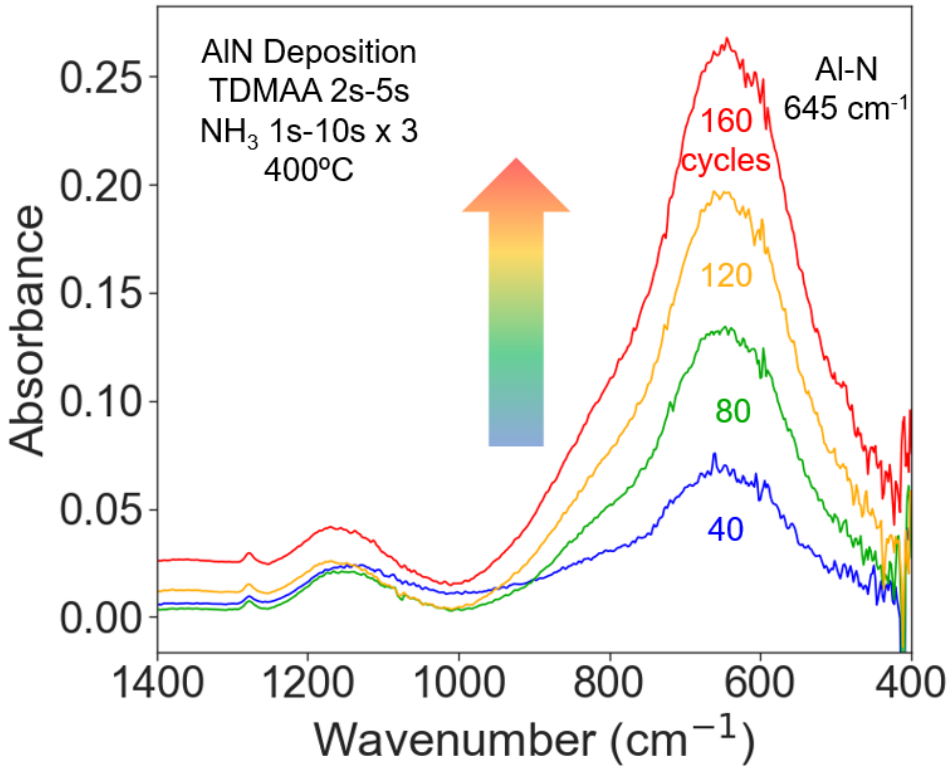

Figure 4-1: FTIR spectra after 40, 80, 120, and 160 ALD cycles of TDMAA and NH_3 shown from 400 to 1400 cm^{-1}

4.4 Discussion and Results

Aluminum nitride ALD was monitored in-situ with the FTIR apparatus. Figure 4-1 shows the growth of aluminum nitride after every 40 cycles for 120 TDMAA and NH_3 cycles at 400ºC. After 40 cycles of TDMAA and NH_3 there is a clear increase of absorbance at 645 cm^{-1}. This peak is consistent with the Al-N stretching vibrational band.[36-37, 95] After 40 ALD cycles there are other peaks which arise as well. The Al-N vibrational band has a shoulder at 850 cm^{-1} which is consistent with the LO Al-O stretching vibration.[96-97] This is due to the interface with

the native oxide of silicon. During initial cycles of aluminum nitride, the Al-O peak grows but later cycles show no continued increase of the Al-O band. There is a peak at 1150 cm^{-1} which is assigned to Si-O vibrational mode likely from small H_2O contamination in the initial cycles of NH_3. No shown are small peaks at 3200 cm^{-1}, and 2110 cm^{-1}. The peak at 3200 cm^{-1} is due to small amounts of N-H during deposition. There is another small peak centered at 2110 cm^{-1} is representative of the AlN-N vibrational mode.[36] During the last 40 cycles of aluminum nitride deposition there was no detectable increases in Al-O vibrational band. The FWHM of the Al-N peak was 315 cm^{-1}. This broadness could be due to an amorphous aluminum nitride film or polycrystalline film.

To monitor the etching behavior of this aluminum nitride film infrared spectra were taken after each half-cycle during sequential exposures of HF and BCl_3. Figure 4-2 shows the etching of aluminum nitride after various cycles of HF and BCl_3 at 350°C. The peak of the absorbance loss was centered at 655 cm^{-1}, very close to the absorbance gain during Al-N growth at 645 cm^{-1}. This small change is most likely due to a small amount of aluminum fluoride increase at a frequency lower than that of Al-N. This would slightly shift the loss of Al-N to a higher-than-expected frequency. This Al-F peak at 500-700 cm^{-1} is not distinguishable due to the Al-N adsorption centered at 645 cm^{-1}. There was a linear decrease in the absorption of aluminum nitride vibrational mode as a function of HF and BCl_3 cycles. There is a slight decrease in the etch rate towards the end of the 27 cycles due to decreased amounts of aluminum nitride on the silicon powder. There is also a small increase in absorbance around 1240 cm^{-1} which could be some B-N formation during initial BCl_3 exposures.

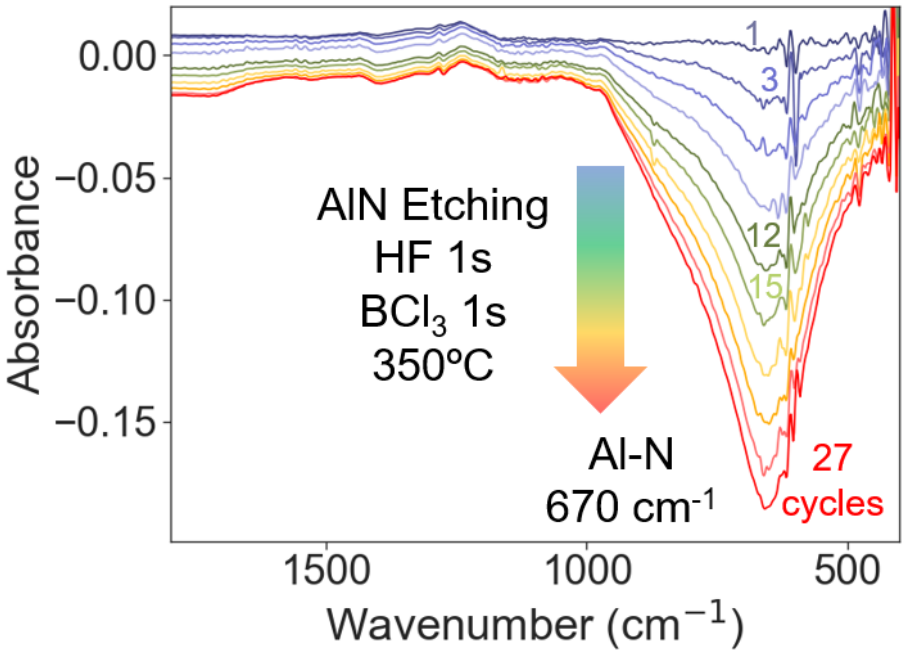

Figure 4-2: FTIR spectra every third cycle to 27 cycles of ALE with HF and BCl_3 at 350ºC between 400-1800 cm^{-1}

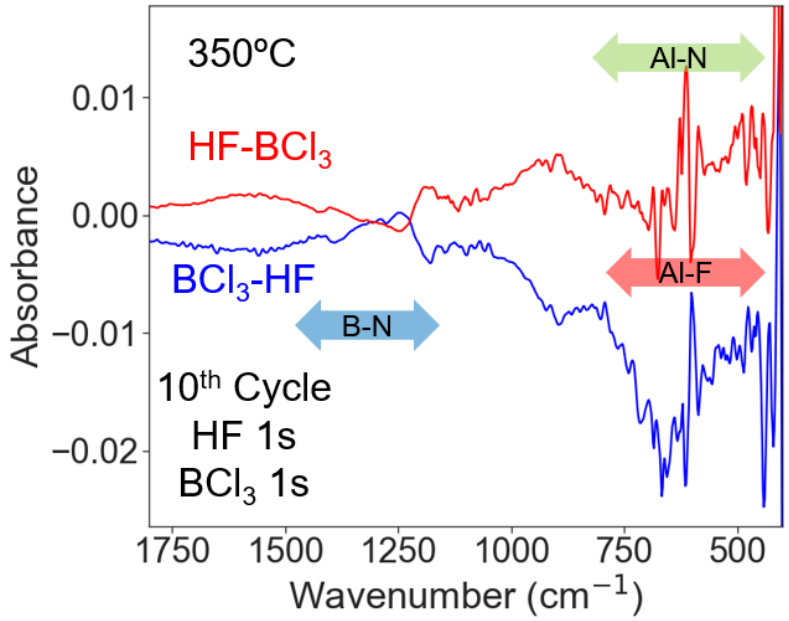

Figure 4-3: FTIR difference spectra after the HF exposure (red) and the BCl_3 exposure (blue) at 350ºC

FTIR is a useful tool for understanding surface changes between half-cycles. Difference spectra are created by referencing a previous spectrum to isolate the change in between spectra. Figure 4-3 displays the FTIR difference spectra during the 10th cycle of aluminum nitride etching at 350°C referencing the previous BCl_3 or previous HF exposures for the HF (red) and BCl_3(blue) exposures respectively. The HF exposure is complicated by the overlap of the Al-N and Al-F vibrational features.[36, 41, 87] During the HF exposure, there is a small decrease in B-N vibrational band. The Al-F and Al-N features are difficult to make conclusions about due to large peak overlap. One feature of note is the B-N vibrational band from 1200 cm^{-1} to 1450 cm^{-1}. This increases during the BCl_3 exposure but is removed ruing the HF exposure. BCl_3 can undergo different mechanisms in thermal ALE. BCl_3 can undergo conversion reactions where one metal oxide or nitride is converted to another metal oxide or nitride.[15, 61, 98] Here it seems that there may be small amounts of conversion happening on the BCl_3 exposure creating BN which is removed by the subsequent HF exposure. Figure 4-3 also shows the large decrease in absorbance at 650 cm^{-1}. This is likely the removal of aluminum fluoride created in the HF exposure. This fluoride is difficult to interpret due to the overlap in Al-N and Al-F vibrational modes.

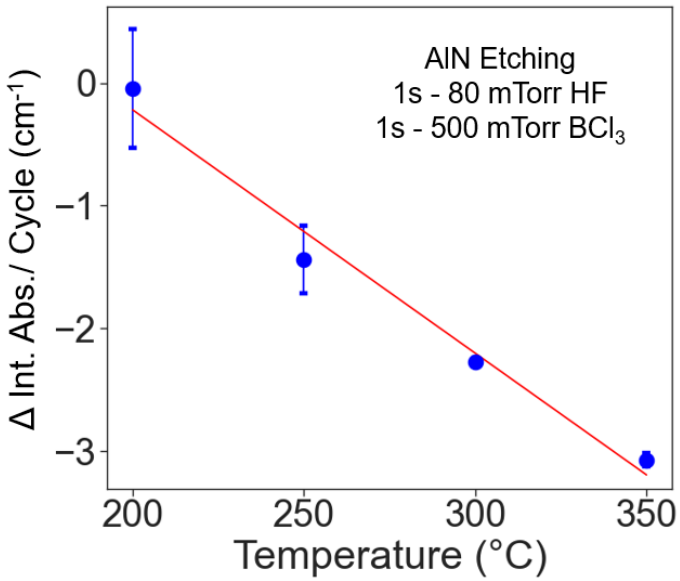

Figure 4-4: Temperature dependence of HF and BCl_3 etching of ALD grown aluminum nitride showing the change in the integrated absorbance at 200ºC, 250ºC, 300ºC, and 350ºC from 400-1000 cm^{-1}.

To try to further understand the etching characteristics of the ALD grown aluminum nitride the temperature dependence was investigated. Figure 4-4 shows the change in the integrated absorbance per cycle from 400-1000 cm^{-1}. This etching was done at 200ºC, 250ºC, 300ºC and 350ºC. The etching rate increased as a function of increasing temperature. At 200ºC there was no clear etching seen but by 250ºC there was clear losses in the Al-N vibrational band. The Al-N vibrational loss rate increased at 300ºC and 350ºC. This increase in the etching rate is most likely due to increased fluorination and thus there is more AlF_3 to volatilize in the BCl_3 exposure. The initial onset of etching at temperatures above 200ºC is likely due to the temperature dependence of the ligand-exchange reaction. This idea is explored more in Figure 4-13.

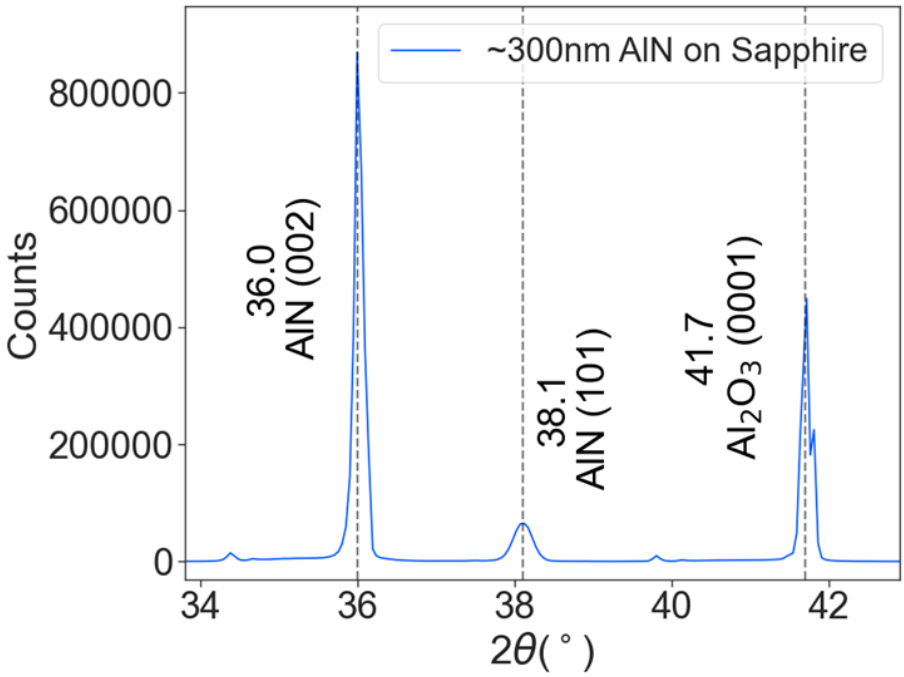

Figure 4-5: XRD pattern of the single crystal AlN on sapphire substrate

When ALE is employed commercially, it is usually done on high quality substrates. To fully understand the ALE of aluminum nitride, the etching of crystalline aluminum nitride was also looked at. Figure 4-5 shows the XRD pattern of the single crystal aluminum nitride used in these experiments. Aluminum nitride was mostly in the (002) phase with small amounts of (101). The crystalline sapphire substrate was also seen in the XRD pattern due to the aluminum nitride thickness being 300 nm although this changed from sample to sample. Crystalline materials are likely to be harder to fluorinate than their amorphous or polycrystalline counterparts.[99-100]

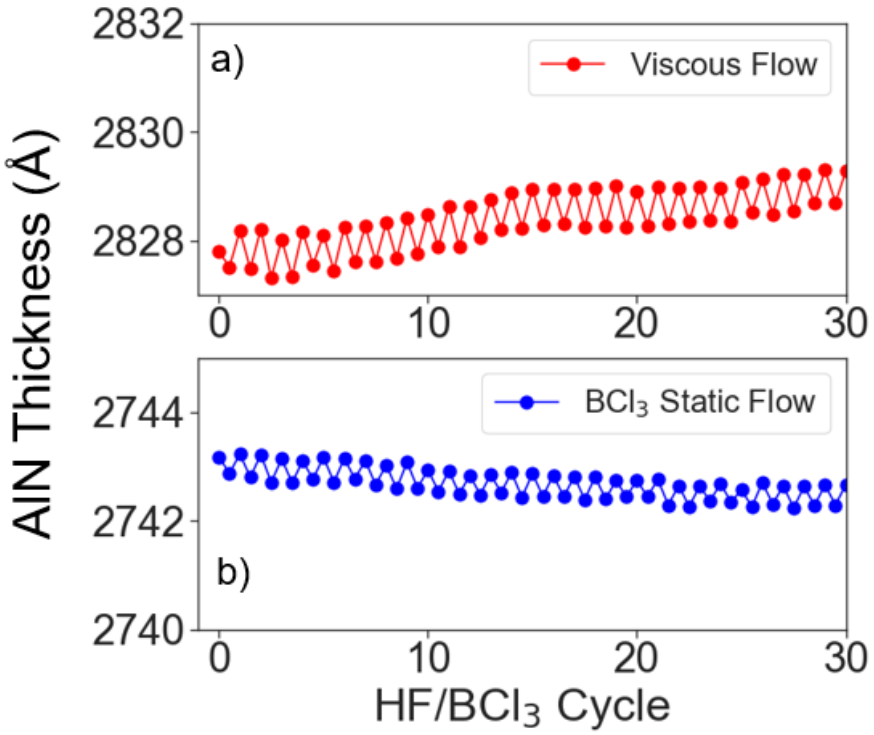

Figure 4-6: Ellipsometry measurements of HF and BCl_3 on aluminum nitride at 298ºC using a) viscous exposures of BCl_3 and b) static exposures of BCl_3 with a setpoint of 2.5 Torr and an exposure time of 20 seconds

To investigate crystalline aluminum nitride samples, in-situ spectroscopic ellipsometry was employed. This in-situ ellipsometry tool has different thermal limitations than in-situ infrared spectroscopic. A maximum temperature of 300ºC possible was used. Etching was first attempted with alternating exposures of HF and BCl_3 shown in Figure 4-6a at 298ºC. Figure 4-6 shows the thickness after each half-cycle during 30 cycles of HF and BCl_3 with the BCl_3 exposure done in viscous flow (a) and in static flow (b) where the BCl_3 setpoint was 2.5 Torr and the static dose time was 20 seconds. In Figure 4-6b After 30 cycles of HF and BCl_3 done in viscous flow there was a small thickness increase. This is good evidence that no etching occurs on the crystalline aluminum nitride. This was also true of temperatures below this temperature.

This contrasts with etching seen at 300ºC during HF and BCl_3 etching of ALD grown aluminum nitride in Figure 4-4. While trying static exposures of BCl_3 there was no evidence of etching either. While there were small thickness changes during each half-cycle, only an extremely small etch rate of 0.02 Å/cycle was observed during static flow. It can be difficult to postulate on the etching rate of a material using infrared spectroscopy like in Figure 4-2, but it seems likely the etching rate for the ALD grown aluminum nitride is very different than with the single crystal aluminum nitride. This lack of etching was determined to be due to the HF not being able to fluorinate the crystalline aluminum nitride well. To fluorinate aluminum nitride xenon difluoride (XeF_2) was explored as a stronger fluorination source.

The etching of aluminum nitride with XeF_2 and BCl_3 was conducted at 255°C. The dosing sequence was first the XeF_2 was pulsed into the reactor for one second then purged for 40 seconds before taking an SE measurement. F or the BCl_3 exposure, BCl_3 was pulsed into the chamber until the partial pressure of BCl_3 reached a desired setpoint, normally 2 Torr, and was held in the chamber statically for a desired time, usually 20 seconds before being pumped out and purged with N_2 for 60 seconds before a SE scan. To investigate whether aluminum nitride will etch with XeF_2 and BCl_3, spectroscopic ellipsometry was used to measure any changes in thickness of the aluminum nitride film.

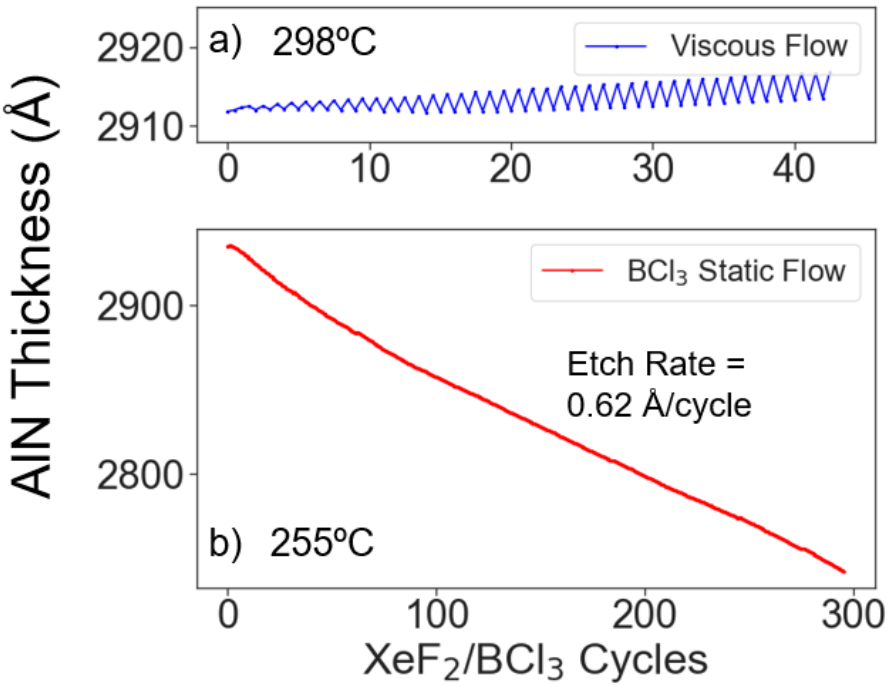

Figure 4-7: SE measurements of the ALE of AlN over 300 XeF_2 and BCl_3 cycles at 255ºC during a) viscous flow of XeF_2 and BCl_3 and then b) in viscous flow of XeF_2 and static flow of BCl_3

Figure 4-7 shows ellipsometry results of aluminum nitride etching at 255ºC. In Figure 4-7a there are visous exposures of XeF_2 and BCl_3. There was no etching seen over 50 cycles at 298ºC. There is good evidence that XeF_2 should be able to fluorinate aluminum nitride. This lack of etching was likely due to BCl_3 not being able to remove the created fluoride. Figure 4-7b shows the etching of aluminum nitride when BCl_3 is statically exposed to the surface. The aluminum nitride thickness decreases linearly as a function of XeF_2 and BCl_3 over 300 cycles with an etch rate of was 0.62 Å/cycle. There is an optical thickness decrease during the XeF_2 exposure with an average thickness decrease of 0.32 Å. This is likely due to the fluorination reaction of XeF_2 with the aluminum nitride but also a loss of chlorine from the surface. This might result in a negative optical thickness change. The fluorination reaction will be discussed

more in Figure 4-8. The fluorination of aluminum nitride would have a volume expansion. There is a thickness decrease during the BCl_3 exposure with an average decrease of 0.33Å. This is likely due to the removal of the fluoride created during the previous XeF_2 exposure.

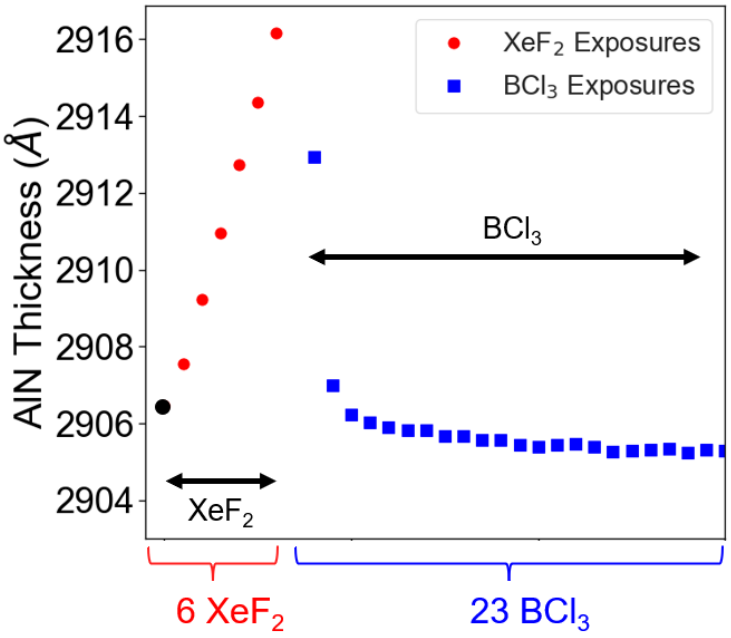

Figure 4-8: AlN thickness measurements measured by ellipsometry at 298ºC showing 6 XeF_2 exposures followed by 23 viscous BCl_3 exposures

Figure 4-8 shows the fluorination reaction for six exposures of XeF_2 on aluminum nitride. This is followed by 23 exposures of BCl_3. The fluoride that is created in the XeF_2 exposure is quickly removed by the first few BCl_3 exposures. After this sequence there is a net thickness loss of 1.3 Å. This thickness loss can be controlled by the XeF_2 exposure as well as the BCl_3 exposure. The reaction is not self-limiting as seen by continual thickness increase over six XeF_2 exposures. The average thickness increase per XeF_2 exposure was 1.6 Å. The continual thickness increase means the XeF_2 fluorination reaction with aluminum nitride is not fully self-limiting. To

get constant fluoridation reactions only a one second XeF_2 exposure is used. This will partially fluorinate the surface and keeps the fluorination constant at each temperature. It is expected with larger fluoride creation that there is a larger etch rate as the ligand-exchange reaction spontaneously etches the entirety of the fluoride.[101] This is seen with the 1.3 Å single cycle etch rate, in comparison to 0.9 Å/cycle etch rate seen in Figure 4-9. What is also expected is a self-limiting etching reaction with respect to the BCl_3 exposures. With no aluminum fluoride to react with BCl_3 does not etch, nor add to the surface.

The temperature dependence of the etching reaction can also help understand the etching pathway. Figure 4-9 shows the etching rate at 213ºC, 230ºC, 255ºC, 263ºC, 280ºC, and 298ºC. The process conditions were a 1 second exposure of XeF_2 followed by a 20 second static BCl_3 exposure with a pressure setpoint of 2 Torr. At 213ºC the etch rate was only 0.19 Å/cycle most likely due to the weak ligand exchange at that temperature. This is close to the temperature that was seen at which the onset of etching is believed to occur. This will be discussed more in Figure 4-12. This is most likely due to the temperature dependence of the ligand-exchange reaction and the volatility of the likely product $AlCl_3$. At temperatures 230ºC to 298ºC the etching rate increased slightly. This is most likely due to slightly increased rates of fluorination at 230ºC than at 298ºC. The etch rates were 0.56 Å/cycle, 0.58 Å/cycle, 0.68 Å/cycle, 0.73 Å/cycle, and 0.93 Å/cycle at 230ºC, 255ºC, 263ºC, 280ºC, and 298ºC respectively. It is likely the onset of etching would occur around 207ºC based on fits of the etch rate near the onset temperature.

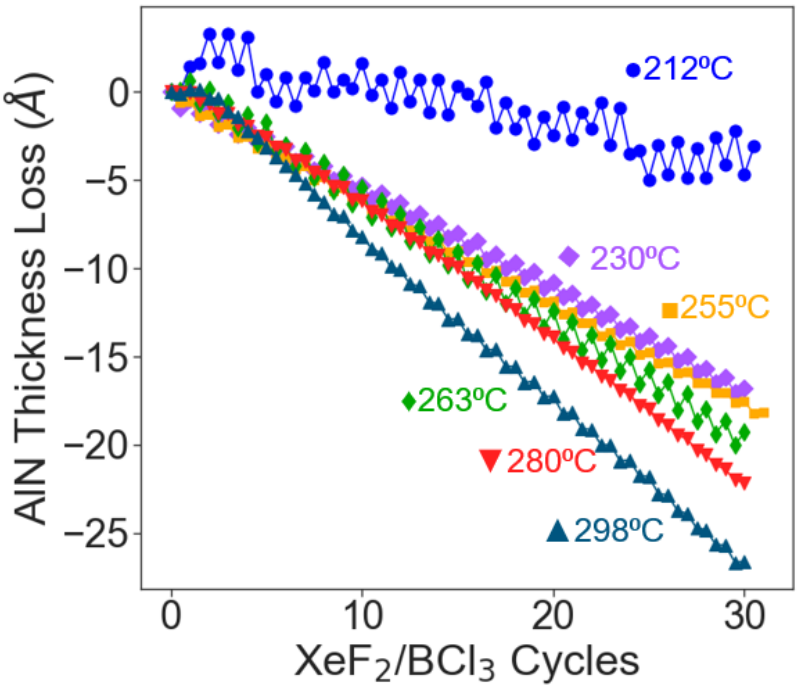

Figure 4-9: Etch rate changes as a function of the substrate temperature during ALE of AlN with XeF_2 and BCl_3

Figure 4-10 shows the etch rate dependence on the total BCl_3 exposure from 0 to 130 Torr seconds. At 4 Torr seconds the etching rate was approximately 0.41 Å per XeF_2/BCl_3 cycle at 255ºC. This etch rate nearly doubled to 0.81 Å per XeF_2/BCl_3 cycle when BCl_3 was exposed to the aluminum nitride substrate for 125 Torr seconds. The long exposure dependence of the etch rate on the BCl_3 exposure likely means the ligand-exchange reaction on the fluorinated crystalline aluminum nitride is kinetically slower than with the ALD grown aluminum nitride. There is an initial increase in the etch rate at lower BCl_3 exposures but takes much more BCl_3 to remove the rest of the aluminum fluoride created. This is likely due to a gradient of fluoride during the first few layers of aluminum nitride. The more fluorinated layer of aluminum nitride may undergo ligand-exchange reactions at a higher rate than sub fluorides of aluminum.

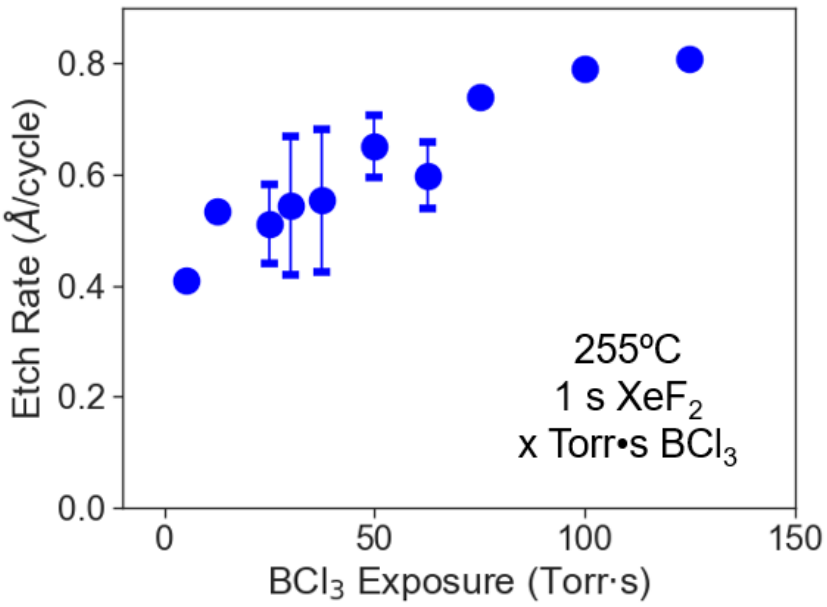

Figure 4-10: Etch rate changes as a function of the BCl_3 exposure during ALE of AlN with XeF_2 and BCl_3 at 255ºC

To investigate the fluoride on the surface ex-situ x-ray photoelectron spectroscopy (XPS) was used. The aluminum fluoride peak in XPS is centered somewhere from 76-77.5 eV[41-42, 102]. This is distinctly different when compared to the aluminum nitride peak centered at 73.6 eV or the aluminum oxide peak at 74.7 eV.[42, 102-103] 50 cycles of XeF_2 and BCl_3 were conducted where Figure 4-11a was where etching was finished on a XeF_2 exposure and Figure 4-11b where etching was finished on a BCl_3 exposure. In Figure 4-11a there is clear multiple peaks in the Al 2p region. The peaks were constrained by their locations and the F.W.H.M that were expected for the peak. Two peaks were found at 73.6 eV and 74.7 eV. These are consistent with Al-N and Al-O binding energies. The Al-O peak is likely due to air that reacted with the sample during transfer from the etching chamber to the XPS analysis tool. Another peak was found at 77 eV

which was consistent with Al-F binding energies. This spectrum is consistent with a fluorinated aluminum nitride film. The peak located at 78.2 eV is most likely from small amounts of copper contamination on the sample as it is close to the Cu 3p XPS peak.[104] Figure 4-11b shows the sample after ending the etching on a BCl_3 exposure. There is only a single peak in this spectrum which is consistent with Al-N binding energies. This spectrum argues for only aluminum nitride remaining after BCl_3 exposures. That means all the fluoride that was created, represented in a was removed by the BCl_3 exposure. These spectra also argue for fluorination of the aluminum nitride followed by the removal of that fluoride by BCl_3 via a ligand-exchange process. Peaks were held at a FWHM of 2.4 eV and a L/G ratio of 0.7. Other areas of the spectrum will be discussed later in this paper.

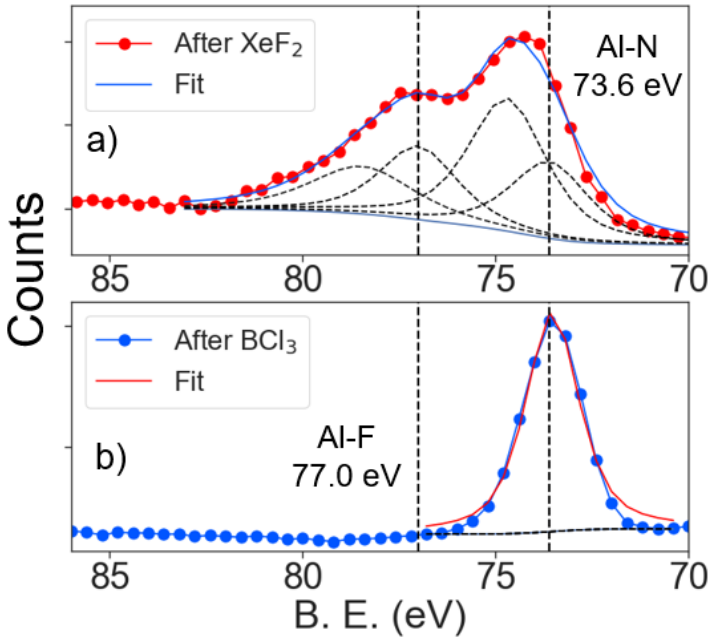

Figure 4-11: X-ray photoelectron spectra of the Al 2p region after a) XeF_2 exposure and b) after the BCl_3 exposure

To help understand the ligand-exchange reaction mass spectrometry was done to look at the volatile etch products. Figure 4-12a is the mass spectrum recorded after BCl_3 is flown through an AlF_3 powder. Most of the gaseous species seen are the product of ligand-exchange reactions between AlF_3 and BCl_3. Single ligand-exchange where a BCl_3 molecule exchanges a single chlorine with a single fluorine from the surface resulting BCl_2F. Double and complete ligand-exchange is also seen with the products $BClF_2$ and BF_3 respectively. Along with the boron ligand-exchange product there is the aluminum-based volatile etch product in $AlCl_3$. This was the predicted etch product given the melting point of $AlCl_3$ is 192.4ºC.[105] Figure 4-12b shows the m/z range from 130 to 139 amu where the parent $AlCl_3^+$ can be found. The spread of the BCl_3 parent peak is due to the two abundant isotopes of boron (20% ^{10}B, 80% ^{11}B) and the two main isotopes of chlorine (76% ^{35}Cl, 24% ^{37}Cl). The red bars indicate what is expected from the isotopic signatures of Cl and Al. The peak at 132 amu is the peak with 100% relative abundance and the intensity of other lines are 97.2%, 31.5%, and 3.4% of the 132 amu peak for 134 amu, 136 amu and 138 amu respectively. This is good evidence that the peak at 132 is definitively from $AlCl_3$.

Temperature dependence of the reaction of BCl_3 with AlF_3 was looked at as well. Figure 4-13 shows the temperature dependence of the boron containing compounds (a) and the aluminum containing compounds (b). As the temperature is increased from room temperature there is little deviation from background until around 200ºC at which point the reactant BCl_3 intensity starts to drop as well at the same time BCl_2F and $BClF_2$ begin to increase. This is the first indicator that the onset of ligand-exchange reactions has begun. Also, at 200ºC the $AlCl_3^+$ peak begins to rise. This temperature correlates well with the onset of etching seen in Figure 4-4 as well as Figure 4-9, where there is noticeable etching seen only as the substrate temperature

increases above 200ºC. As the vapor pressure of $AlCl_3$ rises there becomes more $AlCl_3^+$ that becomes volatile and the intensity of the $AlCl_3^+$ and $AlCl_2^+$ shown increase. Interestingly, as the temperature approaches 330ºC the amount of BCl_3 that undergoes just one or two ligand exchanges decreases and the intensity of the full ligand exchange reaction increases. This likely means as temperature increases it becomes more thermodynamically favorable for BCl_3 to ligand-exchange three times with AlF_3.

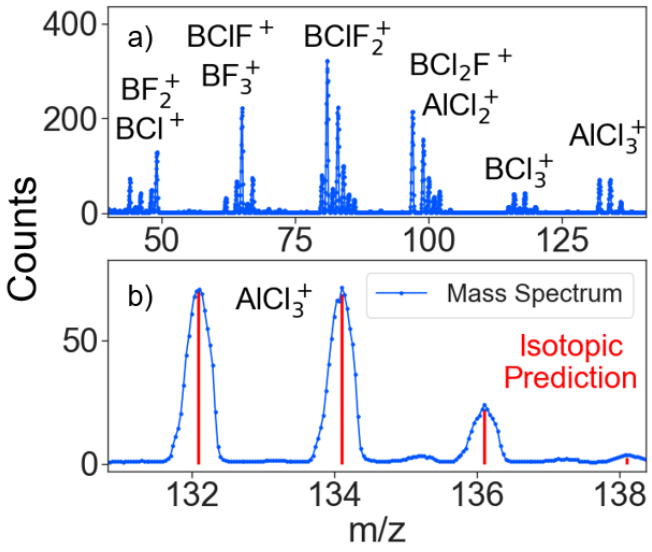

Figure 4-12: Mass spectrum of the BCl_3 exposure on AlF_3 powder a) from 40-140 amu and b) a close up on the region from 131 to 139 amu

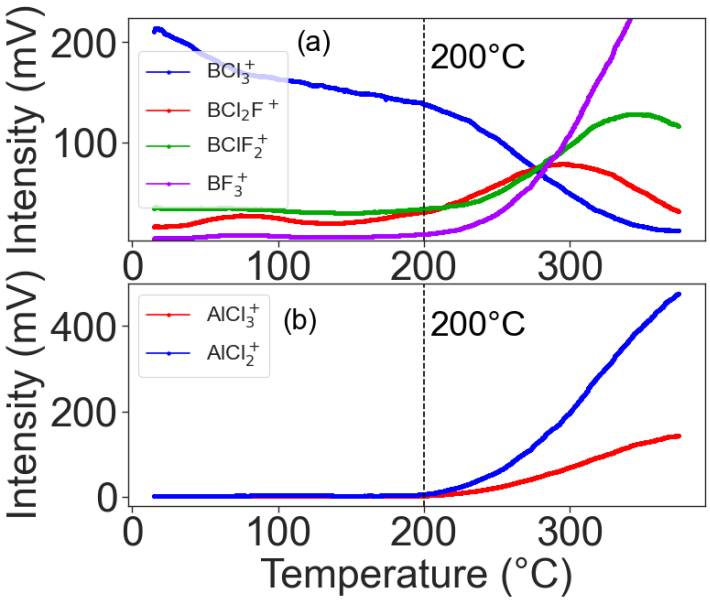

Figure 4-13: Mass traces a) for boron containing species and b) aluminum containing species as a function of substrate temperature

When studying the fluorination of aluminum nitride with ex-situ XPS, it became evident that there was some chlorine and fluorine contaminants which varied from 5-10 atomic percent for both fluorine and chlorine. To remove some of those surface contaminants, exposures of water were implemented into the cycle. Figure 4-14 shows the aluminum nitride thickness change as a function of $XeF_2/BCl_3/H_2O$ cycles. The procedure starts with a one second XeF_2 exposure followed by a 20 second BCl_3 static exposure at 2.5 Torr. The cycle ends with a one second water pulse of ~80mTorr. At 255ºC there is linear etching with an etching rate of 0.49 Å/cycle. This is decreased from 0.62 Å/cycle without water as shown in Figure 4-7.

This was proposed to be the result of surface contamination with fluorine and chlorine starting to build up on the surface. In Figure 4-14 after a slight decrease in the MSE, the error

was completely consistent during 100 cycles of $XeF_2/BCl_3/H_2O$. This was an indication of possible halogen removal from the surface.

To further investigate the surface contamination during etching XPS was done after 50 cycles of different etching processes. XPS was taken after 50 cycles of XeF_2/BCl_3, after 50 cycles of $XeF_2/BCl_3/H_2O$, and after 50 cycles of XeF_2/BCl_3 and ending with one five second water exposure. The atomic percentage of Al, N, O, F, and Cl are plotted in Figure 4-15 for the three different etching conditions along with a survey spectrum of the aluminum nitride wafer with no etching. The adventitious carbon was removed from the atomic percentage. The XeF_2 and BCl_3 etching showed 10.5% chlorine and 6% fluorine on the surface after etching. When using H_2O as the third reactant there was 11% chlorine and 4% fluorine on the surface. This showed that although the MSE was more controlled, there was no real effect on the halogenation of the surface. After 50 cycles of XeF_2 and BCl_3 but the etching was ended with a 5 second H_2O pulse, the chlorine dropped to 0.6% and the fluorine dropped to 3.4%. This showed that water can be an effective remover of chlorine and fluorine on the surface but that there was no difference if the pulse was done after the etching was done or in the cycling process. In addition to the low fluorine and chlorine content, the oxygen remaining was lower than the survey and the ABC process at 13.4% oxygen on the surface.

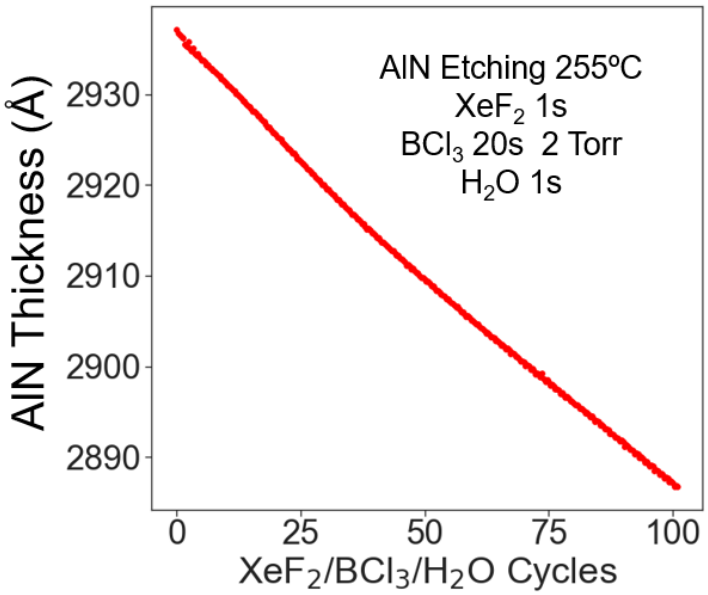

Figure 4-14: SE measurements showing the ALE of AlN using XeF_2, BCl_3 and H_2O exposures

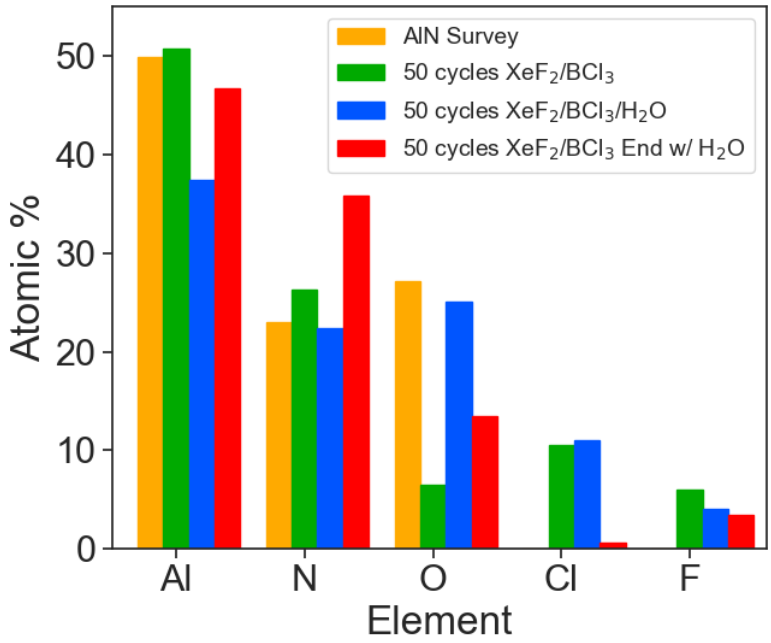

Figure 4-15: Atomic percentage of various elements measured by XPS after ALE of AlN using XeF_2 and BCl_3 etching (green), XeF_2, BCl_3 and H_2O etching (blue) and XeF_2/BCl_3 etching ending with a 5 second H_2O exposure (red) compared to a unetched AlN sample (orange)

4.5 Conclusions

This study presented work showing atomic layer etching of different forms of aluminum nitride. First aluminum nitride growth and etching were observed using in-situ infrared spectroscopy. The growth was done with TDMAA and NH_3 while the etching was observed with HF to fluorinate and BCl_3 to ligand exchange with the fluoride. The loss in the Al-N vibrational band per cycle increased from 200ºC to 350ºC, where at 200ºC there was no observable etching. To investigate the etching characteristics of high-quality aluminum nitride, a single crystal aluminum nitride on sapphire wafer was used. Etching was first attempted with HF and BCl_3 although no etching was seen in either viscous flow or static flow. Ellipsometry showed linear etching over hundreds of cycles when XeF_2 and BCl_3 was used, but only when long static exposures of BCl_3 were used. There were slight increases of the etching rate with temperature in this system which was attributed to increased fluorination at increased temperatures. The volatile etch products were investigated with in-situ quadrupole mass spectrometry where the BCl_3 reaction of AlF_3 powder was focused on. $AlCl_3$ was the aluminum etch product, which was seen in tandem with $BFCl_2$, BF_2Cl and BF_3 which is consistent with exchange of the precursor ligands with fluorine on the surface. The onset of ligand-exchange was seen at 200ºC which matches well with the onset of etching seen on ALD grown AlN using infrared spectroscopy and single crystal AlN using spectroscopic ellipsometry. This process showed fluorine and chlorine contamination after the etching was done shown by XPS. These contaminants can be removed form the surface with H_2O exposures. XPS also confirmed the presence of aluminum fluoride after XeF_2 exposures and removal of the fluoride after BCl_3 exposures.

4.6 Acknowledgements

The FTIR and SE studies were funded by Intel through a member specific research grant through the Semiconductor Research Corporation (SRC). Support for the new QMS reactor and the QMS investigations was provided by Lam Research.

Atomic Layer Etching of Aluminum Oxide with HF and BCl_3

Austin Cano, Jonathan Partridge, Steven M. George

Department of Chemistry, University of Colorado at Boulder, Colorado 80309, USA

5.1 Abstract

The atomic layer etching of aluminum oxide with HF and BCl_3 is explored. Infrared spectroscopy is utilized to observe the growth and subsequent etch of aluminum oxide with HF and BCl_3. Infrared difference spectra show that the main reaction pathway during etching is of fluorination by HF and then removal of the fluoride with BCl_3. BCl_3 has shown characteristics of conversion reactions creating boron oxide from tungsten oxide. BCl_3 also shows evidence of conversion reactions of aluminum oxide to boron oxide. On initial exposures of BCl_3 on aluminum oxide there is a conversion of the aluminum oxide to boron oxide shown by a decrease in the Al-O vibrational band and increase in the B-O vibrational band. Subsequent HF exposures can remove the boron oxide that forms from the BCl_3 exposure. Subsequent BCl_3 exposures do not convert much of the underlying aluminum oxide. Ellipsometry measurements showed thickness loss as a function of the number of HF and BCl_3 cycles. The volatile products were analyzed using mass spectrometry and saw the ligand-exchange product of $AlCl_3$ and BCl_2F.

5.2 Introduction

Atomic layer etching (ALE) is a technique that can remove sub-angstrom amounts of material by using sequential surface reactions.[10, 12] Thermal ALE has been a growing field where the energy used in the ALE reaction comes from heat instead of a plasma source.[1-2, 12] Thermal

ALE has been typically done by first modifying a surface with a fluorination agent such as HF, SF_4 or XeF_2.[14-15, 22] This modification can also be done with a fluorine based plasma.[106] This changes the surface from either a nitride or oxide to a fluoride. These fluoride materials have been shown that they can be removed by various precursors via a ligand-exchange, or ligand addition reaction.[107]

Boron trichloride (BCl_3) is a precursor that has been used for thermal ALE reactions in the past although the mechanism was not thoroughly studied.[15, 61] Previous reports have suggested that BCl_3 may etch via a conversion reaction where the surface is converted into boron oxide and the metal is volatilized. This boron oxide can then be spontaneously etched by a fluorine source like HF. BCl_3 may also undergo thermal ALE by a ligand-exchange reaction as seen in Chapter 4. The removal of a fluoride by a ligand-exchange reaction works because the reaction creates products which both have good vapor pressures or volatile dimers of the surface fluoride and precursor.[23]

Trimethyl aluminum (TMA) is another precursor used in thermal ALE that has also been shown to remove surface fluorides by ligand-exchange.[16-17, 22, 98] TMA has also been the study of the etching of silicon oxide with HF.[17] Interestingly when etching silicon oxide, TMA was able to convert the silicon oxide into an aluminum oxide by the reaction $SiO_{2(s)} + TMA_{(g)} \rightarrow Al_2O_{3(s)} + Si(CH_3)_{4(g)}$. This made the etching possible as aluminum oxide ALE has been performed previously.[20, 22] The ability to create both ligand exchange reactions as well as conversion type reactions makes TMA a valuable precursor to study. This could also be true for BCl_3 but more study of the reaction mechanisms needs to be done.

For this study thermal ALE of aluminum oxide with HF and BCl_3 was explored. Infrared spectroscopy was used to understand surface compositional change during cycling of HF and

BCl_3. The bulk Al-O vibrational band was used as a measure of growth and etching of aluminum oxide. In-situ spectroscopic ellipsometry measurements were used to understand film thickness changes during ALE cycles. Quadrupole mass spectrometry is also explored to understand volatile etch products created during both the HF and BCl_3 half reactions.

5.3 Experimental

In-situ infrared spectroscopy was done in a warm walled viscous flow reactor. A more detailed description of this reactor can be found in previous work.[92] The reactor is heated by a ceramic custom heater from Watlow. The wall temperature was kept at 150ºC during deposition and etching experiments. To increase the sample temperature, the sample was resistively heated by a HP 626B direct current power supply. This heating was controlled with a 16B PID Love controller. The initial substrate was silicon nano powder with an average diameter of 30-50 nanometers. The silicon particles have a native oxide that can be seen throughout growth and etching studies. This silicon powder is pressed into a 3cm by 1.7cm tungsten grid with grid spacings of 50 microns with 100 gridlines per inch. This grid has tantalum foil spot welded on each side for good electrical contact to the resistive heating lines. A type-k thermocouple is attached to the tungsten grid with an insulating epoxy (Ceramabond, Aremco 571).

FTIR spectrum was obtained with a Nicolet 6700 spectrometer. The light was generated with a glow bar light source and used a KBr beam splitter and then was redirected into a viscous flow tube where the light passed through the silicon powder sample. The light then was directed to outside the reactor to an MCT-B detector. Vacuum was maintained by two KBr windows which are separated from the etching and deposition chemistry by gate valves and only opened while obtaining a spectrum. Final spectra were averaged for 100 scans with a resolution of 4 cm^{-1}

and data spacing of 0.482 cm^{-1}. Backgrounds were collected before each experiment was conducted.

Aluminum oxide deposition in the in-situ FTIR reactor was done with trimethyl aluminum (TMA) obtained from Sigma-Alrich (99.5%), and chemical grade water. The deposition was done at 150ºC and used 1 second of TMA and 2 seconds of H_2O. The etching studies were done with HF-pyridine and BCl_3. Boron trichloride cylinder was purchased from Synquest Chemicals (BCl_3, 99%). The HF used in these experiments were derived from HF-pyridine (70% HF, 30% pyridine) and was purchased from Millipore-Sigma. The HF-pyridine was transferred into a bored out stainless-steel bubbler that was gold-plated bubbler to minimize corrosion on the stainless-steel container. A carrier gas of UHP N_2 was used and FTIR experiments which had a flow of 100 sccm for a transient N_2 pressure of 1.5 Torr.

In-situ ellipsometry deposition and etching experiments were done in a home built in-situ chemical reactor reported on previously.[61] The reactor is a warm walled with a resistive heater which elevates the sample temperature above that of its surroundings with a sample temperature limit of 300ºC. The polarized light hits the sample at a 70° angle from normal and is fixed at this angle. A spectroscopic ellipsometer (M-2000, J. A. Woollam) was used for all ellipsometry experiments. Wavelengths from 240nm to 1700nm were used in the fitting of the film optical properties. The Ψ and Δ parameters were analyzed with the CompleteEASE software package (J. A. Woollam). Silicon substrates with a native oxide were used as the substrates for aluminum oxide ALD. The aluminum oxide Cody Lorentz model was used to fit the aluminum oxide deposition. Aluminum oxide was deposited in the ellipsometry tool with trimethyl aluminum (TMA) and ozone. The ozone was generated by an Ozonia ozone generator. TMA was purchased

from Sigma-Alrich (99.5%). The etching with HF-pyridine and BCl_3 was done with the same chemicals used in the

Quadrupole mass spectrometry was done in a new reactor described previously.[101] The volatile etch products were observed using quadrupole mass spectrometer (Extrel, MAX-QMS Flanged Mounted System. An electron ionization energy of 70 eV was used for these experiments. To minimize exposures to corrosive gaseous species the ionizer and analyzer were positioned perpendicular to the incoming molecular beam. AlF_3 powder was purchased from US-Nano Research Materials (99.5%).

5.4 Results and Discussion

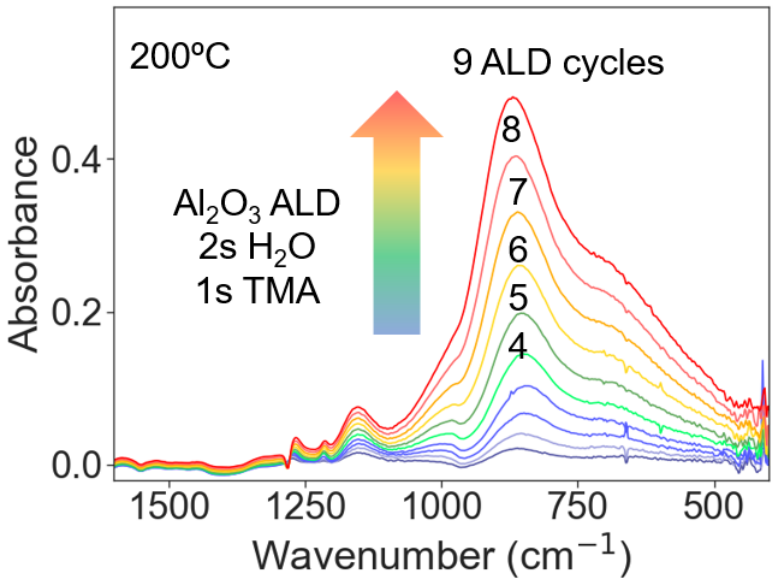

Figure 5-1: Infrared spectra between 1600 and 400 cm^{-1} showing the growth of aluminum oxide over 9 ALD cycles with TMA and H_2O at 200°C taken after H_2O exposures.

To study the etching of aluminum oxide using infrared spectroscopy first aluminum oxide must be deposited on the silicon substrate. Figure 5-1 is the growth of ALD aluminum oxide

with TMA and H_2O. The spectra show the growth of the Al-O stretching mode at 850 cm^{-1}.[20, 82] This vibrational mode increases with increasing number of cycles over the course of 9 ALD cycles. The peak at 1130 cm^{-1} is assigned to the Si-O-Al vibrational mode that is formed during the initial stages of growth between the interface of the silicon native oxide and the aluminum oxide deposited. The spectra shown are all after H_2O exposures. After the TMA exposures peaks at 1215 cm^{-1} and 2900 cm^{-1} can be seen which are assigned to the Al-CH_3 deformation peak and the C-H stretch respectively.[17, 22]

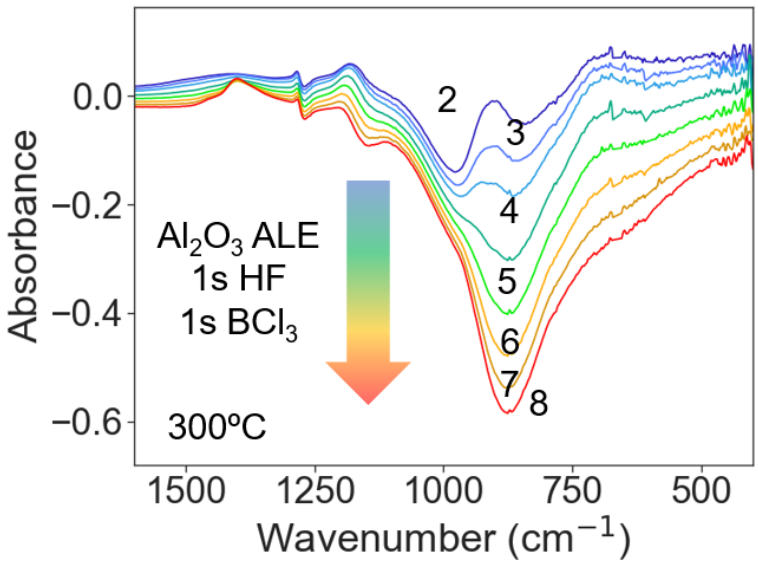

Figure 5-2: Infrared spectra of aluminum oxide ALE using HF and BCl_3 at 300°C after 8 cycles.

Infrared difference spectra taken after HF and BCl_3 cycles referenced to the aluminum oxide ALD film are shown in Figure 5-2. Here there is clear evidence of etching shown by the decrease in the Al-O vibrational band at 850 cm^{-1}. Initially there is a large decrease in the Al-O vibrational band. This absorbance loss continues as the cycles of HF and BCl_3 continue. There is

a small increase in the B-O vibrational mode seen at 1370 cm^{-1}.[108] This decrease in the Al-O vibrational band has the largest decrease in the initial cycles as compared to later cycles. This is likely due to there being less aluminum oxide on the nanoparticle substrate. This could be due to inconsistent deposition during aluminum oxide growth. No peaks were seen with a higher frequency than the B-O vibrational mode.

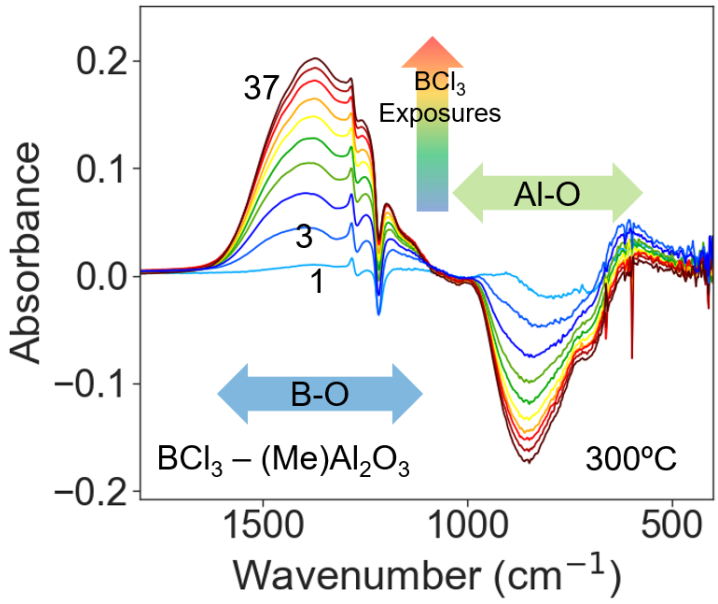

Figure 5-3: 37 BCl_3 exposures at 300ºC in viscous flow showing the loss of the Al-O vibrational band happen concurrently with the gain in the B-O vibrational band

There has been recent literature on BCl_3 possibly being used as a conversion reagent for the etching of WO_3 as well as GaN.[15, 61] For that reason the BCl_3 half reaction was important to focus on to see if there was similar chemistry driving the etching reaction of aluminum oxide. Figure 5-3 shows the difference spectra of 37 BCl_3 exposures referenced to the last TMA exposure after aluminum oxide atomic layer deposition. A methylated surface was used in order to remove the side reaction of BCl_3 with hydroxyl groups which would also produce B-O

stretching vibrations. In Figure 5-3 there is a clear loss of Al-O absorbance and a clear gain in B-O absorbance. This loss of one metal oxide and gain of another is evidence of the conversion reaction depicted in previous literature. Importantly the reaction does not seem to initially self-limit. Continued BCl_3 exposures simply removes more aluminum oxide from the surface and creates more boron oxide. There is a negative feature at 1215 cm^{-1} which is assigned to the aluminum methyl deformation stretch which is due to the surface being methyl terminated. Not shown is the loss of the C-H stretching vibrations during the first BCl_3 exposure which indicates that the terminal methyl groups are immediately volatilized.

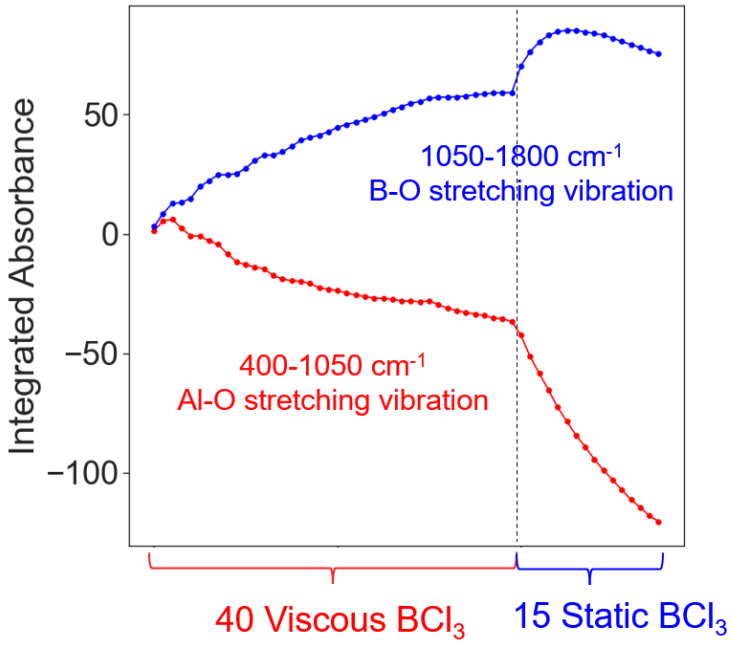

Figure 5-4:Integrated absorbance in IR difference spectra from 400 to 1050 cm^{-1} (blue) and 1050 to 1800 cm^{-1} red showing the increase of the B-O vibrational band in blue and the Al-O vibrational band in red during many BCl_3 viscous and static exposures.

To visualize how the BCl_3 converted the aluminum oxide into boron oxide the integrated absorbance was monitored for the Al-O and B-O bands shown in Figure 5-4. The result of the 56 BCl_3 exposures can be found in Figure 5-3a. Initial exposures showed a decrease in the Al-O band and increase in the B-O band. The conversion of the Al-O to B-O happens within the first few BCl_3 exposures. The amount of Al-O converted into B-O slowed as the number of exposures continued. After 40 viscous exposures of BCl_3 there were 16 more BCl_3 exposures that were with a setpoint of 1 Torr of BCl_3 statically for 5 seconds. When there were static exposures of BCl_3 the increase of the B-O and decrease of the Al-O accelerated. The Al-O showed continued loss during the 16 static BCl_3 exposures. This is likely due to increased conversion of the aluminum oxide surface to boron oxide. The B-O did not increase after the first 8 exposures. After 8 static BCl_3 exposures there showed a loss in the B-O vibrational mode as well. This is likely due to volatilizing some of the B-O on the surface to BCl_3 or other volatile compounds such as $B_3O_3Cl_3$. This may make it easier for the conversion of aluminum oxide to occur since it may decrease the length that the $AlCl_3$ product may need to diffuse to reach the surface to volatilize. This could indicate that BCl_3 might be able to spontaneously etch aluminum oxide although this reaction was not investigated.

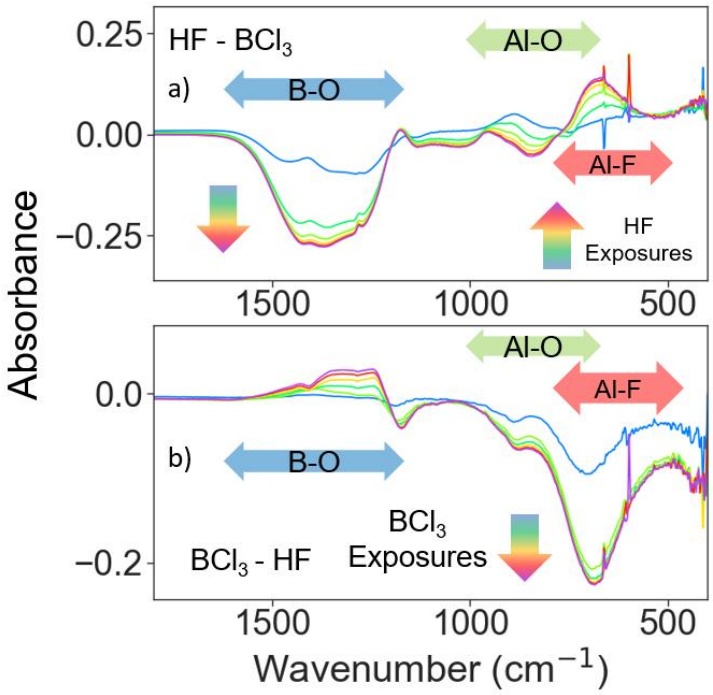

Figure 5-5: Infrared difference spectra of 37 BCl_3 exposures on aluminum oxide ALD ending on a TMA exposure.

The BCl_3 reaction with aluminum oxide was further studied by doing many consecutive exposures of BCl_3 on aluminum oxide**.** The initial exposures of BCl_3 and HF where slightly different than etching in later cycles. Figure 5-5a and Figure 5-5b shows the difference spectra of the next cycle after the first BCl_3 exposure on Al_2O_3 shown in Figure 5-3. On the first BCl_3 exposure there was a clear loss in absorbance at 900 cm^{-1} and a gain in absorbance at 1370 cm^{-1}. This is consistent with conversion reactions seen previously.[16-17, 98] On the subsequent HF exposure, the boron oxide is removed seen by the large decrease from 1200-1600 cm^{-1} which is close to the amount of B-O formed in the previous BCl_3 exposure. While the HF removed most of the B-O formed, there was still a small vibrational mode which persisted throughout 20 HF exposures. This is consistent with previously studies on the HF reaction with B_2O_3 as well in

Chapter 6.[61] There is also an increase in the Al-F peak increase seen at 680 cm^{-1}. This comes from the fluorination of the aluminum oxide under the boron oxide converted layer. There is also evidence of the loss of aluminum oxide during the HF exposure as well at 850 cm^{-1}. These spectra would be consistent with the removal of the boron oxide converted layer, then the fluorination of aluminum oxide.

The subsequent 20 BCl_3 exposures are shown in Figure 5-5b. This spectrum is quite different than the BCl_3 exposure shown in Figure 5-3. Firstly, the amount of B-O created is much smaller than the B-O formed during initial exposures of BCl_3. This comes in conjunction with small change in the Al-O vibrational modes. There is still some loss of Al-O and small gain in B-O, but it is diminished from the first exposure. The main feature in the difference spectra is the loss of a mode at 690 cm^{-1} which is assigned to Al-F loss. This is consistent with the formation of Al-F created during the previous HF exposure. This fluorination of aluminum oxide in the HF exposure and then subsequent removal in the BCl_3 exposure is consistent with fluorination and ligand exchange reactions.

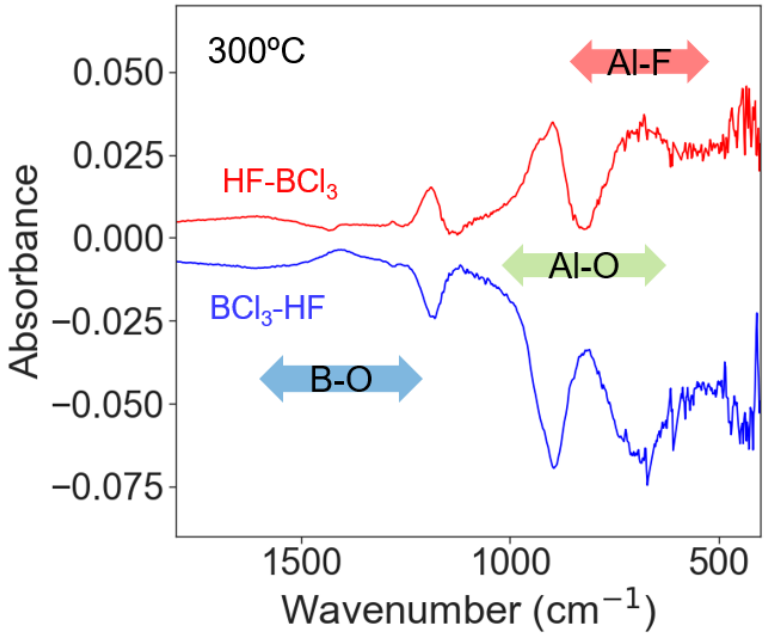

Figure 5-6: Infrared difference spectra after the HF exposure (red) and the BCl_3 exposure and after one complete cycle (orange).

Difference spectra were looked at after the HF and BCl_3 exposures. Figure **5-6** shows the difference spectra after the HF exposure (red) and the BCl_3 exposure (blue) each referenced to the previous exposure. The overall change in the spectrum over one cycle is also shown in orange. During the HF exposure there is an increase in absorbance at 680 cm^{-1}. This is the Al-F formation. This same Al-F feature is then lost during the subsequent BCl_3 exposure. This would be consistent with fluorination and then ligand-exchange, removing the fluoride form the surface. After the BCl_3 exposure there is a loss in absorbance which is consistent with the Al-F vibrational band. This is due to the removal of the aluminum fluoride in the BCl_3 exposure. A similar reaction can be seen in the BCl_3 exposure during aluminum nitride etching in Figure 4-3. Additionally, both the HF and BCl_3 exposures show little change in the B-O vibrational mode. Only a small change occurs during the BCl_3 exposure. This could mean that while there is

conversion happening on the surface of the film, the dominant pathway to etching is by fluorination and removal of that fluoride. Other peaks at 900 cm^{-1} and 1130 cm^{-1} are tentatively assigned to Al-F and B-F-Al respectively.

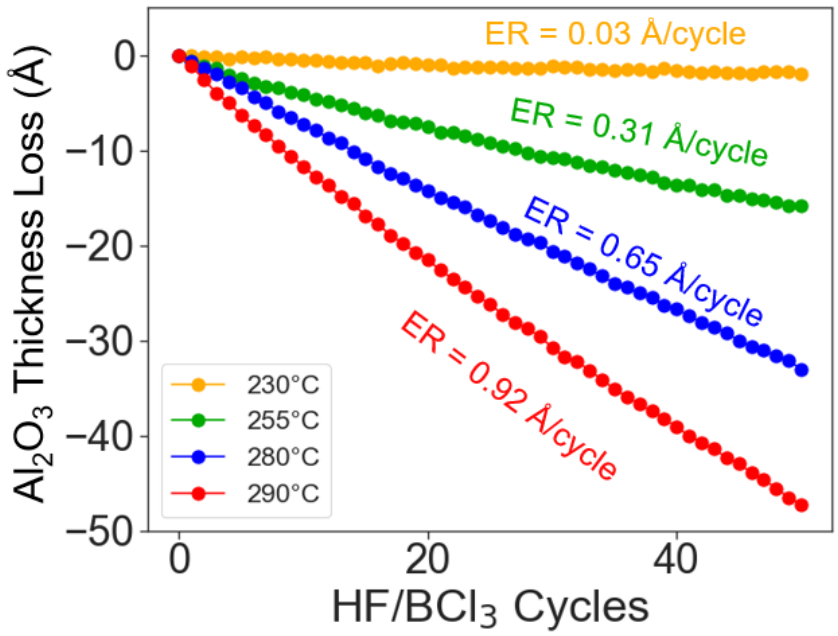

Figure 5-7: Ellipsometry thickness measurments of aluminum oxide etching at 230ºC, 255ºC, 280ºC and 298ºC with HF and BCl_3

Ellipsometry measurement of aluminum oxide etching with HF and BCl_3 were also done. Figure 5-7 shows the thickness measurements after each cycle for 50 ALE cycles. At 230ºC there was no discernable etching seen with an etch rate of only 0.03 Å/cycle. Over 50 cycles that was just a decrease in aluminum oxide thickness of 1.5 Å. When the substrate temperature was increased to 255ºC the etch rate increased to 0.31 Å per cycle. This trend in increased etch rate with increasing temperature was true at 280ºC and 298ºC with an etch rate of 0.65 Å per cycle and 0.92 Å per cycle respectively. This trend of increased etching was likely due to increased

fluorination with increasing temperature which has also been seen previously.[21-22, 55] Linear etching was seen at each temperature. These results show that temperature can be used to control the etch rate.

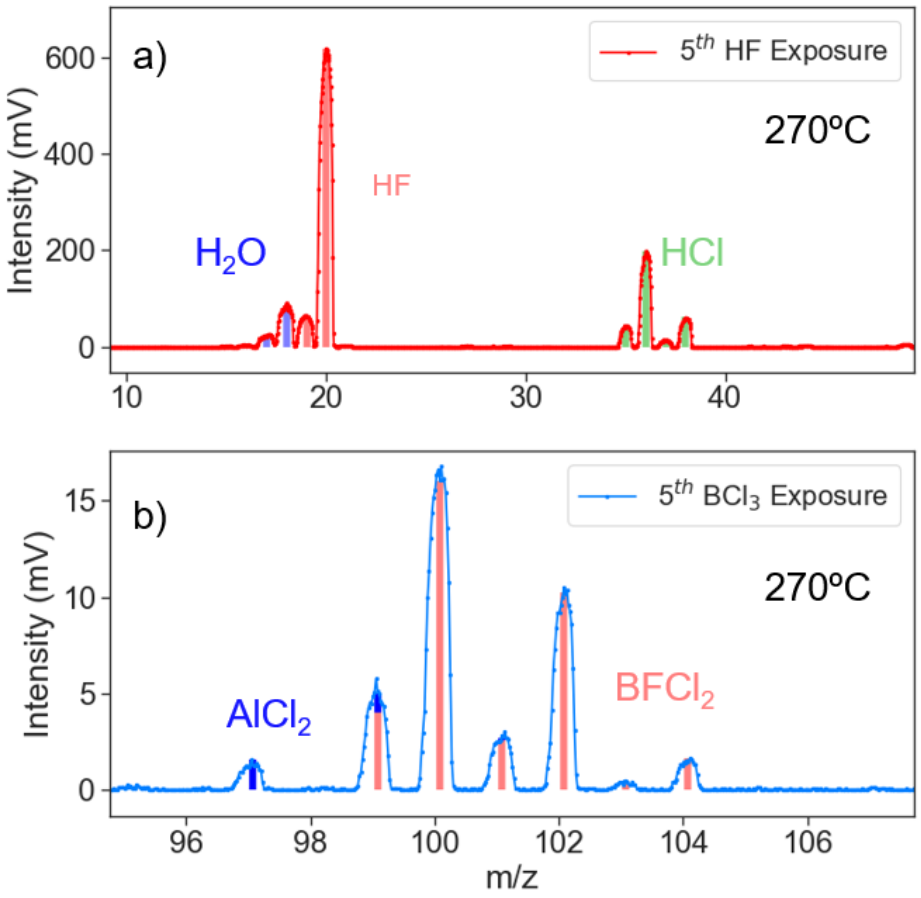

Figure 5-8: Mass spectrum during the 5th cycle of HF and BCl_3 cycling on aluminum oxide powder.

To study the ligand exchange reaction, mass spectrometry was used.[107] The substrate was aluminum oxide powder and alternating exposures of HF and BCl_3 was pulsed through the powder bed. This simulates the chemical exposure of the aluminum oxide films used during IR and SE experiments. The mass spectrum after an HF exposure is shown in Figure 5-8a with the

spectrum after a BCl_3 exposure shown in Figure 5-8b. After the HF exposure a few peaks are seen including H_2O, HF, and HCl. HF is expected in the spectrum as it's the precursor used in this step. H_2O seen is likely due to the fluorination reaction: $Al_2O_{3(s)} + 6HF_{(g)} \rightarrow 2AlF_{3(s)} + 3H_2O_{(g)}$. This fluorination reaction has the byproduct of H_2O and is the main reaction responsible for creating aluminum fluoride on the aluminum oxide substrate.[20] HCl seen in the spectrum likely means that there is residual chlorine left on the surface after the BCl_3 exposure. This is consistent with chlorine contamination after aluminum nitride etching with XeF_2 and BCl_3 as seen in Chapter 4. Interestingly, there was no boron containing species seen in the HF exposures. This would have been evidence that there was a conversion of the surface aluminum oxide to boron oxide which would be spontaneously etched during the HF exposure. This reaction is the focus of Chapter 6. This would suggest that the reaction goes by fluorination and then ligand-exchange.

Figure 5-8b shows the mass range from 95-107 amu. In this region there is the $AlCl_2^+$ and $BFCl_2^+$ peaks. $AlCl_2^+$ is the most intense peak of the $AlCl_3$ parent. This makes the $AlCl_2^+$ a good region to see if there is any $AlCl_3$ being volatilized during cycling of HF and BCl_3. $AlCl_3$ is the expected by product of both the conversion reaction: $Al_2O_{3(s)} + 2BCl_{3(g)} \rightarrow B_2O_{3(s)} + 2AlCl_{3(g)}$ and the ligand exchange reaction: $AlF_{3(s)} + 3BCl_{3(g)} \rightarrow AlCl_{3(g)} + 3BFCl_{2(g)}$. The proposed by product is $BFCl_2$ which would be a single ligand exchange with the aluminum fluoride surface. The ligand exchange reaction may lead to the boron byproducts of BF_3 and BF_2Cl which would be a complete and double ligand exchange reactions with aluminum fluoride. This was seen in the reaction of BCl_3 with AlF_3 studied in Chapter 4. The BCl_3 exposure shows peaks representative of $AlCl_2^+$ and $BFCl_2^+$. This would align with the expected

byproduct of $AlCl_3$ and the ligand exchange product of $BFCl_2$. Small peaks that were consistent with BF_2Cl were also seen in the spectrum. The intensity of the $AlCl_3$ peak is also seen but with a weak signal. During BCl_3 exposures, there was also small amounts of $B_3O_3Cl_3$ present with an intensity of ~0.5 mV.

5.5 Conclusions

Thermal ALE was done on aluminum oxide using HF and BCl_3. The reaction was monitored by in-situ FTIR and showed a reaction mechanism close to fluorination and ligand-exchange. Initial exposures of BCl_3 on aluminum oxide were consistent with a conversion of aluminum oxide to boron oxide. This reaction seemed to be more prominent on the initial aluminum oxide film and not as prominent on subsequent cycles. This boron oxide was then removed by an HF exposure. During the HF exposure the underlying aluminum oxide was also fluorinated. Difference spectra showed evidence of fluorination and ligand-exchange reactions happening once the surface was etched. Ellipsometry measurements showed there was linear etching of the aluminum oxide film. The ALE etching rate was also controllable by changing the substrate temperature. Etch rates of aluminum oxide with HF and BCl_3 0.03, 0.31, 0.65, and 0.92 Å/cycle. Quadrupole mass spectrometry showed the expected aluminum product in $AlCl_3$ and the ligand-exchange product $BFCl_2$.

Understanding Spontaneous Etching of B_2O_3 by HF Gas Using Infrared Spectroscopy, Mass Spectrometry and Density Functional Theory

Austin M. Cano,[1] Suresh Natarajan,[2-3] Jonathan L. Partridge,[1] Simon Elliot,[4] and Steven M. George[1]

1Department of Chemistry, University of Colorado, Boulder CO, 80309, USA.

[2]University College Cork, Tyndall National Institute, Lee Maltings, Dyke Parade, Cork, T12 R5CP, Ireland.

[3]Department of Electrical Engineering and Automation, Aalto University, Espoo 02150, Finland

[4]Schrödinger Inc., 120 West 45th Street, 17th Floor, New York, NY 10036-4041, USA.

6.1 Abstract

The spontaneous etching of B_2O_3 (boron oxide) by HF (hydrogen fluoride) gas is important during thermal atomic layer etching (ALE) after BCl_3 converts the surface of various metal oxides to a B_2O_3 layer. In this study, the chemical vapor etching (CVE) of B_2O_3 by HF was monitored experimentally using Fourier transform infrared spectroscopy (FTIR) and quadrupole mass spectrometry (QMS). The spontaneous etching of B_2O_3 by HF gas was also analyzed using density functional theory (DFT). The B_2O_3 films were grown using B_2O_3 atomic layer deposition (ALD) with BCl_3 and H_2O as the reactants at 40°C. FTIR spectroscopy then observed the CVE of B_2O_3 by HF at 150 °C. The B_2O_3 etching was monitored by the loss of absorbance for the B-O stretching vibration in B_2O_3 films. The FTIR spectroscopy studies also observed B-F stretching vibrations from BF_x species on the B_2O_3 surface after HF exposures. In

addition, QMS analysis was able to identify the etch products during the spontaneous etching of B_2O_3 by HF gas at 150 °C. The QMS studies observed the main volatile etch products as BF_3, $BF_2(OH)$ and H_2O. Secondary volatile etch products were also detected including $B_3O_3F_3$ and other boroxine ring compounds. The DFT predictions were consistent with the spontaneous etching of B_2O_3 by HF gas. DFT confirmed that CVE was likely because the energetics of the spontaneous etching reaction $B_2O_3(s) + 6HF(g) \rightarrow 2BF_3(g) + 3H_2O(g)$ were more favorable than the self-limiting reaction $B_2O_3(s) + 6HF(g) \rightarrow BF_3(s) + 3H_2O(g)$. The spontaneous etching of B_2O_3 was predicted at temperatures above -163°C for a HF reactant pressure of 0.2 Torr and BF_3 and H_2O product pressure of 0.01 Torr.

6.2 Introduction

Etching has been important to fabricate images and patterns for many centuries.[2] Dry etching has been particularly important in semiconductor processing.[5] The fabrication of three-dimensional device structures uses successive steps of deposition and etching in the presence of masks to control the areas for deposition and etching. Much of the previous dry etching has been performed using reactive radical and ionic species from plasmas.[4] Some dry etching has also utilized plasmaless thermal chemistry.[109-110] A prominent application of dry etching using only thermal chemistry is micromachining and feature release during MEMS processing.[111-113]

Compared with plasma etching, there are not many examples of dry thermal etching. The main demonstrations of dry thermal etching involve the formation of volatile halides using various halogenation reactants. For example, the dry thermal etching of silicon can occur spontaneously using XeF_2, F_2 or ClF_3 as the reactants.[109-110, 114] Many metals can also be etched by exposure to halogenation reactants. Tungsten and niobium can undergo dry thermal etching

by XeF_2.[112-113, 115-116] Other metals, such as copper and aluminum, can also be spontaneously etched by Cl_2.[116-117]

Many metal oxides can also be spontaneously etched using ligand addition or halogenation reactions. Copper oxide, iron oxide and other metal oxides can be spontaneously etched by exposure to ligands that can coordinate to the metal and produce volatile products.[118-120] The dry etching of SiO_2 can also occur with HF in the presence of H_2O vapor at H_2O pressures sufficient to form a H_2O multilayer on the SiO_2 surface.[121] Other examples of dry thermal spontaneous etching involve a variety of ligand-exchange reactions between metal fluorides and precursors that transfer ligands to the metal fluoride that volatilize the metal fluoride.[10, 13, 22, 86-87, 101]

Spontaneous etching is also involved in thermal atomic layer etching (ALE).[10, 85] Two sequential reactions typically define thermal ALE. One reaction modifies the surface layer of the material and the second reaction leads to the volatile release of this modified surface layer.[10] For example, the surface modification of metal oxides and metal nitrides during thermal ALE can be performed using fluorination to form a metal fluoride.[10, 56] The metal fluoride can then be volatilized using ligand-exchange reactions. Other mechanisms for thermal ALE can employ oxidation reactions to change the oxidation state of the metal or conversion reactions to convert the initial metal oxide to a different metal oxide that has an etching pathway.[10, 17, 61] If at least one reaction in the thermal ALE reaction sequence is self-limiting, the other reactions in the sequence may involve spontaneous etching.

Spontaneous etching in thermal ALE reaction sequences has been identified in several systems. WO_3 ALE using BCl_3 and HF as the reactants involves conversion of WO_3 to B_2O_3 and

then the spontaneous etching of B_2O_3 by HF.[61] TiN ALE using O_3 and HF as the reactants is defined by the oxidation of TiN to TiO_2 and then the spontaneous etching of TiO_2 by HF.[57] In addition, Al_2O_3 ALE using HF and TMA as the reactants proceeds by the fluorination of Al_2O_3 to AlF_3 and then the spontaneous etching of AlF_3 by TMA.[57, 86] In these examples, the conversion, oxidation or fluorination reactions are self-limiting, and then the removal of the modified surface layer occurs by spontaneous etching.

The reaction of HF with metal oxides plays a pivotal role in many thermal ALE systems.[68, 122] HF can either remove the initial material or the modified surface layer as a volatile fluoride by chemical vapor etching (CVE). Alternatively, HF can fluorinate the initial material leading to the formation of a stable self-limiting (SL) metal fluoride layer. The CVE or SL pathways are determined by the energetics and volatility of the reaction products. Having a better knowledge of HF reactions with metals and metal oxides will help improve the understanding of spontaneous etching and its role in thermal ALE.

In this paper, the spontaneous etching of B_2O_3 by HF gas is examined using FTIR spectroscopy, quadrupole mass spectrometry (QMS) and density functional theory (DFT). The FTIR analysis confirms the spontaneous etching of B_2O_3 by HF gas and reveals the species remaining on the B_2O_3 surface after HF etching. The QMS measurements identify the volatile etch products that leave the B_2O_3 surface during etching. The DFT investigations examine the energetics of the CVE and SL reactions between B_2O_3 and HF gas and predict the expected etch products versus temperature and reactant and product pressures.

6.3 Experiment and Methods

6.3.1 FTIR Spectroscopy

The Fourier transform infrared (FTIR) spectroscopy studies of B_2O_3 etching by HF were performed in a reactor reported previously.[92] Prior to B_2O_3 etching, the boron oxide was deposited using B_2O_3 ALD using sequential exposures of BCl_3 (≥99.9% trace metals basis, Sigma-Aldrich) and deionized (DI) H_2O at 35 °C.[61] The BCl_3 reaction was a 2 s exposure in viscous flow, followed by 90 s purge. The FTIR scan was then recorded for 60 s. The water reaction consisted of a 1 s exposure, followed by a 60 s purge. The FTIR scan was then again recorded for 60 s.

The B_2O_3 ALD film was deposited on silicon nanoparticles (>98 % US Research Nanomaterials). The silicon nanoparticles had a diameter of ~30-50 nm. The use of silicon nanoparticles ensures a good signal-to-noise ratio when using transmission FTIR spectroscopy to identify surface species.[17] The silicon nanoparticles were pressed into a tungsten grid. The FTIR spectroscopy was then conducted by passing the IR light through the tungsten grid.[82] The tungsten grid was ~1.7 x 3.0 cm, 50 microns thick with 100 grid lines per inch. The tungsten grid was resistively heated with a DC power supply (6268B, 12 V/40 A, HP). The power supply was controlled by a PID temperature controller (Love Controls 16B, Dwyer Instruments). To monitor the temperature, a type K thermocouple was connected to the tungsten grid with a nonconductive epoxy (Cermabond 571).

The B_2O_3 spontaneous etching experiments were performed using HF-pyridine (70 wt% HF, Sigma-Aldrich) as the HF source. Each HF exposure was a 2 s static exposure of HF at 200 mTorr followed by a 90 second purge. Subsequently, the FTIR scan was recorded for 60 s.

Longer purges than necessary were used to eliminate the possibility of HF contact with the KBr windows during the FTIR scan.

6.3.2 Quadrupole Mass Spectroscopy (QMS)

The QMS investigations employed a new reactor that has been described earlier.[101] This reactor is different than a previous reactor that employed static exposures and then sampled the gas phase products using a pulsed valve.[101] The new reactor studies volatile etch products produced by flowing reactant gases through powder samples. The volatile etch products and background gas were expanded through an aperture to form a molecular beam. The beam of background gas and volatile etch products were then passed through a skimmer and entered a differentially pumped region for QMS analysis.

The skimmer aperture diameter was 1.4 mm and the skimmer was positioned 41 mm from the sample aperture.[101] The volatile etch products were observed using a high sensitivity, high mass quadrupole mass spectrometer (Extrel, MAX-QMS Flange Mounted System). Each spectrum monitored mass intensities from 2 amu to 300 amu and was recorded in 1 s. An average of 100 scans were collected during HF exposures to help eliminate noise. Electron-impact ionization of gas-phase etching products was achieved with a circular thoriated iridium filament in the ionization volume inside the ionizer housing. An electron ionization energy of 70 eV was used for these experiments.

HF was first introduced into a reservoir at a pressure of 9 Torr to have a consistent HF partial pressure during the reaction. HF was leaked into the flowing N_2 background gas. The HF pressure in the sample holder containing the B_2O_3 powder was 5.2 Torr. The background N_2 pressure was 2.8 Torr. B_2O_3 nano powder was purchased from US Research Nanomaterials

(99.9%, 165 nm diameter) and added to a sample holder. The mass of the B_2O_3 nano powder was recorded before and after the etching experiments. The mass of the B_2O_3 nano powder before the spontaneous etching was 50.5 mg.

6.3.3 Density Functional Theory (DFT)

The computational approach is similar to the approach employed in previous studies.[68, 122] In these earlier investigations, the energetics and thermochemistry of self-limiting (SL) and chemical vapor etching (CVE) reactions are compared to reveal their competition. In the CVE reaction, the HF precursor gas molecules etch B_2O_3 to form gaseous products. In the SL reaction, the HF precursor gas molecules interact and passivate the material surface by forming a non-volatile fluoride layer.

This computational study considered the following CVE and SL reactions:

CVE1: $B_2O_{3(b)} + 6\ HF_{(g)} \rightarrow 2BF_{3(g)} + 3H_2O_{(g)}$ (1)

CVE2: $4B_2O_{3(b)} + 14HF_{(g)} \rightarrow 5H_2O_{(g)} + BF_{3(g)} + 4B(OH)F_{2(g)} + B_3O_3F_{3(g)}$ (2)

SL: $2B_2O_3^{*} + 12H_{(g)} \rightarrow 4\ BF_3^{*} + 6H_2O_{(g)}$ (3)

In these reactions, b indicates bulk, g refers to gas and the asterisks designate surface species.

This computational approach revealed that there is a “minimum thermodynamic barrier” that must be overcome to allow etching from the passivated surface. Based on the value of this “minimum thermodynamic barrier” and the respective energies of the CVE and SL reactions, the HF precursor gas pulse can be in one of the four following states: purely self-limiting, preferred

self-limiting, preferred etching and purely etching. These states are discussed in detail in previous studies.[122]

All the DFT calculations performed in this study were based on spin polarized generalized gradient approximation using the Perdew-Burke-Ernzerhof (PBE) exchange-correlation (XC) functional[123] as implemented in the Vienna ab initio simulation package (VASP).[124] In this approach, the valence electrons are treated explicitly by expanding their wave functions in a plane wave basis up to an energy cutoff of 400 eV, whereas the core electrons are treated by projector augmented waves.[125-126]

The enthalpy and entropy contributions of the bulk and surface geometries are computed with the help of the Phonopy code,[127] which requires accurate interatomic force constants obtained from density functional perturbation theory (DFPT) calculations in VASP. The total electronic energies of gas phase molecules, BF_3 and H_2O, are computed in VASP by placing their molecular geometry in a large periodic box of dimensions 15.0 x 15.5 x 16.0 and relaxing them. However, the enthalpy and entropy contributions of the gas phase molecules are obtained from the free enthalpy (freeh) code of Turbomole suite[10] using the PBE XC functional and triple zeta basis set (def-TZVPP).

To model the bulk B_2O_3 geometry, a trigonal lattice geometry is employed from the materials project database.[128] The geometry is reoptimized simultaneously for the ionic positions, cell shape and cell volume with an increased plane wave energy cutoff of 550 eV and a Monkhorst-Pack K-point mesh of 4 x 4 x 2. The converged lattice parameters are found to be a=b=4.4027 Å, c=8.8174 Å, $\alpha=\beta=90°$, $\gamma=120°$ as shown in Figure 6-1a

A 9.4 Å thick slab of trigonal B_2O_3 sliced along the (1 0 1) surface plane with 15 Å of vacuum separating the periodic images along the surface normal was then chosen to represent the surface model in the self-limiting reaction. This surface slab model consists of 3 layers of 6 B_2O_3 units ($B_{36}O_{54}$) as shown in Figure 6-1b. To model the fluorinated surface, 6 surface O atoms are removed as H_2O and 12 F atoms are introduced such that the F atoms bind to surface boron atoms as shown in Figure 6-1c. The geometry was optimized to obtain the ground state electronic energy. Only the top most layer of these surfaces was considered for the DFPT calculations.

The reaction free energy (ΔG) discussed in this paper is computed as:

$$\Delta G = \Delta H - T\Delta S + RTln(Q), \text{ where} \quad (4)$$

$$\Delta H = \Delta E + \Delta ZPE + \Delta W(T) \quad (5)$$

$$Q = \prod p^{\mu}_{products} / \prod p^{\mu}_{reactants} \quad (6)$$

In these equations, ΔH and ΔS are the enthalpy and entropy change, respectively. ΔH is computed as the sum of the electronic reaction energy (ΔE), zero point energy change (ΔZPE) and a temperature dependent contribution ($W(T)$). R is the gas constant, Q is the reaction quotient which allows for changes in reactant and product pressures, and μ is the stoichiometric coefficient of the respective reactant and product species.

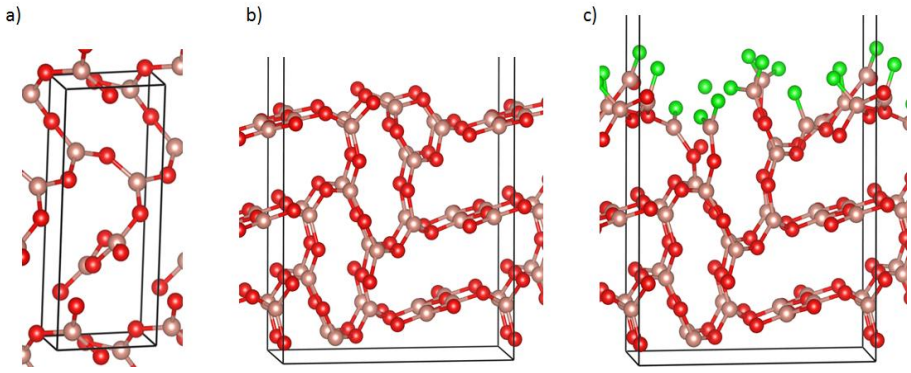

Figure 6-1: (a) Reoptimized trigonal lattice geometry for B_2O_3 bulk; (b) Bare (1 0 1) surface of trigonal B_2O_3. (c) Fluorinated B_2O_3 surface from Figure 1b after removing 6 surface O atoms.

6.4 Results and Discussion

6.4.1 FTIR Spectroscopy

The etching of B_2O_3 films was studied using transmission FTIR spectroscopy. To study the etching of B_2O_3 films, B_2O_3 was first deposited on silicon nanoparticles. FTIR studies of B_2O_3 ALD are shown in Figure 6-2. B_2O_3 ALD was performed with BCl_3 and H_2O as the reactants at a low deposition temperature of ~40°C.[61] The overall reaction is $2BCl_3 + 3H_2O \rightarrow B_2O_3 + 6HCl$. The BCl_3 exposure was conducted for 1 s at 500 mTorr. The H_2O exposure was conducted for 1 s at 80 mTorr. B_2O_3 ALD with BCl_3 and H_2O is similar to B_2O_3 ALD using BBr_3 and H_2O.[129] Earlier studies of B_2O_3 ALD films using BCl_3 and H_2O have also been performed and found to have the correct B_2O_3 stoichiometry by XPS.[61]

Figure 6-2 shows the FTIR spectra referenced to the original silicon nanoparticle substrate. After the first BCl_3 and H_2O cycle, absorbance gains are measured at 1450 cm^{-1} and 1315 cm^{-1} and a smaller absorbance loss is observed at 1250 cm^{-1}. These absorbance features

can be identified as a gain of B-O stretching vibrations and a small loss of Si-O-Si vibrations, respectively.[35, 108, 130-131] The loss of absorbance for Si-O-Si vibrations likely results from boron being slightly soluble in silicon.[132] Three main vibrational modes grow at 1450 cm^{-1}, 1315 cm^{-1} and 730 cm^{-1} with increasing number of B_2O_3 ALD cycles up to 15 cycles. These vibrational features are assigned to different boron-oxygen stretching modes and ring stretching modes in boric acid and borate.[108, 130-131, 133]

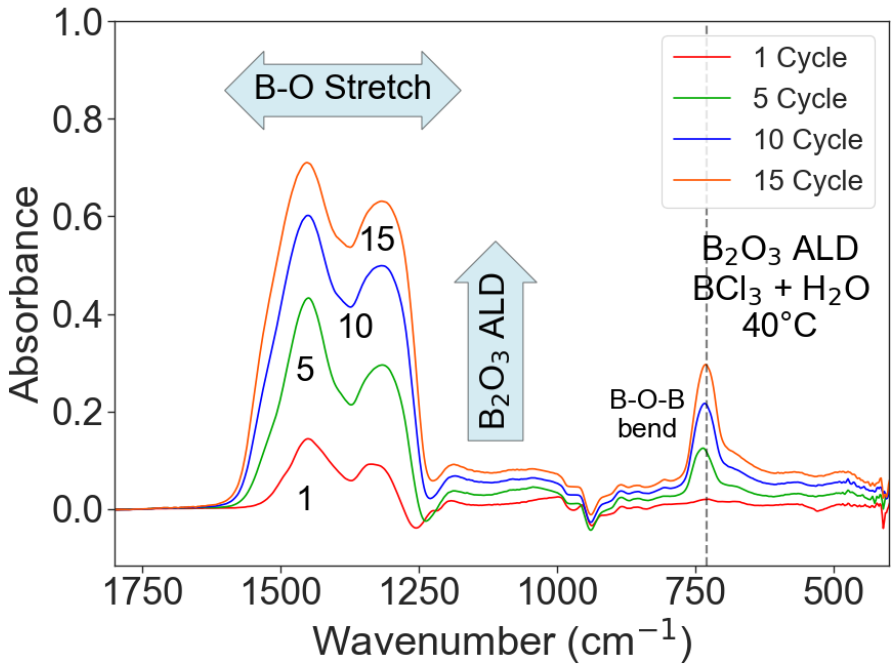

Figure 6-2: Infrared absorbance spectra from 400 – 1800 cm^{-1} during B_2O_3 ALD using BCl_3 and H_2O as reactants after 1, 5, 10 and 15 B_2O_3 ALD cycles at 40ºC.

Difference spectra recorded during the 13th BCl_3 and H_2O exposures during B_2O_3 ALD are displayed in Figure 6-3. These difference spectra are consistent with the sequential AB reactions during B_2O_3 ALD as:

(A) $BOH^* + BCl_3(g) \rightarrow BOBCl_2^* + HCl(g)$ (7)

(B) $BCl^* + H_2O(g) \rightarrow BOH^* + HCl(g)$ (8)

In these equations, the astericks indicate the surface species.

In Figure 6-3a, positive vibrational absorbance peaks are observed at 1530, 1362, 1273, and 950 cm^{-1} after the BCl_3 exposure. The absorbance peaks at 1530, 1362 cm^{-1} and 1273 cm^{-1} are attributed to different boron oxide vibrations such as ring-stretching boroxol vibrations and B-O stretching vibrations.[108, 130-131, 133] The absorbance peak at 950 cm^{-1} is attributed to B-Cl surface vibrations left on the surface after the BCl_3 exposure.[134] There are also B-Cl vibrations found between 1300 and 1500 cm^{-1} that are largely obscured by the absorbance from B-O vibrational modes.[134] Negative vibrational absorbance peaks are also observed at 750, and 500 cm^{-1} after the BCl_3 exposure. These peaks are assigned to BO_2 bending vibrations.[130-131, 133] A small loss at 1450 cm^{-1} is assigned to B-OH and is likely lost resulting from BCl_3 reaction with BOH species.[108]

Positive vibrational absorbance peaks are also observed in Figure 6-3a at 1440 cm^{-1}, 730 cm^{-1} and 530 cm^{-1} after the H_2O exposure. These vibrational features result from the reaction of H_2O with BCl surface species. These are likely B-OH stretching vibrations and the bending modes of BO_2.[131] In addition, there are also negative absorbance peaks at 1530, 1362, 1273, and 950 cm^{-1} after the H_2O exposure. These negative absorbance peaks after the H_2O exposure mirror the reverse of the positive absorbance peaks monitored after the BCl_3 exposure. There is also a negative vibrational absorbance peak at 1250 cm^{-1} after the H_2O exposure. This negative absorbance peak is attributed to the removal of B-Cl surface species.[134]

Figure 6-3b shows the change in the O-H vibrations after H_2O and BCl_3 exposures. After H_2O exposures there is an increase at 3700 cm^{-1} that is consistent with isolated O-H groups in boric acid like films.[135] There is also a very broad peak at 3600-3000 cm^{-1} that is attributed to hydrogen-bonded BOH species on the surface.[135] The positive absorbance features observed after the H_2O exposure are then almost exactly reversed when the BOH species are removed from the surface by reaction with the BCl_3 exposure.

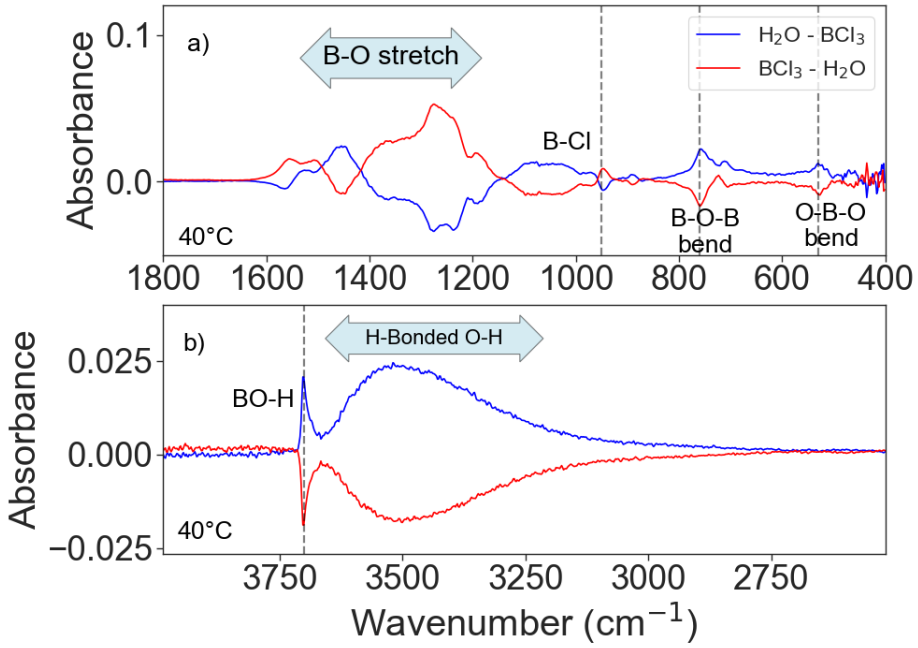

Figure 6-3: Infrared difference spectra recorded after BCl_3 and H_2O exposures during 14th B_2O_3 ALD cycle at 40ºC. (a) Difference spectra between 400 - 1800 cm^{-1}. (b) Difference spectra between 400 - 2500 cm^{-1}.

The spontaneous etching of B_2O_3 by HF gas was then examined using the B_2O_3 ALD films. FTIR spectra were recorded after each 2 s static exposure of HF at 200 mTorr at 150 °C. These FTIR spectra were referenced to the initial B_2O_3 ALD film on the silicon nanoparticles.

The progressive FTIR spectra versus number of HF exposures for 9 HF exposures on B_2O_3 are shown in Figure 6-4. Each consecutive HF exposure removes a fraction of the absorbance from the B_2O_3 ALD film. This absorbance loss corresponds with CVE of the B_2O_3 film. The vibrational modes at 1450 cm^{-1}, 1315 cm^{-1} and 730 cm^{-1} are attributed to B-O vibrations as discussed earlier during the growth of the B_2O_3 ALD films.[108, 130-131, 133] The first HF exposure in Figure 6-4 only removes a small fraction of the B_2O_3 film. Perhaps the first HF exposure is required to fluorinate the surface and condition the B_2O_3 film. The largest absorbance losses are observed during the second, third and fourth HF exposures in Figure 6-4. The absorbance losses are reduced during the subsequent HF exposures. By the eighth HF exposure, the B_2O_3 film has been completely removed by the CVE reaction.

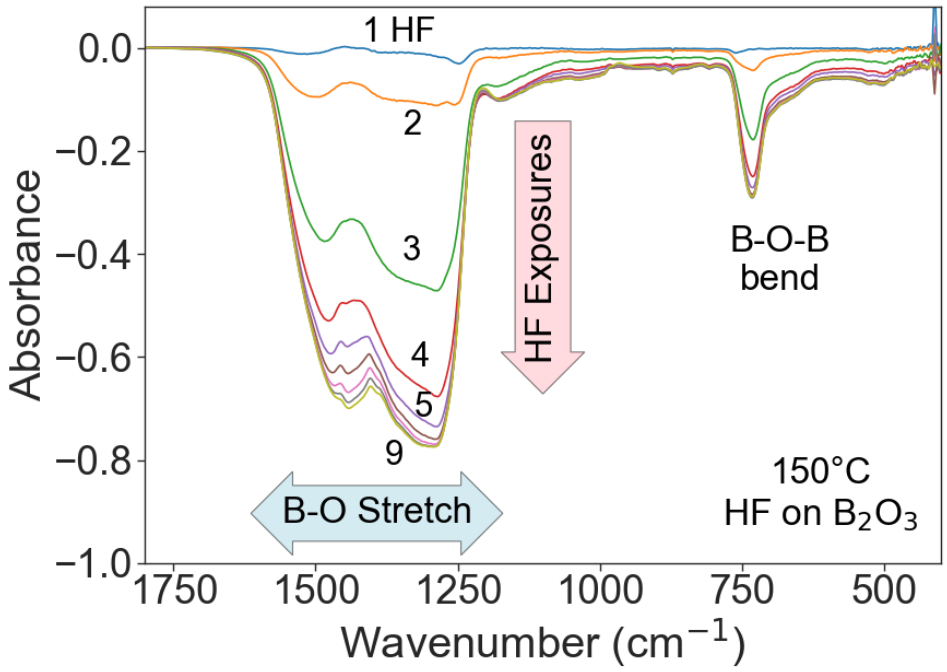

Figure 6-4: Infrared difference spectra between 400 -1800 cm^{-1} recorded after consecutive HF exposures on B_2O_3 ALD film at 150ºC using original B_2O_3 ALD film as reference. Original B_2O_3 ALD film is nearly completely removed after 5 HF exposures.

The spontaneous etching of B_2O_3 by HF at 150°C is consistent with earlier results for B_2O_3 etching by HF at 207°C observed by spectroscopic ellipsometry studies.[61] These previous studies were conducted to confirm that HF could spontaneously remove B_2O_3 films after using BCl_3 to convert the surface of WO_3 to B_2O_3 layers. The conversion of WO_3 to B_2O_3 was an important step in the thermal ALE of WO_3 using BCl_3 and HF and also the thermal ALE of W using O_2/O_3, BCl_3 and HF.[61] The earlier study etched B_2O_3 ALD film grown using BCl_3 and H_2O as the reactants and then etched the B_2O_3 ALD films using HF exposures of 100 mTorr s. Each HF exposure removed ≈1.8 Å of B_2O_3 at 207°C.[61] In contrast, approximately 5 HF

exposures were required to remove the B_2O_3 ALD film in Figure 6-4 where each HF exposure was 400 mTorr s. Based on a B_2O_3 ALD growth rate of ≈ 1 Å/cycle using BCl_3 and H_2O,[61] the etch rate in Figure 6-4 for the B_2O_3 film grown using 15 B_2O_3 ALD cycles is ≈3 Å/HF exposure. There is reasonable agreement Figure 6-5 shows difference spectra from 3350-3850 cm^{-1} referenced to the initial B_2O_3 film during HF exposures on B_2O_3. There is an absorbance increase at 3740 cm^{-1}, an absorbance loss at 3700 cm^{-1}, and another broad absorbance loss from 3400-3700 cm^{-1}. The positive absorbance feature at 3740 cm^{-1} is attributed to H-F stretching vibrations from adsorbed HF on the surface.[136-137] Figure 6-4 shows that most of the B_2O_3 film has been etched after the 4th HF exposure. Before the 4th HF exposure, HF was presumably consumed by the B_2O_3 etching reaction.

Figure 6-5 shows that the peak at 3700 cm^{-1} decreases and is constant after the first HF exposure. This peak is attributed to terminal BO-H vibrational stretching vibrations.[135] Terminal BOH species were also present during B_2O_3 ALD after the H_2O exposure as shown in Figure 6-3b. These terminal BOH species are consumed by the first HF exposure. The broad absorbance loss from 3400-3700 cm^{-1} is also assigned to the loss of hydrogen-bonded BOH groups on the B_2O_3 film.[135] However, these hydrogen-bonded BOH groups are not removed until after the 4th HF exposures. The removal of these hydrogen-bonded BOH groups coincides with the growth of absorbance assigned to HF on the B_2O_3 surface.

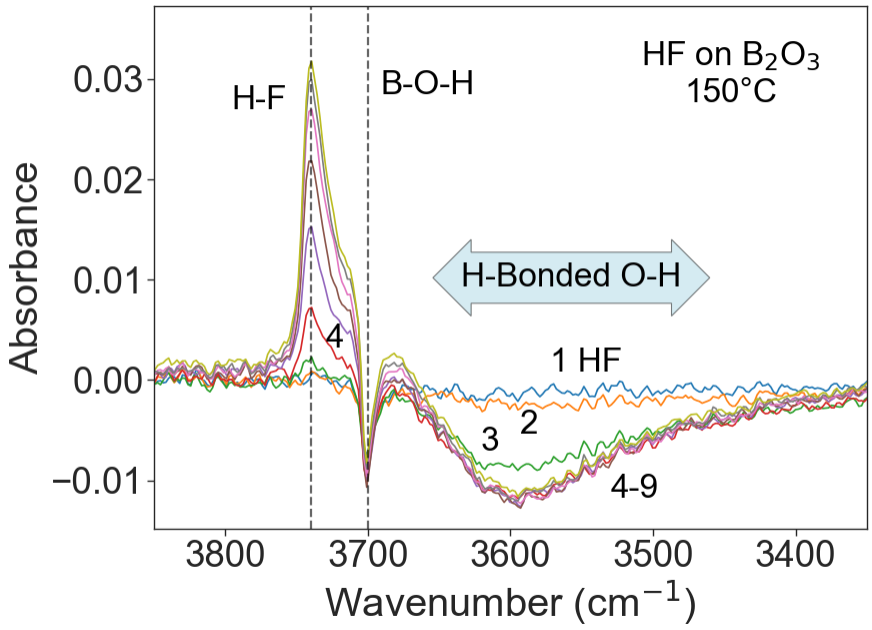

Figure 6-5: Infrared difference spectra between 3300 - 3900 cm^{-1} recorded after consecutive HF exposures on B_2O_3 ALD film at 150ºC using original B_2O_3 ALD film as reference.

Figure 6-6 shows the change in the FTIR spectra during the 1st HF exposure and during the last (9th) HF exposure. The 1st HF exposure is referenced to the initial B_2O_3 ALD film and the 9th HF exposure is referenced to the 8th HF exposure to understand the change of each individual HF exposure. For comparison, this difference spectrum is contrasted with the inverted absorbance for the B_2O_3 ALD film over the same frequency range. The FTIR difference spectra after the first HF exposure shows apparent absorbance loss peaks at 1242 cm^{-1} and 1517 cm^{-1}. These two apparent absorbance loss peaks result from removal of B-O vibrations together with an absorbance gain at 1440 cm^{-1} resulting from another vibrational feature. The absorbance gain

at 1440 cm^{-1} does not appear as a positive absorbance peak because this absorbance gain occurs concurrently with a larger absorbance loss resulting from the B_2O_3 spontaneous etching.

If the first HF exposure was only removing B_2O_3, then the FTIR difference spectra after the first HF exposure and the absorbance from the B_2O_3 ALD film should be similar in Figure 6-6. The discrepancy between the first HF exposure and ninth HF exposure can be explained by the growth of absorbance from B-F vibrational modes of BF_x surface species at 1440 cm^{-1}.[138-141] This new positive absorbance partially offsets the absorbance loss resulting from B_2O_3 etching. Subsequent HF exposures lead to the loss of more B_2O_3 and the comparison between the FTIR difference spectra and the absorbance from the B_2O_3 ALD film is more similar as shown in Figure 6-4. This behavior is expected if the BF_x surface species stay constant during subsequent HF exposures while the B-O absorbance losses continue to increase with more HF exposures.

Further confirmation for the assignment of B-F stretching vibrations from BF_x surface species centered at ~1430 cm^{-1} is derived from the evolution of the difference spectra with each HF exposure. The FTIR difference spectra after the 9th exposure shows only an absorbance loss centered at 1430 cm^{-1}. This absorbance loss is again consistent with the B-F stretching vibrations from BF_3 surface species.[138-141] In this case, nearly all the B_2O_3 has been etched away. The 9th HF exposure then removes the last of the B-F surface species.

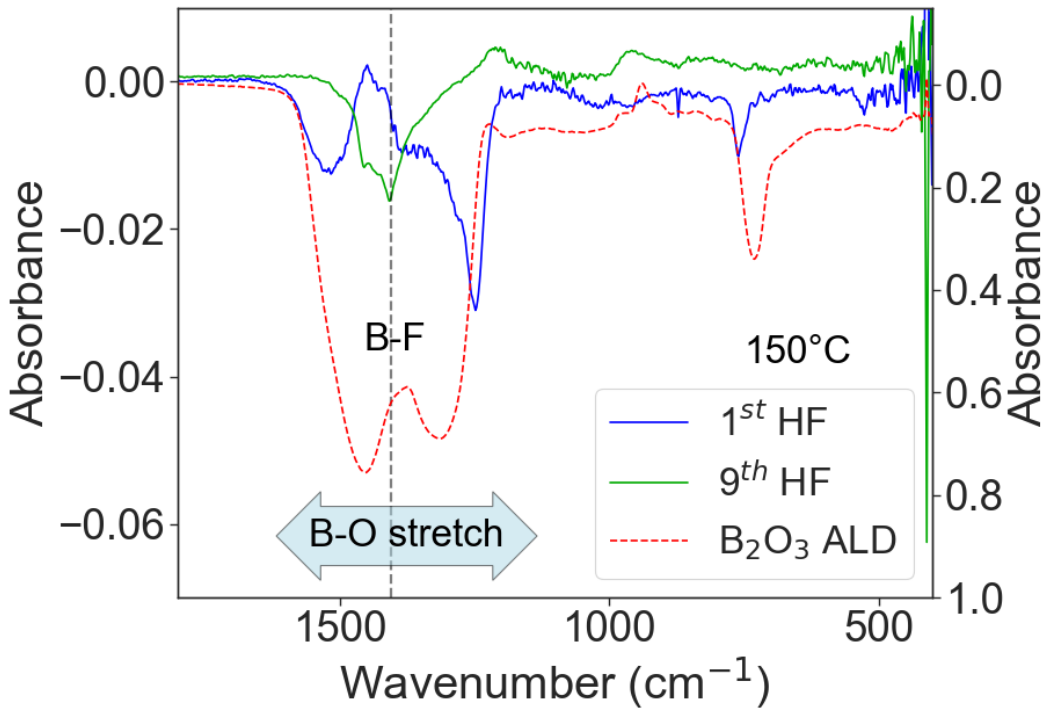

Figure 6-6: Infrared difference spectra showing absorbance after 1st HF exposure referenced to the initial B_2O_3 ALD film and 9th HF exposure referenced to the absorbance after the 8th HF exposure. Inverted absorbance for original B_2O_3 ALD film is also shown for comparison

The B_2O_3 also was easily etched by HF at lower temperatures than 150°C. Figure 6-7 shows the etching of B_2O_3 during HF exposures at a lower temperature of 40°C. This temperature was the lowest temperature examined in this study. The B-O vibrational feature at 1200-1600 cm^{-1} decreases in intensity during the first and second HF exposures. The absorbance loss is faster than the absorbance loss observed for B_2O_3 etching at 150°C shown in Figure 6-4. However, the B_2O_3 etching rate was not quantified versus temperature.

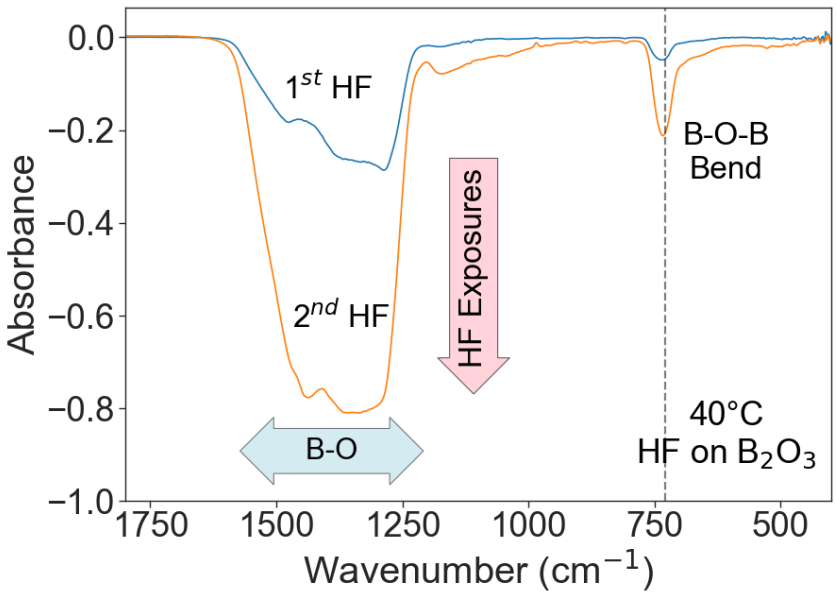

Figure 6-7: Infrared difference spectra between 400 -1800 cm^{-1} recorded after consecutive HF exposures on B_2O_3 ALD film at 40ºC using original B_2O_3 ALD film as reference. Original B_2O_3 ALD film is nearly completely removed after 2 HF exposures.

6.4.2 QMS

Quadrupole mass spectrometry (QMS) was used to identify the volatile etch products during the spontaneous etching of B_2O_3 by HF. The QMS observed that the main volatile etch products were BF_3, $BF_2(OH)$ and H_2O. Figure 6-8 shows a portion of the mass spectrum from 40-70 amu during the 1st and 5th HF exposures at 150ºC on B_2O_3. In this spectral range, the main peaks are assigned to BF_3 and $BF_2(OH)$. The largest masses at m/z =68 and 67 amu are assigned to the BF_3^+ molecular ion. The shapes of the clusters are determined by the 80:20 isotopic ratio between ^{11}B and ^{10}B. The ratio of the signal intensities at m/z = 68 and 67 is consistent with the natural isotopic abundance of boron.

The largest mass intensity is observed for a fragment of BF_3^+ corresponding to BF_2^+ at m/z =49 amu for ^{11}B. There is also a signal at m/z = 48 amu based on the isotopic abundance of ^{10}B. This peak also has the correct signal intensity relative to the signal at m/z = 49 amu. In addition, there are other peaks at m/z = 66 and 65 amu that are assigned to $BF_2(OH)$. The fragmentation of $BF_2(OH)^+$ also produces a signal for $BF(OH)^+$ at m/z= 47 and 46 amu. The species $BF_2(OH)^+$ and $BF(OH)^+$ have been observed and characterized previously by reacting BF_3 with $B(OH)_3$ at room temperature.[142] This etching of B_2O_3 can also be confirmed by the mass loss of B_2O_3 powder. The initial mass of the B_2O_3 powder was 50.5 mg. After multiple HF exposures, the B_2O_3 powder mass was reduced to 24.8 mg.

Figure 6-8a shows that there are more $BF_2(OH)$ species observed during the 1st HF exposure compared with the 5th HF exposure displayed in Figure 6-8b. In particular, the signals for $BF_2(OH)^+$ and $BF(OH)^+$ both drop dramatically versus the signal for BF_2^+ when comparing Figure 6-8a and Figure 6-8b. The initial B_2O_3 powder was loaded into the chamber from ambient air. The air exposure likely hydrated the B_2O_3 surface to form a boric-acid like surface. This surface yields more OH species during HF etching.

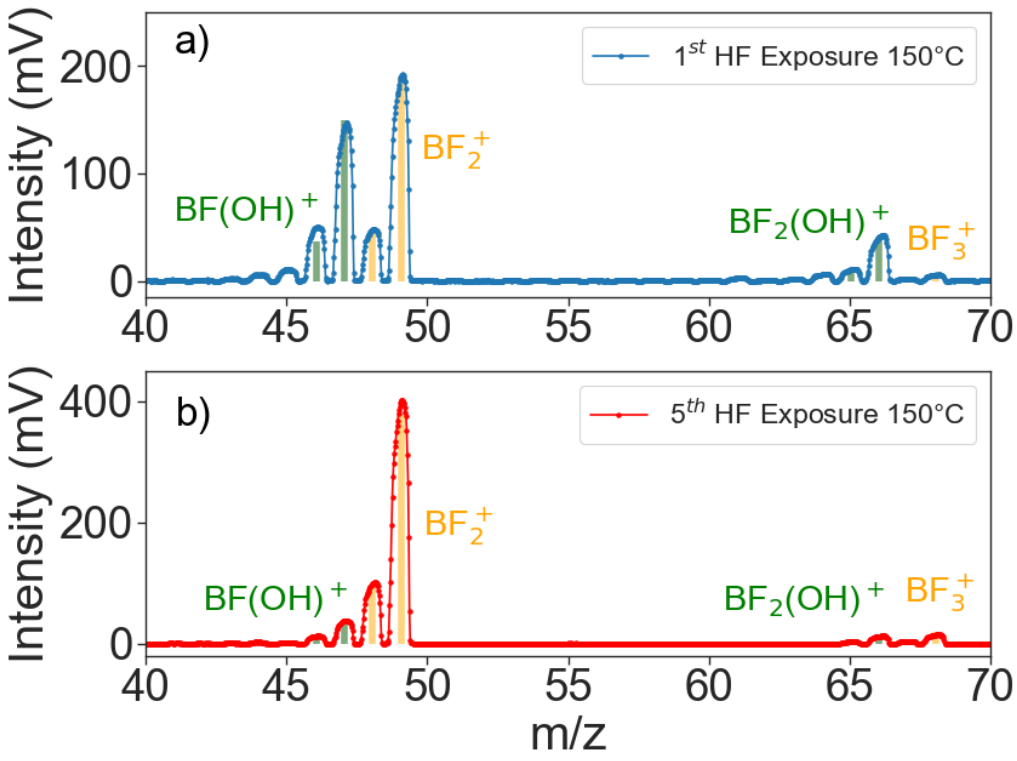

Figure 6-8: Mass spectrum of products monitored in range from m/z = 40-75 amu during spontaneous etching of B_2O_3 by HF at 150ºC during the (a) 1st HF exposure and (b) 5th HF exposure. Observed products are BF_3 and $B(OH)F_2$.

Figure 6-9 shows the mass signals at higher mass from m/z =75 - 140 amu. This portion of the mass spectrum corresponds to boroxine ring compounds. The existence of gas phase $B_3O_3F_3$ boroxine rings has been previously reported and characterized using mass spectrometry.[143] Figure 6-9 reveals that clusters of mass peaks are observed around m/z= 136 amu, 118 amu, 92 amu, and 79 amu. The peaks located from m/z = 131-140 amu are shown on an expanded scale in Figure 6-10. These peaks are attributed to the parent $B_3O_3F_3$, $B_3O_3F_2OH$

and $B_3O_3F(OH)_2$ boroxine rings. The identity of these peaks is confirmed by the predictions for their masses based on the isotopic abundance of ^{11}B and ^{10}B shown in Figure 6-10.

The next grouping of peaks is observed around m/z =118 amu in Figure 6-9. These peaks are consistent with $B_3O_3F_2^+$ and $B_3O_3F(OH)^+$. These peaks are assigned to fragments of the $B_3O_3F_3$ and $B_3O_3F_2OH$ boroxine ring compounds. The grouping of peaks around m/z =92 amu are also fragments of the parent boroxine rings and are attributed to $B_2OF_2OH^+$ and $B_2OF_3^+$. Likewise, the grouping of peaks around m/z = 79 amu are assigned to the fragments $B_2F_3^+$ and $B_2F_2(OH)^+$. The signals for the boroxine rings with hydroxyl groups in Figure 6-9 are much larger during the 1st HF exposure compared with the 5th HF exposure. The larger hydroxyl content during the 1st HF exposure is again attributed to the initial boric acid-like surface of the B_2O_3 powders. This hydrated B_2O_3 surface is removed by the 5th HF exposure.

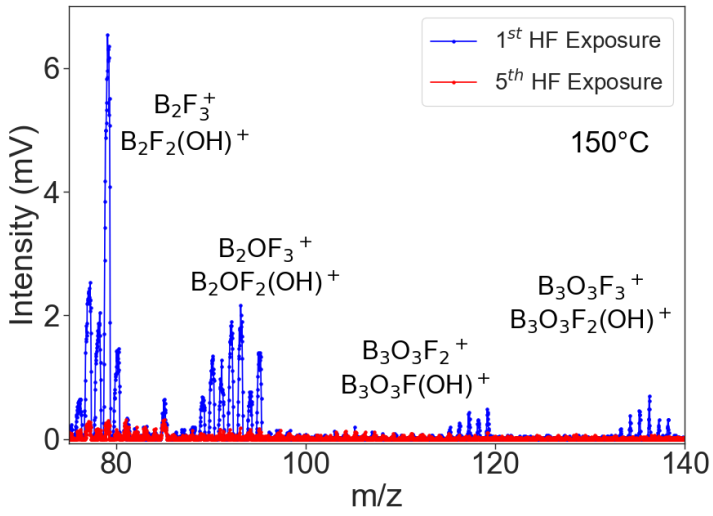

Figure 6-9: Mass spectrum of products monitored in range from m/z = 70-140 amu during spontaneous etching of B_2O_3 by HF at 150ºC during the (a) 1st HF exposure and (b) 5th HF exposure. Observed products are $B_3O_3F_3$, $B_3O_3F_2OH$ and $B_3O_3F(OH)_2$ boroxine rings.

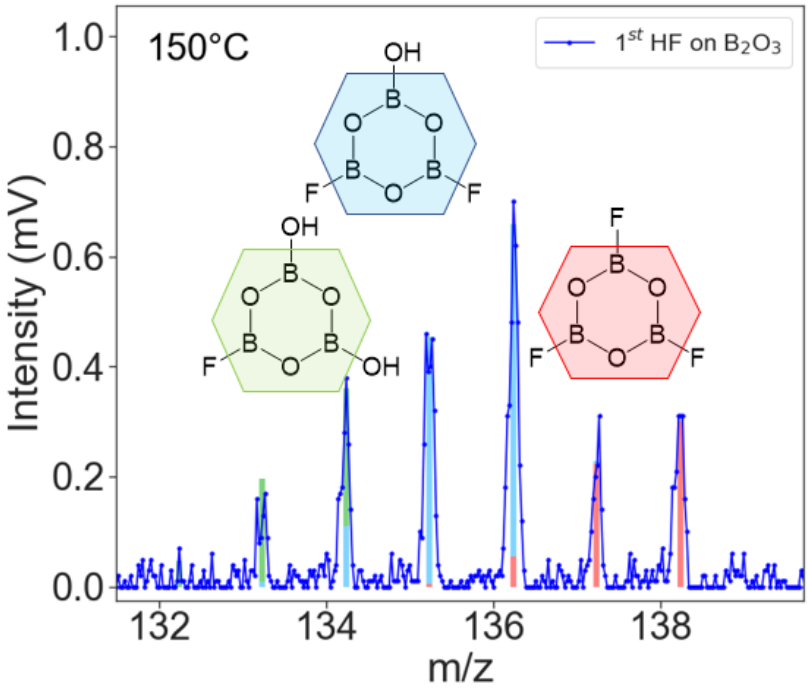

Figure 6-10: Mass spectrum of products monitored in range from m/z = 131 - 140 amu during spontaneous etching of B_2O_3 by HF at 150ºC. Parent peaks of $B_3O_3F_3$, $B_3O_3F_2(OH)$, $B_3O_3F(OH)_2$ boroxine rings are observed during 1st HF exposure.

The etch products evolve versus number of HF exposures on the B_2O_3 powder. Figure 6-11 shows the evolution of the main volatile etch products during the first five HF exposures on the B_2O_3 powder. Figure 6-11a shows the mass intensities for BF_2^+ and $BF(OH)^+$. These species are the highest mass intensities corresponding to the BF_3 and $BF_2(OH)$ volatile etch products. Figure 6-11b displays the mass intensities for H_2O^+ corresponding to the same first five HF exposures.

A comparison between the signals for BF_2^+ and $BF(OH)^+$ for the first five HF exposures in Figure 6-11a reveals that the intensity for the $BF(OH)^+$ drops significantly with HF exposures.

In contrast, the intensity for H_2O^+ in Figure 6-11b is very constant for the 2nd-5th HF exposures. The decrease in the signal for $BF(OH)^+$ is consistent with the HF etching through the initial surface of the hydrated B_2O_3 powder. After removing this boric acid-like surface of the B_2O_3 powder, the HF exposure yields primarily BF_3 as the volatile etch product.

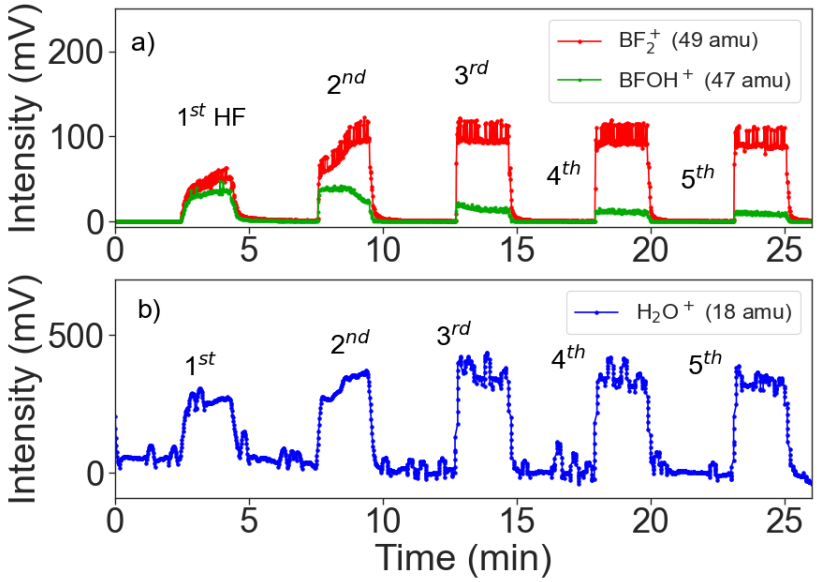

Figure 6-11: Mass traces of (a) BF_2^+ at m/z =47 amu and BFOH+ at m/z = 49 amu and (b) H_2O^+ at m/z = 18 amu versus time during the first 5 HF exposures on B_2O_3 powder.

6.4.3 DFT

DFT was used to determine the reaction energies and "minimum thermodynamic barriers" to etch. The CVE1 reaction is $B_2O_3 + 6\ HF(g) \rightarrow 2\ BF_3(g) + 3\ H_2O(g)$. This reaction needs 6 HF molecules to etch a unit bulk of B_2O_3 and form 2 BF_3 and 3 H_2O gas phase molecules. The BF_3 and H_2O reaction products are consistent with the results from the QMS studies. The CVE1 reaction is determined to be exoergic with a reaction energy of -1.6 eV. The

SL reaction is also exoergic with a reaction energy of -0.8 eV. This reaction energy is less exoergic than the CVE1 reaction by 0.8 eV. Consequently, the spontaneous etch reaction is more favorable than the self-limiting reaction and there is a negative "minimum thermodynamic barrier" for spontaneous etching.

The CVE2 reaction is 4 B_2O_3 + 14 HF(g) → 5 H_2O(g) + BF_3(g) + 4 $B(OH)F_2$(g) + $B_3O_3F_3$(g). This reaction was considered to study the formation of the $B(OH)F_2$ and $B_3O_3F_3$ reaction products. These reaction products were also identified by the QMS investigations. The CVE2 reaction is exoergic with a reaction energy of -1.1 eV. However, this reaction energy of -1.1 eV is only -0.27 eV per each B_2O_3 unit. Therefore, this reaction energy is much less than the reaction energy of -1.8 eV per each B_2O_3 unit for the CVE1 reaction. The "minimum thermodynamic barrier" to etch B_2O_3 and form these $B(OH)F_2$ and $B_3O_3F_3$ products is also negative. The much larger reaction energy for the CVE1 reaction is consistent with the QMS observation of primarily BF_3 etch products after removing the hydrated layer on the B_2O_3 powder.

Figure 6-12 displays the free energy profiles (FEPs) of CVE1, CVE2 and SL reactions in the temperature range of 0 – 1000 K at a constant HF reactant pressure of 0.2 Torr and a product pressure of 0.01 Torr. The SL reaction is exergonic at 0 K and increases in free energy with temperature. The SL reaction crosses the zero line at 110 K and becomes endergonic at higher temperatures. In comparison, the free energies of CVE1 and CVE2 reactions are exergonic at 0 K. The free energies of CVE1 and CVE2 reactions decrease with temperature albeit with a small negative slope. The FEP of the CVE1 reaction has a comparatively slightly larger negative slope than the FEP of the CVE2 reaction. The CVE1 and CVE2 reactions never cross the zero line.

The region up to 110 K in Figure 6-12 is labelled as “preferred etching” since the CVE reactions are more favorable than the SL reaction and both CVE and SL reactions are exergonic in this temperature range. The region at temperatures greater than 110 K in Figure 6-12 is labelled as “purely etching”. In this temperature zone, the SL reaction is endergonic. The stable surface B-F bonds at T<110 K (163ºC) are not favorable in the presence of a continuous supply of HF gas at T> 110 K. The experimental FTIR and QMS observations of spontaneous etching of B_2O_3 by HF exposure at 150°C (423 K) are in the “purely etching” region and consistent with these computational results. The FTIR results of spontaneous B_2O_3 etching by HF at 40°C and the earlier spectroscopic ellipsometry measurements of spontaneous B_2O_3 etching by HF at 207°C are also in agreement with these theoretical predictions.[61]

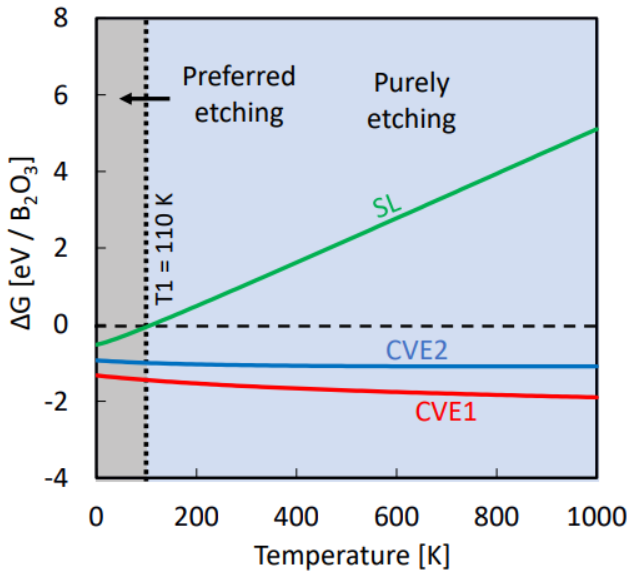

Figure 6-12: ΔG free energy profiles of CVE1, CVE2 and SL reactions versus temperature at a constant HF reactant pressure of 0.2 Torr and a product pressure of 0.01 Torr. SL reaction becomes endergonic at 110 K.

The FEPs of the CVE1 and SL reactions were then examined at different reactant HF pressure from 0.01 Torr to 2.0 Torr at a constant product pressure of 0.01 Torr in the temperature range of 0 – 1000 K. The resulting free energy changes for CVE1 and SL reactions and the difference between the reactions, CVE1-SL, are shown in Figure 6-13. The CVE1 reaction is favorable at all pressures and temperatures. An increase in the reactant HF pressure decreases the slope of the CVE1 FEP and makes the reaction slightly more favorable at any given temperature. In agreement with Figure 6-12, the SL reaction displays a zero crossing at approximately 110K (163ºC) at all pressures. The plot of CVE1 – SL does not show significant change versus reactant pressure. The spontaneous etching reaction becomes only slightly more favorable relative to the self-limiting reaction as the reactant pressure increases.

The FEPs of the CVE1 and SL reactions were also explored at different product pressures of 0.01 Torr, 0.2 Torr, 1 Torr and 2 Torr for reactant HF pressures from 0.01 Torr to 2.0 Torr in the temperature range of 0 – 1000 K. The resulting free energy changes for CVE1 and SL reactions and the difference between the reactions, CVE1-SL, are displayed in Figure 6-14. The free energy of CVE1 increases with increase in the product pressure and the reaction becomes unfavorable at high temperatures. The free energy of SL also increases with product pressure. The temperature for the zero crossing for the SL FEP also decreases, although a very small change, at higher product pressures. The unfavorability of both the CVE1 and SL reactions at high product pressure leads to the white region for CVE1-SL in Figure 6-14. In this region at high product pressure, the reaction may reverse and lead to B_2O_3 deposition by $BF_3 + H_2O \rightarrow B_2O_3 + HF$.

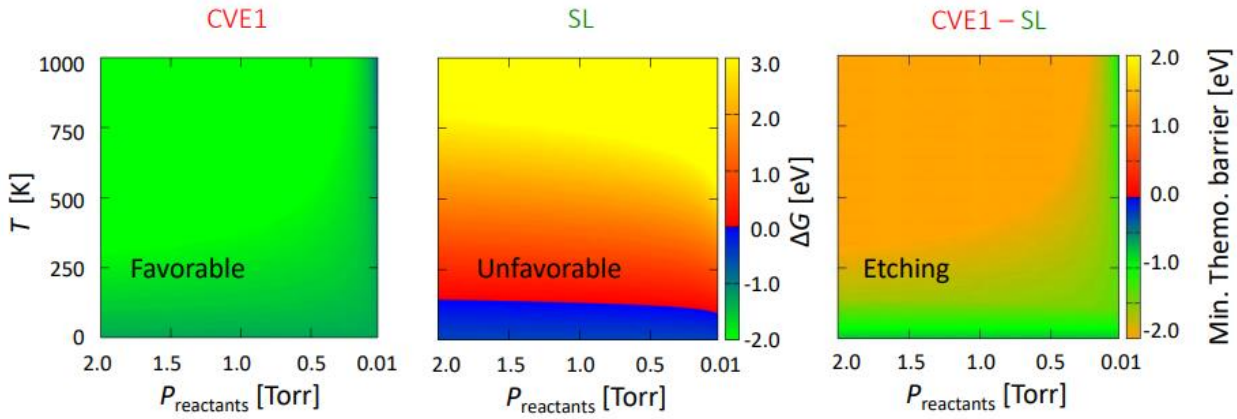

Figure 6-13: 2D heat maps of ΔG free energies of CVE1 and SL reactions and corresponding "minimum barrier" to etch given by CVE1 – SL at different reactant HF pressures from 0.01 Torr to 2.0 Torr at a constant product pressure of 0.01 Torr.

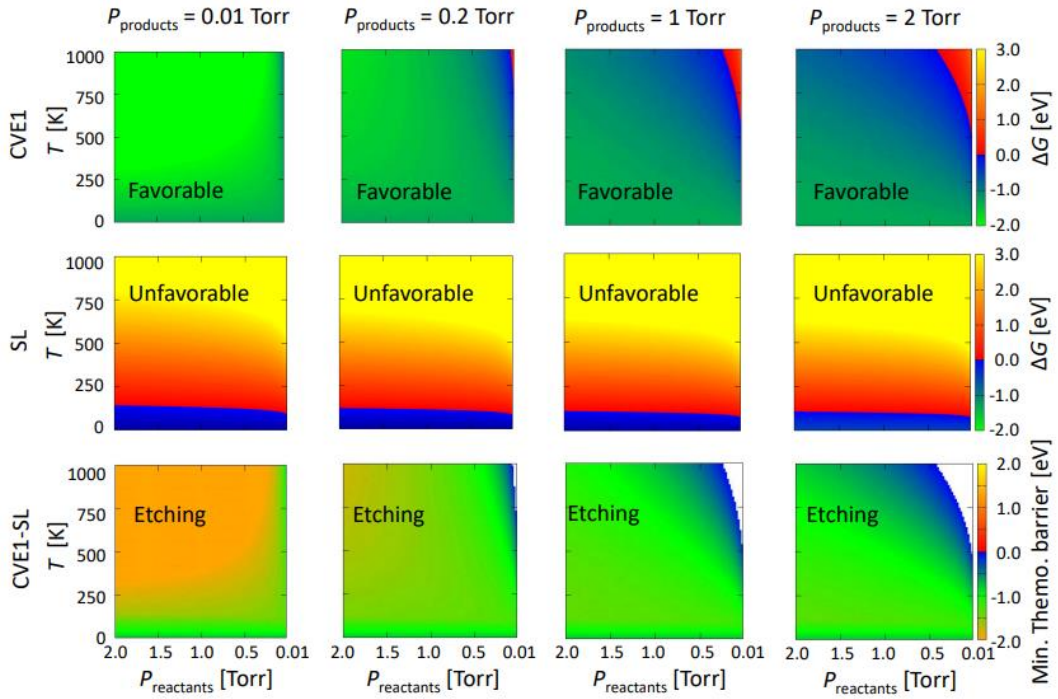

Figure 6-14: 2D heat maps of ΔG free energies of CVE1 and SL reactions and corresponding "minimum barrier" to etch given by CVE1 - SL with respect to change in HF pressure from 0.01 Torr to 2.0 Torr for product pressures of 0.01 Torr, 0.2 Torr, 1 Torr and 2 Torr.

6.5 Conclusions

The reaction of HF on B_2O_3 was investigated using FTIR to demonstrate the spontaneous etching and understand the surface chemistry, QMS to identify the etch products and DFT to predict and understand the CVE reaction. Using B_2O_3 films grown using B_2O_3 ALD, FTIR spectroscopy observed the CVE of B_2O_3 by HF at 150 °C. The B_2O_3 etching was monitored by the loss of absorbance for the B-O stretching vibration in B_2O_3 at 1200-1600 cm^{-1}. The FTIR spectroscopy studies also observed B-F stretching vibrations from BF_x species on the B_2O_3 surface at 1440 cm^{-1} after HF exposures.

The volatile etch products during the spontaneous etching of B_2O_3 by HF at 150 °C were identified by QMS studies. The main etch products were BF_3, $B(OH)F_2$ and H_2O. During the initial HF exposures on B_2O_3 powders that had been exposed to air, boroxine ring etch product were also detected including $B_3O_3F_3$, $B_3O_3F_2(OH)$ and $B_3O_3F(OH)_2$. After etching through the initial hydrated B_2O_3 powder, the later HF exposures produced mostly BF_3 and H_2O and fewer $B(OH)F_2$ and boroxine rings products.

DFT studies investigated the energetics of the CVE reactions and SL reactions. The spontaneous etching of B_2O_3 was predicted at temperatures above -163°C for a HF reactant pressure of 0.2 Torr and BF_3 and H_2O combined product pressure of 0.01 Torr. The DFT calculations confirmed that BF_3 is the preferred etch product. In addition, the energetics of the reaction was affected slightly by the pressure of the reactant and products.

Prediction and Validation of Process Window for Atomic Layer Etching: HF Exposure on TiO_2

Suresh Kondati Natarajan,*[1,2] Austin M. Cano,[3] Jonathan L. Partridge,[3] Steven M. George,[3] and Simon D. Elliott[4]

[1]University College Cork, Tyndall National Institute, Lee Maltings, Dyke Parade, Cork, T12 R5CP, Ireland.
[2]Department of Electrical Engineering and Automation, Aalto University, Espoo 02150, Finland
[3]Department of Chemistry, University of Colorado, Boulder, Colorado 80309, USA
[4]Schrödinger Inc., 120 West 45th Street, 17th Floor, New York, NY 10036-4041, USA.

7.1 Abstract

A combined computational and experimental study is employed to understand the competition between self-limiting (SL) and chemical vapor etch (CVE) reactions to design an atomic layer etch (ALE) process. The pulses in an ALE process have to be self-limiting, i.e. the reactions should reach saturation after sufficient pulse time. By comparing the reaction free energies of corresponding SL and CVE reactions using density functional theory (DFT), the temperature and pressure conditions can be predicted that favor the SL or CVE reactions. The etching of TiO_2 when exposed to HF gas is utilized as a test case. Simulations reveal that when TiO_2 is exposed to reactant HF at a pressure of 0.2 Torr, the SL reaction removing H_2O at 0.01 Torr and fluorinating the surface is preferred up to 87ºC (360 K). At higher temperatures, continuous removal of TiO_2 by CVE occurs according to the reaction $TiO_2 + HF \rightarrow TiF_4 + H_2O$ subject to kinetic activation barriers. Experimental results from in situ Fourier Transform Infrared (FTIR) spectroscopy and quadrupole mass spectrometry (QMS) are compared with the

theoretical predictions. In good agreement with theory, the FTIR spectroscopy studies revealed an onset of spontaneous etching (CVE) at temperatures around 80-90ºC. In addition, the QMS analysis observed TiF_4 and H_2O as the etch products, further validating the calculations. The calculations also predicted that an increase in the reactant gas pressure would enhance etching at high temperatures. The low computational cost of this theoretical approach allows for rapid screening of etch reagents and prediction of the temperature/pressure windows where the reactions will be in the SL or CVE regimes.

7.2 Introduction

Materials may be processed reliably and uniformly with atomic level control by exploiting self-limiting gas-surface reactions. For instance, atomic layer deposition (ALD) is a process in which a precise fraction of a monolayer of material is deposited in each cycle of gas pulses via a sequence of self-limiting (SL) surface reactions.[9, 144] ALD has become an indispensable step in the fabrication of modern semiconductor devices.[9, 144-147] Alternatively, materials may be deposited faster, but with less control, by means of chemical vapor deposition (CVD), which is a spontaneous and continuous process.

A sequence of SL reactions is also the basis for atomic layer etch (ALE) process.[1, 22] ALE is expanding in scope to become a key enabling technology for the fabrication of next generation semiconductor devices.[1, 8, 22, 89, 148-149] In some cases, combining ALD and ALE will be advantageous for the production of ultra-smooth thin films only on selected substrates.[150] This area-selectivity could reduce the number of lithographic steps and allow further size reduction in semiconductor devices.[22, 150] The challenge is to identify SL chemistries, or more

precisely, to identify reagents and reaction conditions for the desired SL reaction. This paper presents a combined experimental and computational approach for meeting this challenge.

In the ALE concept, the target material surface is first chemically modified by exposure to a pulse of a suitable gas reactant that self-limits after forming a non-volatile surface layer.[1, 10, 88] The modified layer is then volatilized by the action of the second reactant pulse. Plasma ALE employs directional (*i.e.* anisotropic) high energy ion bombardment in the second pulse to remove the modified surface layer .[1, 151] Thermal isotropic ALE processes have also recently been introduced where the modified layer is removed by chemical reaction with another gas phase reactant.[10, 85, 88] The second reactant may then remove the entire modified layer in a continuous, unlimited way, but self-limits upon reaching the unmodified material underneath.

Modification of the surface by the first reactant is the subject of this study. The first reactant is introduced into the etch chamber as a gas and adsorbs onto the substrate material by binding with the surface atoms. A volatile by-product may be produced at this stage. If some fragment of the reactant passivates the surface and causes the surface to become inert towards further reactant adsorption, then this is an SL reaction, as required for ALE.[152] On the other hand, the adsorbate could continue to react with the substrate by diffusing into and reacting with sub-surface layers. This process would result in continual formation of volatile by-products that desorb and regenerate active sites on the surface. This spontaneous reaction would be a CVE process.[152]

Thermochemical calculations of model reactions have been performed by researchers investigating ALD and ALE processes.[13, 88-89, 153-157] One popular approach is to model the reactions using thermochemical tables from databases such as NIST-JANAF[157] with the help of software packages such as the HSC Chemistry.[120] Alternatively, reactions can be modelled from

first principles using density functional theory (DFT) calculations. Such calculations have been used to investigate ALD mechanism in detail[8, 145, 153] and recently also to study thermal ALE with HF.[152, 158] One advantage of using first principles calculations is that any specific phase of a solid system or any gas phase molecule of interest, however exotic, can be modelled explicitly by ab initio methods. In addition, databases typically include only bulk materials, and so the calculated thermochemistry is valid only for bulk deposition or etching, and not for the surface reactions.

Applying DFT to a slab model is the standard computational procedure for investigating material surfaces, including their interaction with gas phase molecules.[152, 158] This approach can be used to model the SL reaction. By comparing the free energy profiles (FEPs) of CVE and SL reactions using the 'Natarajan-Elliott' analysis,[152] the nature of a reactant pulse can be understood. From this analysis, a 'minimum thermodynamic barrier' to etch is computed, which is the difference between the corresponding reaction free energies of the CVE and SL reactions. Four distinct reaction states are identified based on the value of this 'minimum thermodynamic barrier'. These states are purely self-limiting, preferred self-limiting, preferred etching and purely etching. A detailed description of this analysis methodology is given elsewhere.[152]

TiO_2 has significant applications in a variety of technological fields.[159] For example, TiO_2 is an important photocatalyst and has been explored for the production of hydrogen and self-cleaning surfaces.[160] TiO_2 is also a key material in semiconductor devices such as metal-oxide resistive random access memory (RRAM).[161] Thin films of TiO_2 are also used in mirror coatings, orthopedic implants and pharmacological applications. A great number of examples are available where thin films of TiO_2 have been deposited using the ALD approach.[162-163]

HF has been used as the fluorinating agent in the thermal ALE of several metal oxides such as Al_2O_3, HfO_2 and ZrO_2.[88-89, 154] However, HF was found to be unsuitable in the thermal ALE of TiO_2 where the Ti atoms are in an oxidation state of +4.[164] TiO_2 is spontaneously etched by HF at temperatures greater than 200°C, probably forming gaseous TiF_4 and H_2O.[164] However, when WF_6 was used as the fluorination reactant at lower temperatures below 170□C, TiO_2 ALE was possible using WF_6 and BCl_3 without the spontaneous etching of TiO_2.[13] Therefore, HF exposure on TiO_2 presents an excellent test case for investigating the competition between self-limiting and spontaneous etch reactions.

The purpose of this paper is to demonstrate and validate a combined computational and experimental approach for the design of new ALE processes. The main design steps are: (1) choosing reactant molecules for each pulse, (2) optimizing the process conditions in terms of temperature and reactant gas pressure, and (3) identifying and treating the exhaust gases. In a purely experimental approach, each design choice is evaluated by trial and error in the laboratory. This is a time intensive process that limits the number of options that can be considered. On the other hand, purely computer-based design can consider a much larger range of molecules. However, the computational model may not be able to include all the variables. A closely-coupled combination of computations to narrow down the design choices and experiments to optimize the reaction conditions may provide the best strategy.

7.3 Methods Section

7.3.1 Computational Methods

The calculations described in this paper were performed within spin-polarized density functional theory (DFT) using the Vienna ab initio simulation package (VASP, version 5.3).[124] The calculations were based on the generalized gradient approximation (GGA) using the Perdew-Burke-Ernzerhof (PBE) exchange-correlation functional.[123] The core electrons were described by projector augmented wave potentials [125, 165] and the valence electrons were treated explicitly using plane wave basis sets up to 400 eV of energy.

The reaction free energies reported in this paper were computed as follows

$$\Delta G = G\mathrm{p} - G\mathrm{r} + RT\ln(Q)$$

with

$$G\mathrm{p|r} = H\mathrm{p|r} - TS\mathrm{p|r}$$

$$H\mathrm{p|r} = E\mathrm{p|r} + \mathrm{ZPEp|r} + W(T)\mathrm{p|r}$$

$$Q = \prod p^{\mu}\mathrm{p} / \prod p^{\mu}\mathrm{r}$$

Here, ΔG is the reaction free energy, p and r in the subscript refer to products and reactants, respectively, H is enthalpy which includes the DFT electronic energy E, zero point energy (ZPE) and S is entropy. The temperature dependent enthalpy $W(T)$ is simply RT for molecules and $\Sigma_{q^{\nu}} \hbar\omega(q^{\nu})/(\exp(\hbar\omega(q^{\nu})/k_B T) - 1)$ for solids where q is wave vector, ν is phonon mode index and ω is the phonon frequency. Q is the reaction quotient, which measures the relative amounts of product and reactant molecules participating in the reaction, and μ is the stoichiometric coefficient for the reaction. The quantities H and S for bulk and surface models

were obtained from phonon frequencies using the Phonopy code.[127] Accurate force constants are a prerequisite for this, and they were obtained from density functional perturbation theory (DFPT) calculations in VASP using a strict energy convergence threshold of 1.0e^{-8} eV.

'Natarajan-Elliott' analysis was used to study the competition between CVE and SL reactions via free energies from a modest number of DFT calculations. In this analysis, each precursor pulse is designated to one of four possible cases depending on the reaction free energies of the SL and CVE reactions (negative free energy means the reaction is favorable):[152]

(a) preferred self-limiting (ΔG_{CVE}, $\Delta G_{SL} < 0$; $\Delta G_{SL} < \Delta G_{CVE}$),

(b) purely self-limiting ($\Delta G_{CVE} > 0$; $\Delta G_{SL} < 0$; $\Delta G_{SL} < \Delta G_{CVE}$),

(c) preferred etching (ΔG_{CVE}, $\Delta G_{SL} < 0$; $\Delta G_{SL} > \Delta G_{CVE}$) and

(d) purely etching ($\Delta G_{CVE} < 0$; $\Delta G_{SL} > 0$; $\Delta G_{SL} > \Delta G_{CVE}$).

The bulk and surface models of TiO_2 in the calculations were constructed from its rutile crystalline phase (space group $P4_2/mnm$) and the corresponding relaxed geometries are shown in . The bulk unit cell consists of two TiO_2 units, which is optimized by simultaneously relaxing the ionic positions, cell volume and cell shape with a higher energy cutoff of 550 eV and a Monkhorst-Pack K-point mesh of 6×6×6. For the surface calculations, a 15 Å thick slab of (2×4) supercell of the rutile-TiO_2 (1 1 0) surface ($Ti_{80}O_{160}$) with a surface area of 1.57 nm^2 and relaxed surface energy of 0.91 J/m^2 was constructed with 15 Å of vacuum separating the periodic images in the surface normal direction. This supercell consists of 5 $Ti_{16}O_{32}$ layers, out of which the bottom two layers were kept fixed. A K-point mesh of 2×2×1 was used for geometry optimization of this slab. The (1 1 0) surface of rutile TiO_2 was chosen for this study as its signature was found from the XRD spectra of TiO_2 ALD at high film thicknesses.[166]

To model the surface geometries resulting from the SL reactions, preserving stoichiometry, 8 surface O atoms are removed from the bare surface of TiO_2 (1 1 0) followed by the adsorption of 16 F atoms as shown in Figure 2a. Moreover, to represent the reduced TiO_{2-x} surface, just 12 F atoms are adsorbed following the removal of 8 O atoms as shown in Figure 2b. For these surface slabs, *H* and *S* are computed by considering only the top layer of surface atoms highlighted in the figures.

Gas phase calculations of the reagent molecules and by-products were performed using VASP with a large periodic box of dimensions 15.0 Å × 16.0 Å × 15.5 Å with an energy cutoff of 400 eV. However, for convenience, *H* and *S* values for these gas phase molecules are obtained from the free program of the Turbomole suite[167] at a constant pressure of 1 atm. All gas phase calculations in Turbomole were performed with the PBE functional and a valence triple zeta basis set (def-TZVPP).

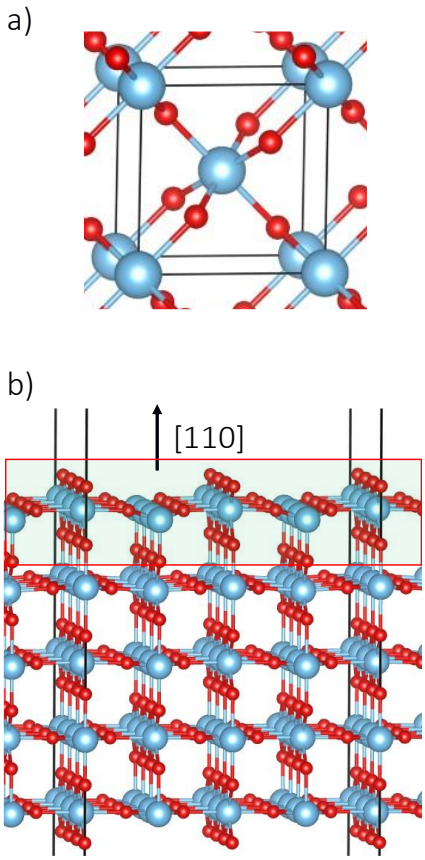

Figure 7-1(a) Equilibrium bulk geometry of rutile TiO2; (b) Relaxed surface slab of TiO2(1 1 0); Ti and O atoms are displayed in cyan and red, respectively.

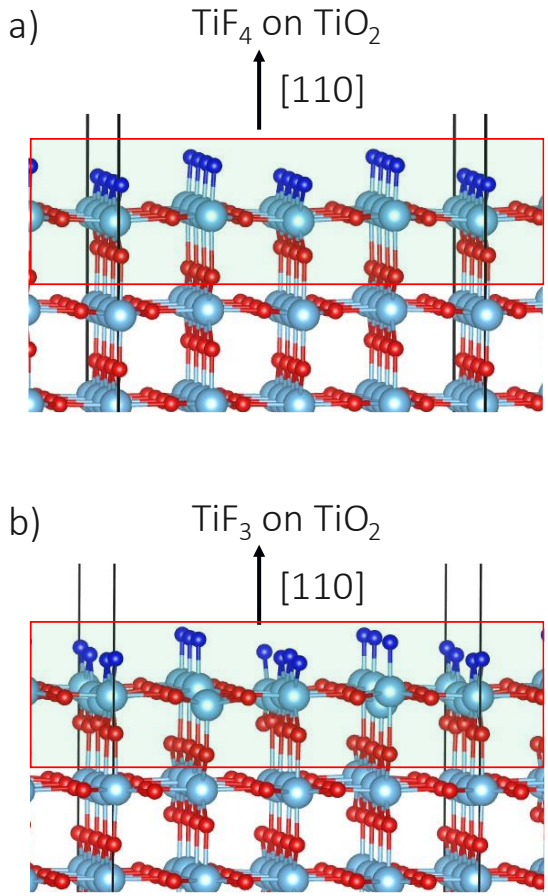

Figure 7-2: (a) Relaxed surface slab model of self-limited fluorination of TiO_2(1 1 0) as "TiF_4"; (b) Relaxed surface slab model of self-limited fluorination of TiO_2(1 1 0) as "TiF_3".

7.4 Experimental Methods

For the FTIR studies of etching, TiO_2 ALD films were first deposited on silicon nano-powder covered with native oxide (>98 % US Research Nanomaterials) that had an approximate diameter of 30 nm. This nanopowder was used to achieve a high TiO_2 surface area for greater signal-to-noise for the FTIR experiments.[82] The powder was pressed into a 1.5 × 3 cm tungsten grid that was 50 microns thick with 100 grid lines per inch.[82] The tungsten grid was resistively heated with a dc power supply (6268B, 12 V/40 A, HP) to heat to the temperatures needed for

the ALD and spontaneous etching experiments. The power supply was controlled by a PID temperature controller (Love Controls 16B, Dwyer Instruments). To monitor the temperature, a type K thermocouple was connected to the tungsten grid with a nonconductive epoxy (Cermabond 571).

TiO_2 ALD was performed in a home-built warm-walled ALD reactor equipped for FTIR studies as described previously.[168-169] For sample temperatures greater than 150C, the chamber walls were held at 150ºC and the sample was heated using the DC power supply. For sample temperatures below 150ºC, the chamber walls maintained the sample temperature. TiO_2 ALD was accomplished with sequential exposures of $TiCl_4$ (≥ 99.995% trace metals basis, Sigma-Aldrich) and H_2O at 200˚C.[162-163, 169-170] The $TiCl_4$ and H_2O reactants produce a TiO_2 ALD growth rate of □0.4 Å/cycle at 200□C.[163, 170] The resulting TiO_2 ALD films are amorphous by x-ray diffraction analysis and known to have low chlorine concentrations of □1 at% by x-ray photoelectron spectroscopy measurements.[163, 170]

During the TiO_2 ALD process, the $TiCl_4$ half-cycle was a 2 second exposure at 50-100 mTorr in viscous flow with the N_2 carrier gas. The $TiCl_4$ exposure was followed by purging with the N_2 carrier gas for 90 seconds. Then the FTIR spectrum was acquired during a scan for 60 seconds. The H_2O half-cycle consisted of a 1 second exposure at 50-80 mTorr in viscous flow with the N_2 carrier gas. The H_2O exposure was followed by purging with the N_2 carrier gas for 60 seconds. Then the FTIR spectrum was acquired during a scan for 60 seconds.

For HF exposures on TiO_2, each HF exposure was a 2 s exposure at 200 mTorr in viscous flow with the N_2 carrier gas. The HF exposure was followed by purging with the N_2 carrier gas for 90 seconds. Then the FTIR spectrum was acquired during a scan for 60 seconds. Longer purges than necessary for ALD were used to try to eliminate the possibility of HF contact with

the KBr windows during the FTIR scan. Spectra were recorded with a spectral resolution of 4 cm^{-1}. During temperature dependent reactions, the reactor was equilibrated at each temperature for 30 minutes.

The QMS investigations employed a new reactor that has been described earlier.[171] This reactor allows the study of etch products produced by flowing reactant gases through powder samples. The etch products and background gas are then expanded through an aperture and form a molecular beam. The beam of background gas and etch products are then passed through a skimmer and enter a differentially-pumped region for QMS analysis. The details of this apparatus have been given previously.[171]

The skimmer aperture diameter was 1.4 mm and the skimmer was positioned 41 mm from the sample aperture. The volatile etch products were observed using a high sensitivity, high mass quadrupole mass spectrometer (Extrel, MAX-QMS Flanged Mounted System). Each spectrum was recorded in 1 second and monitored mass intensities from 1 amu to 512 amu. After the position of the products was determined, the mass spectrum was recorded from 30 amu to 300 amu using optimized ionization energy and electron multiplier gain. An average of 100 scans were recorded during HF exposures to eliminate noise. Electron-impact ionization of gas-phase etching products was achieved with a circular thoriated iridium filament in the ionization volume inside the ionizer housing. An electron ionization energy of 70 eV was used for these experiments.

HF was first introduced into a reservoir at a pressure of 9 Torr to have a consistent HF partial pressure during the reaction. HF was leaked into the flowing N_2 background gas. The HF pressure in the sample holder containing the TiO_2 powder was 5.2 Torr. The background N_2 pressure was 2.8 Torr. TiO_2 nanopowder was purchased from US Research Nanomaterials

(99.9%, 165 nm diameter) and added to a sample holder. The mass of the TiO_2 nanopowder was recorded before and after the etching experiments were done. The mass of the nano powder before etching was 40.58 mg.

7.5 Results

7.5.1 Computed Energetics of HF Reactions with TiO_2

The possible CVE and SL reactions representing the HF pulse on TiO_2 are listed in Table 1 along with their corresponding reaction energies computed with DFT. Three sets of CVE and SL reactions are postulated for the TiO_2 and HF interaction. In the CVE1 reaction of TiO_2, 4 HF molecules are needed to etch away one unit of bulk as TiF_4 and H_2O, whereas in the CVE2 reaction, 2 HF molecules are assumed to be enough to etch a unit of TiO_2 by forming $TiOF_2$ and H_2O. These two reactions are of non-redox type since the Ti ion in the product species retains the oxidation state of +4. On the other hand, in the CVE3 reaction, the Ti^{4+} ion in TiO_2 is reduced to Ti^{3+} by forming TiF_3. The CVE2 and CVE3 reactions are computed to be unfavorable at 0 K with positive reaction energies while the CVE1 reaction is exoergic.

	Reactions	ΔE [eV/u.b.]	Y-X [eV/u.b.]
CVE1	$TiO_{2(b)}$+ 4 $HF_{(g)}$$TiF_{4(g)}$+ 2 $H_2O_{(g)}$	Y1 = -1.4	1.1
SL1	$TiO_{2(surf)}$+ 4 $HF_{(g)}$$TiF_{4(surf)}$+ 2 $H_2O_{(g)}$	X1 = -2.5	
CVE2	$TiO_{2(b)}$+ 2 $HF_{(g)}$$TiOF_{2(g)}$+ 1 $H_2O_{(g)}$	Y2 = 2.0	3.3
SL2	$TiO_{2(surf)}$+ 2 $HF_{(g)}$$TiOF_{2(surf)}$+ 1 $H_2O_{(g)}$	X2 = -1.3	
CVE3	$TiO_{2(b)}$+ 3 $HF_{(g)}$$TiF_{3(g)}$+ 1.5 $H_2O_{(g)}$+ 0.25 $O_{2(g)}$	Y3 = 2.1	2.5
SL3	$TiO_{2(surf)}$+ 3 $HF_{(g)}$$TiF_{3(surf)}$+ 1.5 $H_2O_{(g)}$+ 0.25 $O_{2(g)}$	X3 = -0.4	

Table 1: Reaction energies (ΔE) of the postulated CVE (Y) and SL (X) reactions representing the HF pulse on TiO2 along with the corresponding 'minimum thermodynamic barrier ' (Y-X) to etch. The energy values are normalized per unit bulk (u.b.) material.

Surface-limited versions of these three reactions are also postulated. The SL1, SL2 and SL3 reactions of TiO_2 are found to be energetically more favorable than the CVE1, CVE2 and CVE3 reactions, respectively. This behavior can be interpreted as the TiF units bonded on the

surface being much more favorable than TiF_x molecules in the gas phase at 0 K. CVE1 and SL1 are the most favorable reactions for TiO_2 since the minimum thermodynamic barriers (differences between CVE and SL reaction energies) of the other reaction sets are significantly larger. Therefore, the energy profile of the HF pulse at T=0 K falls under the 'preferred self-limiting' category as both SL and CVE are energetically allowed, but with CVE facing a minimum thermodynamic barrier of 1.1 eV/TiO_2.

7.5.2 Reaction Free Energy Profiles for Etching of TiO_2

FEPs of the candidate etching reactions in Table 1 are computed with a reactant pressure of 0.2 Torr and product pressure of 0.01 Torr in the temperature range 0 to 1000 K. The various contributions to the free energy of the CVE1 reaction of TiO_2 are plotted in Figure 7-3. ΔE and ΔZPE do not change with temperature and are represented as horizontal lines. The entropy term, $T\Delta S$, dominates the FEP of this reaction by spanning from 0 eV at 0 K to -0.73 eV per bulk unit at 1000 K. The entropy decreases primarily because four gaseous molecules react to produce only three product molecules, which indicates that the relative entropies of reactant and product gases play a crucial role in the temperature-dependence of the etch process. The $RT\ln(Q)$ and ΔW terms contribute relatively little in magnitude compared with the entropy term at this pressure. However, these terms do have the effect of offsetting some of the entropic increase in free energy at high temperature for CVE1. At these reactant and product pressures, the FEP shows that the CVE1 reaction is exergonic ($\Delta G < 0$) up to at least 1000 K.

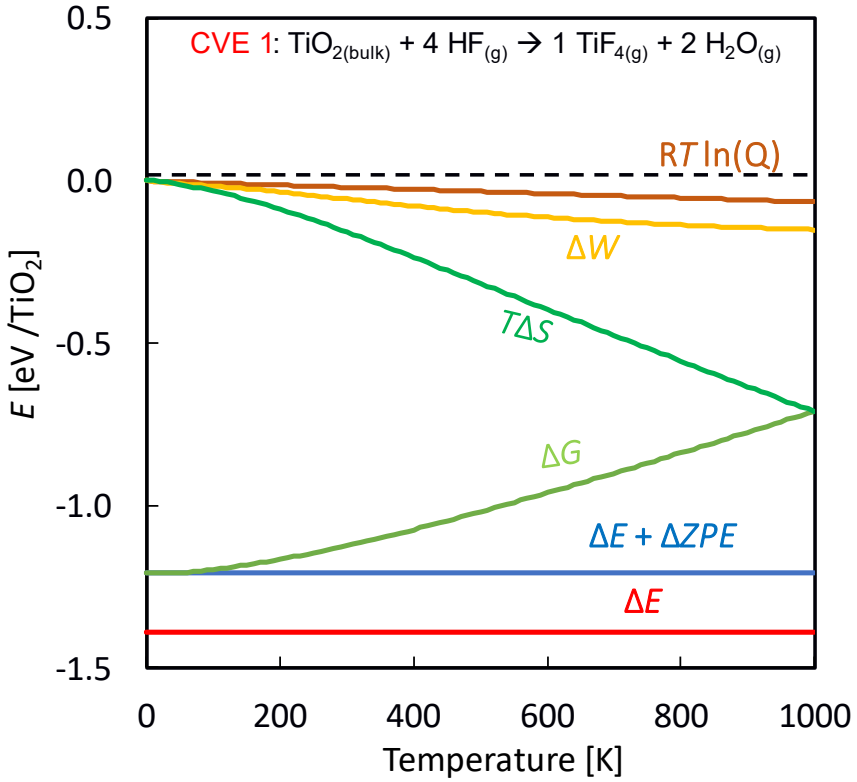

Figure 7-3: Various contributions to the reaction FEP for the CVE1 reaction of TiO_2 + HF → TiF_4 + H_2O at an HF reactant pressure of 0.2 Torr.

The FEPs of CVE and SL reactions for TiO_2 can be compared as shown in Figure 7-4. The CVE2 and CVE3 reactions have almost identical FEPs and are endergonic even though their FEPs have a negative slope. In contrast, the CVE1 reaction is fully exergonic even though its FEP has a slightly positive slope. At some very high temperature, the ΔG profiles of CVE1 and CVE2 may cross over each other. In that case, CVE2 producing $TiOF_2$ would become the most favorable etch reaction. However, judging from the slopes of their FEPs, CVE2 and CVE3 will not cross each other. Consequently, the formation of volatile TiF_3 will never be more favorable than the formation of volatile $TiOF_2$.

The SL reactions are comparatively more exoergic than the CVE counterparts at low temperatures up to 360 K (87ºC). The HF molecules passivate the TiO_2 surface and form surface-bound products in the SL reactions. As a result, there is a significant entropic penalty that is evident in the strongly positive slope of the FEPs of the SL reactions. The SL3 reaction is unfavorable at all temperatures above 70 K, which indicates that reduction by HF of surface Ti atoms to TiO_{2-x} is unlikely.

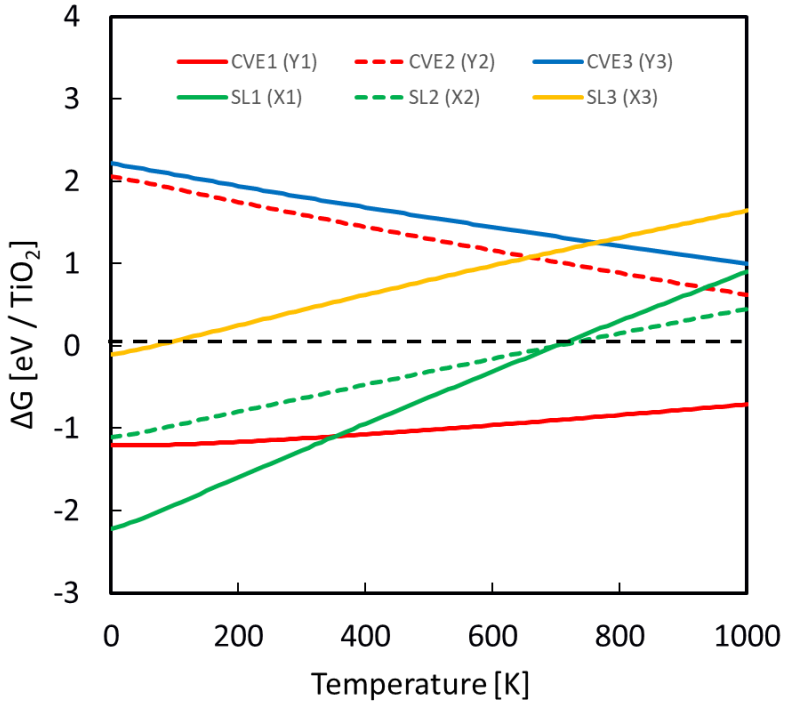

Figure 7-4: FEPs for the CVE1, CVE2, CVE3, SL1 SL2 and SL3 reactions for HF interacting with TiO_2 versus temperature. The labels X and Y correspond to the values listed in Table 1.

Considering only the most favorable reactions, CVE1 and SL1, the graph in Figure 7-5 can be divided into three regions. The FEPs of the CVE1 and SL1 reactions cross at 360 K (87ºC). The region between 0 K and 360 K is labelled as 'preferred self-limiting', since the SL1

reaction is the most favorable in this region and the 'minimum thermodynamic barrier' for SL1 to CVE1 is positive. HF etching of the bulk by CVE1 is possible in this region if the energetic barrier, including kinetic requirement, can be overcome at the reactor conditions. The 'minimum thermodynamic barrier' drops from a value of 1.1 eV per bulk unit at 0 K to zero at 360 K where the CVE1 and SL1 reactions become equally favorable for producing by-products at pressure of 0.01 Torr.

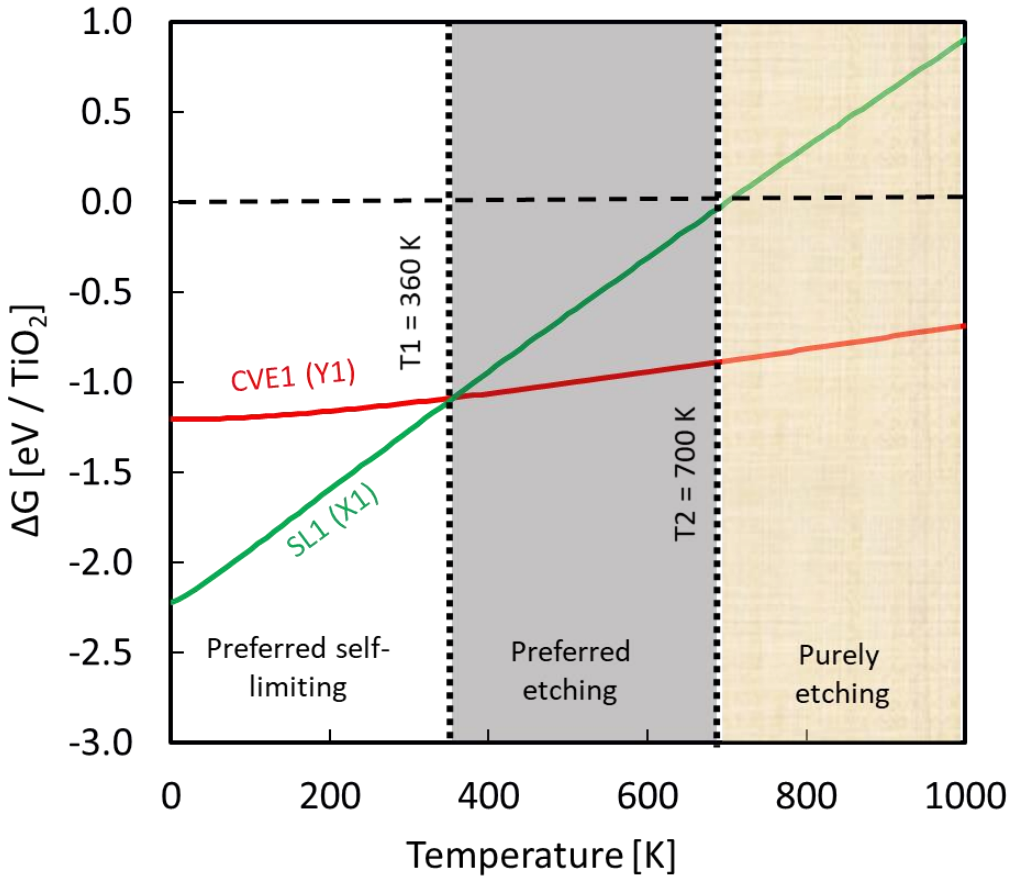

Figure 7-5: FEPs of CVE1 and SL1 showing three regions : preferred self-limiting, preferred etching and purely etching. SL1 and CVE1 line crossing occurs at 360 K (87ºC).

The region between 360 K (87ºC) and 700 K (427ºC) is called ‘preferred etching’, since fluorination of the surface by reaction SL1 is possible, but the CVE1 reaction to volatile TiF_4 is more favored. The actual etch pathway may face kinetic barriers that have not been computed in this study. The SL1 reaction becomes endergonic beyond 700 K and this temperature region is labelled ‘purely etching’. This label suggests that, at these high temperatures, the surface may resist fluorination via SL1, which may constitute a barrier towards the formation of volatile TiF_4 (for CVE1), though we have no data on such details of the mechanism.

7.5.3 Influence of Reactant and Product Pressures

The etch reactions have been considered above at a constant reactant (HF) pressure of 0.2 Torr and a by-product pressure of 0.01 Torr. The reactant gas pressure can be controlled in the reactor. However, the product pressure is not an experimentally adjustable parameter. Any change in the reactant and product pressures will alter the slope of the FEPs due to the contributions from the $RT \ln(Q)$ term, and will hence change the process window. This is now shown for the CVE1 and SL1 reactions of TiO_2 under changes in reactant (HF) pressure from 0.01 Torr to 4 Torr at a constant by-product pressure of 0.01 Torr.

Figure 7-6a and Figure 7-6b display color maps showing the free energy changes of the CVE1 and SL1 reactions of TiO_2 along with the minimum thermodynamic barrier for etching (CVE1-SL1) in Figure 7-6c. The CVE1 reaction shown in Figure 7-6d is mostly favorable in the entire reactant pressure range. CVE1 also becomes more favorable at high temperatures and high reactant pressure. Consequently, an increase of the reactant pressure decreases the slope of the FEP of the CVE1 reaction. In the SL1 reaction shown in Figure 7-6b, the favorable region is pushed to higher temperatures at higher reactant pressure.

From the minimum thermodynamic barrier map in Figure 7-6c, the SL1 reaction is computed to be preferred up to 360 K (87°C) for the entire reactant pressure range. This means that the temperature at which the FEPs of the CVE1 and SL1 reactions cross over is constant with respect to increase in the reactant pressure, under the assumption of a constant product pressure. This behavior occurs because the number of reactant HF molecules per unit TiO_2 is the same for both CVE1 and SL1 reactions. In the 'purely etching' region (ΔG(SL1) > 0 and ΔG(CVE1) < 0), the minimum thermodynamic barrier to etch decreases at higher reactant pressure.

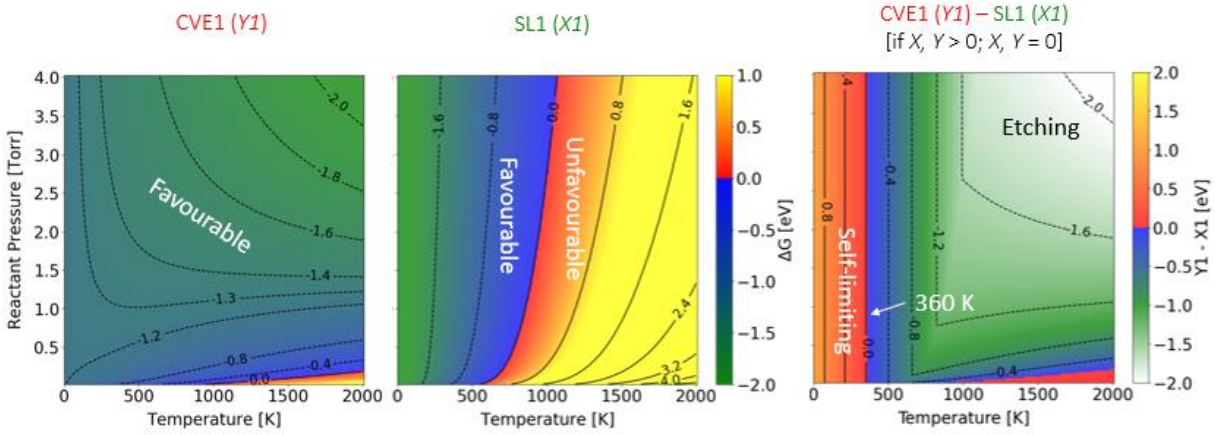

Figure 7-6: 'Heat' maps showing the change in free energy of (a) CVE1 and (b) SL1 reactions for HF exposure on TiO_2. (c) Change in corresponding minimum thermodynamic barrier with respect to reactant pressure and temperature.

7.5.4 FTIR Spectroscopy

Figure 7-7 shows the progressive growth of a TiO_2 film during 36 ALD cycles on silicon nanoparticles measured by the infrared absorbance. $TiCl_4$ and H_2O were employed as the reactants at 200°C for TiO_2 ALD. The spectra are referenced to the original silicon nanoparticle sample that has a thin native oxide of the silicon surface. The absorption peak at 400 - 960 cm^{-1}

corresponds to Ti-O stretching vibrations. The Ti-O stretching vibrations yield a peak at 722 cm^{-1} that increases linearly with number of $TiCl_4$ and H_2O cycles.

The initial cycles of TiO_2 ALD also give rise to several other absorption peaks at 1209 cm^{-1}, 1048 cm^{-1} and 940 cm^{-1}. The vibrational band at 1209 cm^{-1} is assigned to Si-O vibrations that arise due to the oxidation of the silicon powder with H_2O exposures. This peak grows rapidly during the first 10 TiO_2 ALD cycles and then the growth slows at higher TiO_2 ALD film thicknesses. The bands at 940 cm^{-1} and 1048 cm^{-1} are assigned to Si-O-Ti vibrations resulting from the mixing of TiO_2 and SiO_2 at the interface. These vibrational bands also do not increase further as TiO_2 ALD continues past 30 cycles.

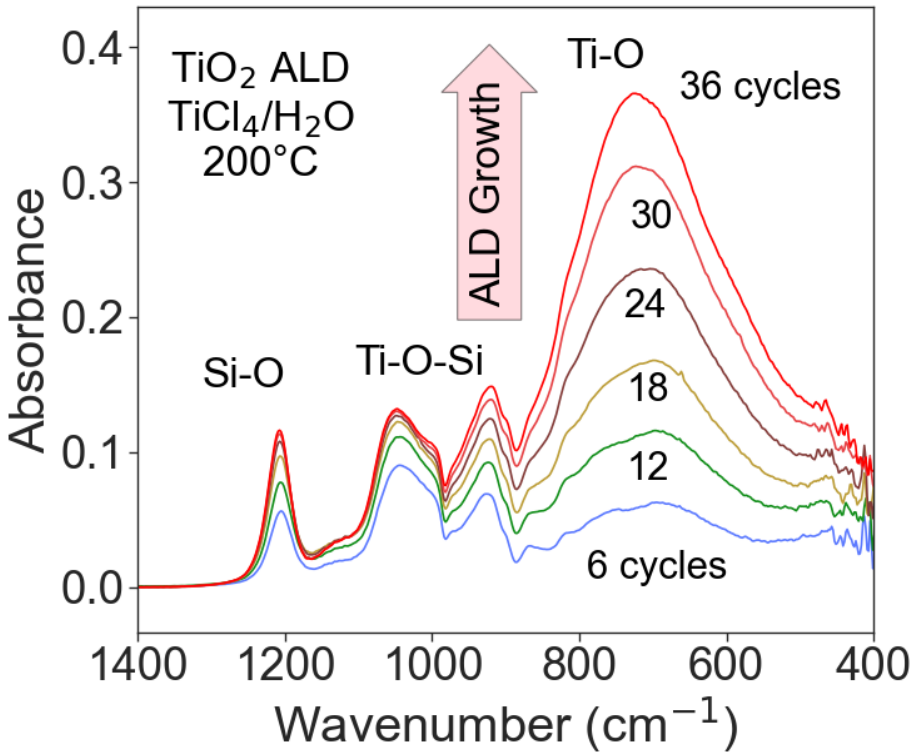

Figure 7-7: FTIR absorbance during TiO_2 ALD on silicon nanoparticles at 200ºC versus number of ALD cycles using $TiCl_4$ and H_2O as the reactants.

The etching of the TiO_2 ALD films by HF was studied by monitoring the changes to the FTIR spectrum. Another TiO_2 ALD film was grown using multiple TiO_2 ALD cycles. Figure 7-8 shows the difference spectrum after the first exposure of HF at 200 mTorr for 2 s at 280°C. This difference spectrum is referenced to the infrared spectrum from the last 20 cycles used to grow the TiO_2 ALD film. The vertical axis for this reference spectrum has been scaled and shown in Figure 7-8. The comparison between the difference spectrum and the reference spectrum reveals that the HF exposure removes the TiO_2 ALD film. The difference spectrum displays a broad decrease in absorbance at 400 - 960 cm^{-1} that is consistent with the spectrum for the TiO_2 ALD film.

There is also a new feature in Figure 7-8 that is not in agreement with the loss of the absorbance from the Ti-O stretching vibration. This feature is observed as an absorption peak at 777 cm^{-1}. This absorption feature is assigned to a Ti-F stretching vibration. The difference spectrum is consistent with the HF exposure spontaneously etching TiO_2 and leaving the TiO_2 surface terminated with Ti-F species after the HF exposure. This Ti-F surface species may be viewed as an intermediate on the way to volatile etch species. The expected possible volatile etch products from the spontaneous etching of TiO_2 by HF may be TiF_4 or $TiOF_2$, which is checked by QMS measurements and DFT calculations.

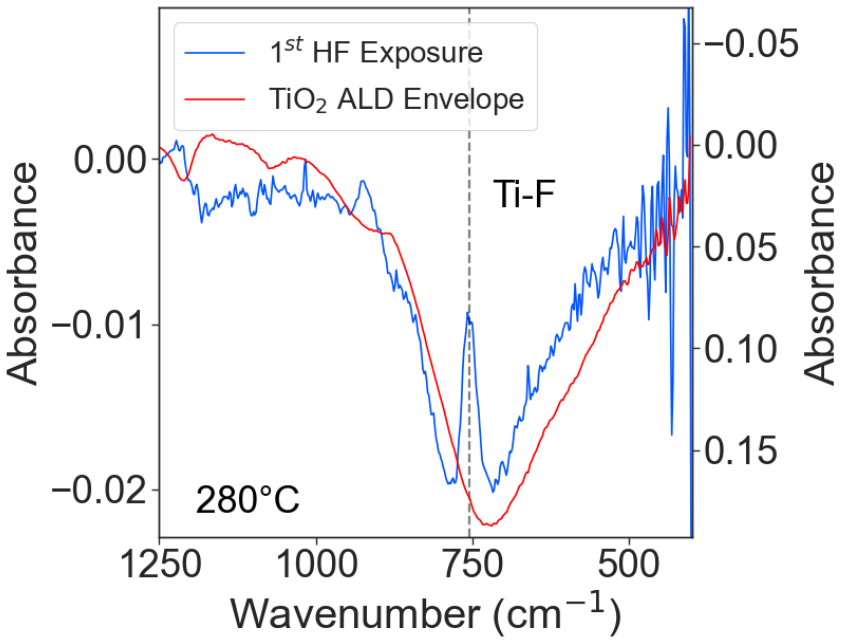

Figure 7-8: FTIR difference spectrum for the first HF exposure on TiO_2. Difference spectrum was obtained using the FTIR absorbance spectrum for TiO_2 ALD after 36 cycles as a reference. Absorbance for TiO_2 ALD film after 36 cycles is also shown for comparison

Figure 7-9 shows the difference spectra after 1, 3, 5, and 10 HF exposures at 200 mTorr for 2 seconds at 280ºC. The starting sample was a TiO_2 ALD film deposited after 60 ALD cycles. The difference spectra are referenced to the absorption spectrum for this TiO_2 ALD film. The decrease of the absorbance for the Ti-O stretching vibration between 500 cm^{-1} and 900 cm^{-1} in Figure 7-9 is linear with respect to the HF exposure. The continuous loss of TiO_2 indicates spontaneous etching (CVE) during each HF exposure.

Figure 7-9 also provides confirmation that the absorption feature at 777 cm^{-1} corresponds to a Ti-F surface species. This absorption peak at 777 cm^{-1} persists through the 1st, 3rd, 5th and 10th HF exposures. The size of this absorption feature also remains constant during the ten HF

exposures. These results are expected since the surface area of Ti-F surface species stays constant as the TiO_2 ALD film is progressively removed by spontaneous etching.

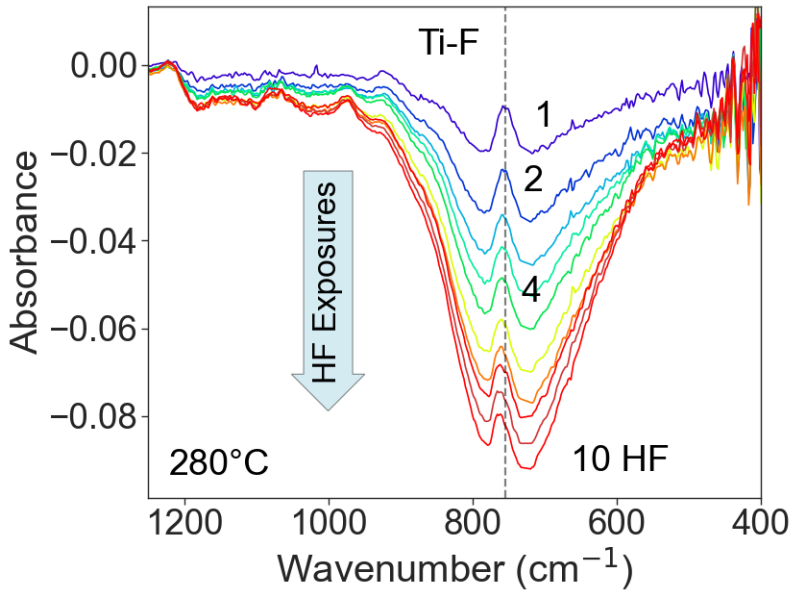

Figure 7-9: FTIR difference spectra after 10 sequential HF exposures at 280ºC on TiO_2 ALD films. Absorbance feature at 777 cm^{-1} is assigned to Ti-F stretching vibration.

The spontaneous etching of TiO_2 increases at higher substrate temperature. To quantify the spontaneous etching rate, experiments were performed at 14 different temperatures between 80˚C and 300˚C. The change in FTIR absorbance was integrated over the frequency range 400 to 960 cm^{-1} after each HF exposure for 10 HF exposures at each temperature. This change in the integrated absorbance during each HF exposure is proportional to the TiO_2 etch rate, which is shown in Figure 7-10. There is a small but measurable integrated absorbance loss at temperatures as low as 80ºC (353 K), but not at lower temperatures. The TiO_2 etching starts to increase more noticeably at approximately 150ºC (423 K). The etch rate increases progressively with temperature up to 300ºC (573 K). These results for the spontaneous etching of TiO_2 are in

agreement with previous experiments that revealed the spontaneous etching of TiO_2 ALD films by HF exposures at 200, 250 and 300ºC using quartz crystal microbalance (QCM) measurements. A central question in this paper is whether this temperature window for etching can be predicted computationally.

The change in the integrated absorbance during each HF exposure can also be related to the thickness of the TiO_2 ALD film. From the results in Figure 7-7, an integrated absorbance (units of absorbance x cm^{-1}) of 118 cm^{-1} is obtained from 400 cm^{-1} to 960 cm^{-1} after 36 TiO_2 ALD cycles at 200ºC. Previous TiO_2 ALD studies have measured a TiO_2 ALD growth rate of 0.4 Å/cycle using $TiCl_4$ and H_2O as the reactants at 200ºC. Using this growth rate, the integrated absorbance of 118 cm^{-1} after 36 TiO_2 ALD cycles can be equated to a TiO_2 ALD film thickness of 14.4 Å. Using this correlation between integrated absorbance and TiO_2 film thickness, the TiO_2 film thickness removed for the HF exposure of 200 mTorr for 2 s at 300□C is estimated to be 0.5 Å.

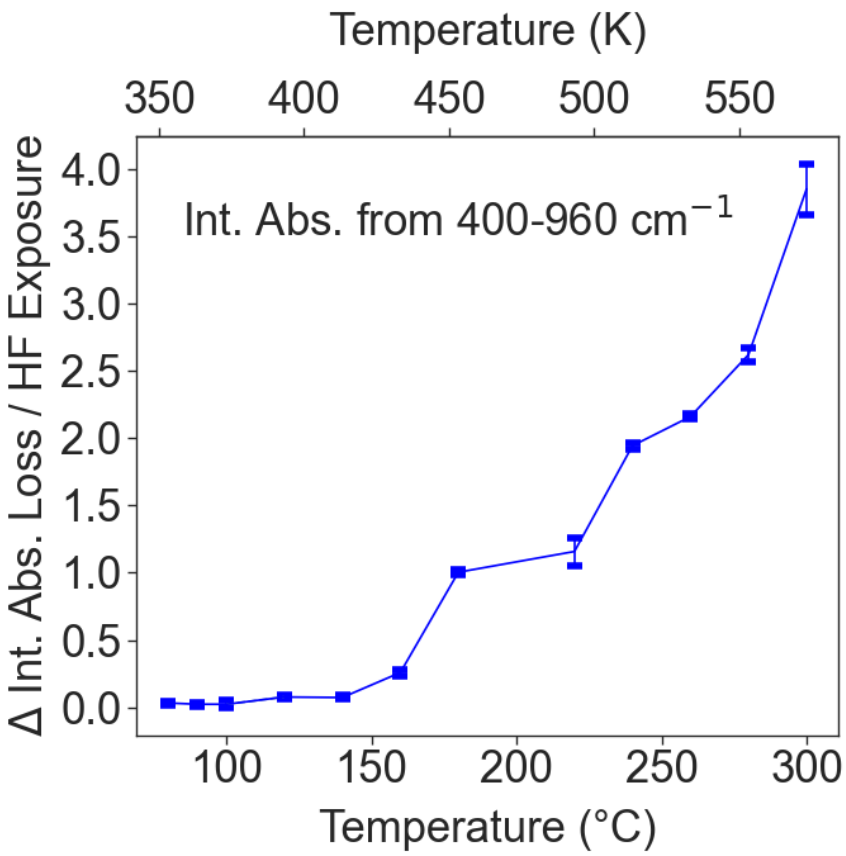

Figure 7-10: Etch rate as measured by change in integrated absorbance of the Ti-O vibrational modes from 400-960 cm^{-1} for each HF exposure. Temperature is varied from 80ºC to 300ºC.

Figure 7-11 shows the Arrhenius plot of the temperature-dependent etch rates. This plot of the logarithm of the etch rate versus 1/T is approximately linear. The slope of the Arrhenius plot yields an activation energy of E_a = 42 kJ/mol. This activation energy is presumably associated with the kinetics of the rate-limiting mechanistic step during HF etching of TiO_2.

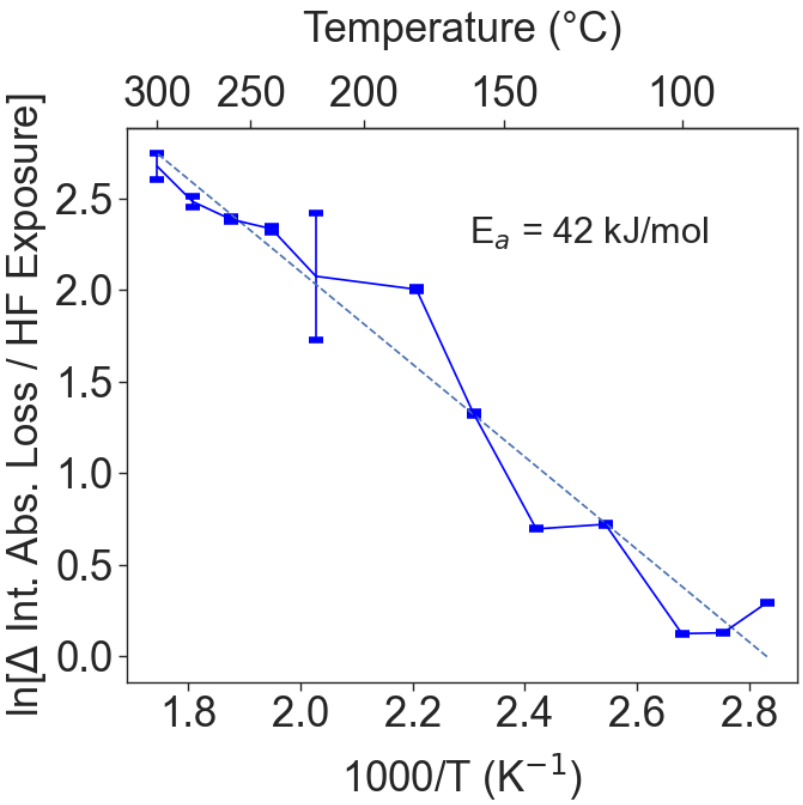

Figure 7-11: Arrhenius plot obtained from etch rates versus temperature presented in Figure 7-10. Slope of the plot yields an activation barrier of Ea = 42 kJ/mol.

7.5.5 QMS Spectrometry

Quadrupole mass spectroscopy was used to investigate the volatile etch species produced when HF interacts with TiO_2 at 300ºC. Figure 7-12a shows the mass spectrum from 46 amu to 110 amu that reveal the peaks for TiF_3^+, TiF_2^+, TiF^+ and Ti^+. The TiF_3^+ fragments have the highest intensity. The main fragment for TiF_3^+ is at m/z = 105 amu. These titanium fluoride species are assigned to the cracking fragments of TiF_4^+. The small peaks found at 55 and 57 amu correspond to hydrocarbons that are often observed during heating of the filament for electron impact ionization.

Figure 7-12b expands the mass spectrum around 105 amu. The TiF_3^+ fragment can be confirmed by the Ti isotopic ratios. Due to the isotopes of titanium, there are expected peaks at 103, 104, 105, 106, and 107 amu with intensities of 10.8%, 9.9%, 100%, 7.5%, and 7.3%, respectively. These expectations accurately match the intensities of the peaks observed for the TiF_3^+ fragment. TiF_3^+ could be a fragment of TiF_4^+. However, TiF_4^+ was not observed in the mass spectrum. TiF_4 would be consistent with the CVE1 reaction (see section XX) where the expected product is $TiF_{4(g)}$. There also could be small contributions from the CVE3 reaction if the product was $TiF_{3(g)}$. TiF_3 is not likely as the parent because TiF_3 is a solid with a very high melting point of 1200ºC. In contrast, TiF_4 has a much lower melting point of 377ºC.

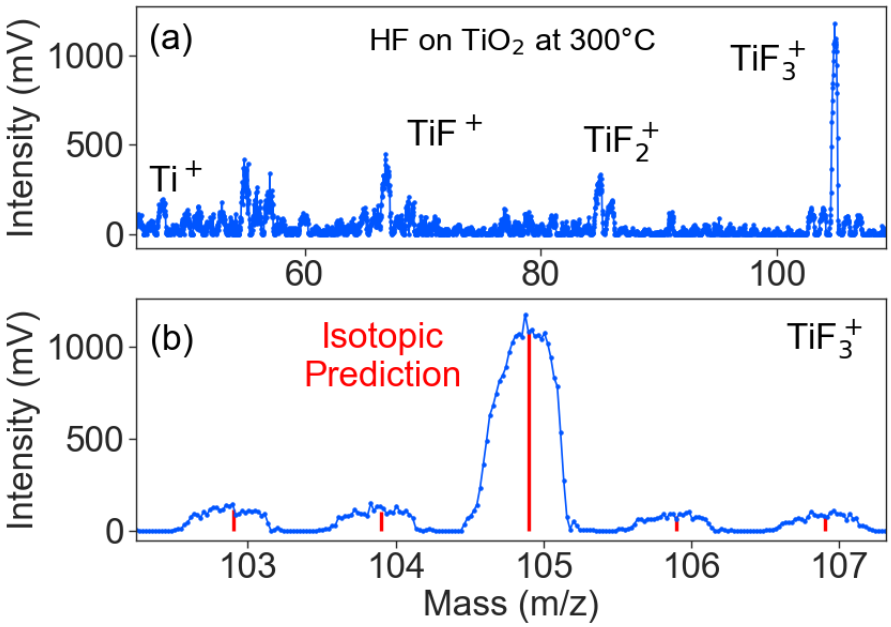

Figure 7-12: (a) TiF_x^+ mass species observed during HF exposure on TiO_2 powder at 300ºC. (b) Expansion of the mass range around the main TiF_3^+ fragment at m/z = 105 amu showing the measured signals and the predicted signals based on the Ti isotopes.

Figure 7-13 shows the intensity of the TiF_x fragments during the HF exposure with a duration of 2 minutes. All TiF_x fragments rise and fall with the HF exposure. The intensity of the TiF^+ peak has a higher background intensity resulting from small hydrocarbons desorbing from the filament at 86 amu. All the TiF_x^+ fragments are attributed to TiF_4. The absence of the TiF_4 parent may result from its complete fragmentation during ionization.

Figure 7-14a shows the increase in the H_2O^+ intensity at 18 amu and Figure 7-14b shows the increase in the HF^+ intensity at 20 amu during the HF exposure with a duration of 2 minutes. The H_2O^+ signal rises and falls with the HF exposure. H_2O is an expected product of both the CVE1 and CVE3 reactions where $TiF_{4(g)}$ and $TiF_{3(g)}$ are the respective products. The mass signal for O_2 at 32 amu did not have an increase during the HF exposure. After the etching experiments, the mass of the powder was measured to investigate the mass decrease resulting from etching. The final mass was 31.26 mg compared with 40.58 mg before etching. The etching resulted in a 23% decrease in the mass of the TiO_2 nanopowder.

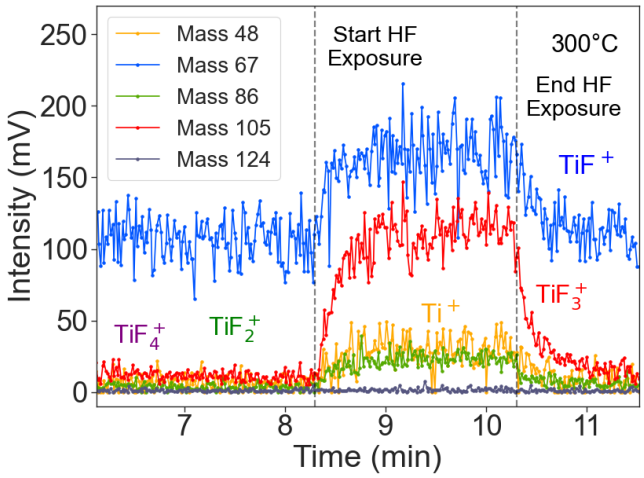

Figure 7-13: Mass spectrometry scans for TiF_4^+, TiF_3^+, TiF_2^+, TiF^+ and Ti^+ during an HF exposure lasting 2 minutes. All TiF_x^+ species rise and fall with the HF exposure.

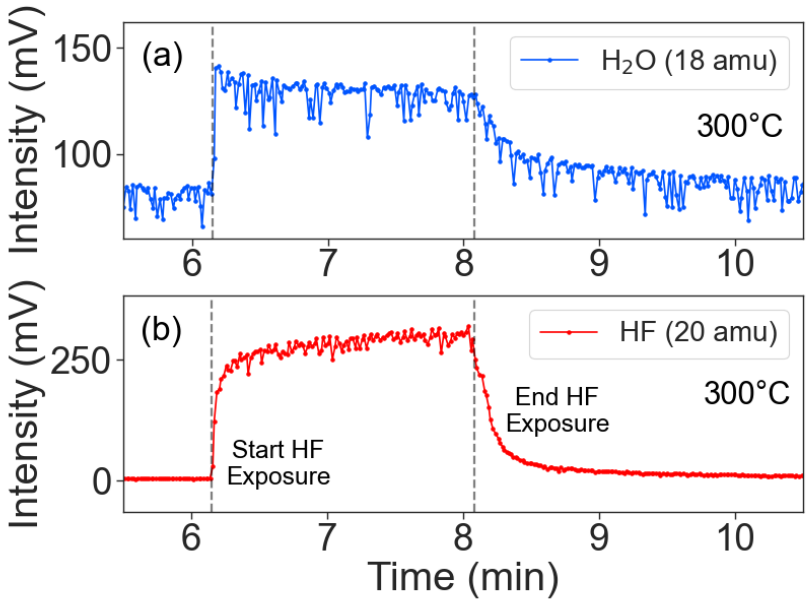

Figure 7-14: Mass spectrometry scans for (a) H_2O^+ and (b) HF during an HF exposure lasting 2 minutes. The H_2O^+ intensity rises and falls with the HF exposure.

7.6 Discussion

The FEPs of postulated SL and CVE reactions for HF exposure on TiO_2 were calculated over wide temperature and pressure ranges of interest. Experimental results were also obtained for the etch onset, etch rate versus temperature and etch products. The onset temperature was the first temperature where the change in the integrated FTIR absorbance of the Ti-O vibrational band was found to be non-negligible. The FTIR measurements showed that the spontaneous etch of TiO_2 (a CVE-type reaction) was favorable from an onset temperature of 80-90□C, which agrees with the theoretical prediction that the continuous etching of TiO_2 by reaction CVE1 dominates at temperatures greater than 360 K ($87_{\circ}$C). In this case, the predicted onset temperature is based on crossover of the computed *thermodynamics* of the candidate etching

reactions. The correlation between the experimental and theoretical onset temperature counters the common assumption that onset temperatures are exclusively a reflection of reaction kinetics.

The calculations show that the surface remains completely passivated with Ti-F species due to the self-limiting SL1 reaction at temperatures below the onset temperature. The FTIR difference spectra in Figure 7-8 also show a persistent Ti-F signal and the loss of Ti-O signal after each HF pulse on the TiO_2 surface at 280□C (553 K). At this temperature, the HF pulse is predicted to be in the 'preferred etching' state where both SL1 and CVE1 reactions are favorable and compete with each other, but with CVE1 more thermochemically favorable . The favorability of CVE1 explains why spontaneous etching and loss of Ti-O signal is observed in Figure 7-8. The Ti-F signal at the surface is observed because the FTIR measurement takes place after the HF exposure. The F-covered TiO_2 surface from the SL1 reaction is preserved because Ti-F is a favorable surface intermediate at this temperature.

The mass spectrometry measurements identify TiF_4 and H_2O as the volatile etch products during HF exposure on TiO_2. These volatile etch products are consistent with the reaction products of the CVE1 reaction pathway that is computed to be favorable, *i.e.* $TiO_2 + HF \square TiF_4 + H_2O$. There were no observed $TiOF_2$ products in agreement with a thermodynamically unfavorable CVE2 reaction. There was also no detection of an O_2 etch product in agreement with the thermodynamically unfavorable SL3 pathway.

This computational model generates thermodynamic information from a few DFT calculations on relatively small systems (*i.e.* bulk crystal, gas-phase molecules and idealized surface slabs), which makes the model suitable for screening large numbers of candidate chemistries and designing new ALE processes. To look at the mechanism and kinetics underlying the process would require more time-consuming calculations. We expect that such

calculations would show which individual steps in the CVE1 reaction are responsible for the measured activation energy (E_a=42 kJ/mol, Figure 7-11). This activation energy may be the barrier for diffusion of Ti and O atoms from sub-surface layers to the fluorinated surface, prior to desorption as TiF_4 and H_2O respectively.

7.7 Conclusion

A combined computational and experimental approach has been presented to understand the competition between self-limiting and continuous etch reactions in an ALE process using HF exposures on TiO_2 as an example. In situ FTIR spectroscopy was used to study etch rates and surface species during the etching of TiO_2 with HF exposure. In situ mass spectrometry was also employed to identify the volatile etch products. The HF exposure was predicted to continuously etch TiO_2 in the temperature window 360-770 K (87-497°C). There was excellent agreement between the onset temperature for the TiO_2 spontaneous etching of 87ºC calculated by the simulations and threshold for absorbance change at 80-90ºC measured by FTIR spectroscopy. The calculations also determined that an increase in the reactant pressure did not alter the etching onset temperature of the preferred etching pathway.

HF was predicted to passivate the TiO_2 surface with Ti-F species in a self-limiting reaction at temperatures up to 360 K (87ºC) and FTIR spectroscopy confirmed the presence of Ti-F surface species after HF exposures. The calculations predicted that TiO_2 was more favorably etched as TiF_4 rather than TiF_3 or $TiOF_2$, and this was confirmed in the observation of cracking fragments of TiF_4 in mass spectrometry.

This study illustrates that the competition between self-limiting and continuous reactions can be predicted with straightforward DFT calculations and used to determine the temperature

window for ALE processes. In addition, theory can predict the expected volatile etch products and surface species resulting from the self-limiting reactions. This theoretical approach has also been experimentally validated using HF exposures on TiO_2. These theoretical predictions can therefore guide experiments to more efficiently develop viable ALE processes. This method of understanding the competition between self-limiting and continuous reactions should be useful for rapid high-throughput screening of precursors and various substrates to design new thermal ALE processes.

7.8 Acknowledgements

The work at the University of Colorado was funded by Intel Corporation through a directed research grant from the Semiconductor Research Corporation. Additional support for the new mass spectrometry apparatus was provided by Lam Research. The authors SKN and SDE thank the Irish Centre for High-End Computing (project code: tiche077c) and the Science Foundation Ireland-funded computing cluster at Tyndall for the computer time.

References

1. Kanarik, K. J.; Lill, T.; Hudson, E. A.; Sriraman, S.; Tan, S.; Marks, J.; Vahedi, V.; Gottscho, R. A., Overview of Atomic Layer Etching in the Semiconductor Industry. *J. Vac. Sci. Technol. A* **2015,** *33* (2), 020802.
2. Kanarik, K. J.; Tan, S.; Gottscho, R. A., Atomic Layer Etching: Rethinking the Art of Etch. *J. Phys. Chem. Lett.* **2018,** *9* (16), 4814-4821.
3. Mack, C. A., Fifty Years of Moore's Law. *IEEE Transactions on Semiconductor Manufacturing* **2011,** *24* (2), 202-207.
4. Donnelly, V. M.; Kornblit, A., Plasma etching: Yesterday, today, and tomorrow. *J. Vac. Sci. Technol. A* **2013,** *31* (5), 050825.
5. Abe, H.; Yoneda, M.; Fujlwara, N., Developments of plasma etching technology for fabricating semiconductor devices. *Jpn. J. Appl. Phys.* **2008,** *47* (3), 1435-1455.
6. Smith, D. L., *Thin-Film Deposition Principles and Practice*. McGraw-Hill: 1995; p 644.
7. Coburn, J. W.; Winters, H. F., Ion- and electron-assisted gas-surface chemistry—An important effect in plasma etching. *Journal of Applied Physics* **1979,** *50* (5), 3189-3196.
8. Kanarik, K. J.; Tan, S.; Yang, W.; Kim, T.; Lill, T.; Kabansky, A.; Hudson, E. A.; Ohba, T.; Nojiri, K.; Yu, J.; Wise, R.; Berry, I. L.; Pan, Y.; Marks, J.; Gottscho, R. A., Predicting synergy in atomic layer etching. *Journal of Vacuum Science & Technology A: Vacuum, Surfaces, and Films* **2017,** *35*, 05C302.
9. George, S. M., Atomic Layer Deposition: An Overview. *Chem. Rev.* **2010,** *110*, 111-131.
10. George, S. M., Mechanisms of Thermal Atomic Layer Etching. *Acc. Chem. Res.* **2020,** *53* (6), 1151-1160.
11. Mackus, A. J. M.; Faraz, T.; Chittock, N., Etching with atomic-level precision. *NEVAC blad* **2020,** *58* (2), 40-42.
12. Fischer, A.; Routzahn, A.; George, S. M.; Lill, T., Thermal atomic layer etching: A review. *Journal of Vacuum Science & Technology A* **2021,** *39* (3), 030801.
13. Lemaire, P. C.; Parsons, G. N., Thermal Selective Vapor Etching of TiO2: Chemical Vapor Etching via WF6 and Self-Limiting Atomic Layer Etching Using WF6 and BCl3. *Chem. Mater.* **2017,** *29* (16), 6653-6665.
14. Gertsch, J. C.; Cano, A. M.; Bright, V. M.; George, S. M., SF4 as the Fluorination Reactant for Al2O3 and VO2 Thermal Atomic Layer Etching. *Chemistry of Materials* **2019,** *31* (10), 3624-3635.
15. Johnson, N. R.; Hite, J. K.; Mastro, M. A.; Eddy, C. R.; George, S. M., Thermal atomic layer etching of crystalline GaN using sequential exposures of XeF2 and BCl3. *Applied Physics Letters* **2019,** *114* (24), 243103.

16. Zywotko, D. R.; George, S. M., Thermal Atomic Layer Etching of ZnO by a "Conversion-Etch" Mechanism Using Sequential Exposures of Hydrogen Fluoride and Trimethylaluminum. *Chem. Mater.* **2017,** *29* (3), 1183-1191.
17. DuMont, J. W.; Marquardt, A. E.; Cano, A. M.; George, S. M., Thermal Atomic Layer Etching of SiO2 by a "Conversion-Etch" Mechanism Using Sequential Reactions of Trimethylaluminum and Hydrogen Fluoride. *ACS Appl. Mater. Interfaces* **2017,** *9* (11), 10296-10307.
18. Abdulagatov, A. I.; George, S. M., Thermal Atomic Layer Etching of Silicon Using O2, HF, and Al(CH3)3 as the Reactants. *Chemistry of Materials* **2018,** *30* (23), 8465-8475.
19. Abdulagatov, A. I.; George, S. M., Thermal atomic layer etching of silicon nitride using an oxidation and "conversion etch" mechanism. *Journal of Vacuum Science & Technology A* **2020,** *38* (2), 022607.
20. Cano, A. M.; Marquardt, A. E.; DuMont, J. W.; George, S. M., Effect of HF Pressure on Thermal Al2O3 Atomic Layer Etch Rates and Al2O3 Fluorination. *The Journal of Physical Chemistry C* **2019,** *123* (16), 10346-10355.
21. Hennessy, J.; Moore, C. S.; Balasubramanian, K.; Jewell, A. D.; France, K.; Nikzad, S., Enhanced Atomic Layer Etching of Native Aluminum Oxide for Ultraviolet Optical Applications. *J. Vac. Sci. Technol. A* **2017,** *35* (4), 041512.
22. Lee, Y.; DuMont, J. W.; George, S. M., Trimethylaluminum as the Metal Precursor for the Atomic Layer Etching of Al2O3 Using Sequential, Self-Limiting Thermal Reactions. *Chem. Mater.* **2016,** *28* (9), 2994-3003.
23. Clancey, J. W.; George, S. M., In Situ Mass Spectrometer Studies of Volatile Etch Products During Al_2O_3 Atomic Layer Etching Using HF and Trimethylaluminum. *4th International Atomic Layer Etching Workshop, Denver, Colorado, Poster Presentation, July 15-17, 2017, Denver, Colorado.*
24. Carver, C. T.; Plombon, J. J.; Romero, P. E.; Suri, S.; Tronic, T. A.; Turkot, R. B., Atomic Layer Etching: An Industry Perspective. *ECS Journal ofSolid State Science and Technology* **2015,** *4* (6), N5005-N5009.
25. Lu, W.; Lee, Y.; Murdzek, J.; Gertsch, J.; Vardi, A.; Kong, L.; George, S. M.; A. del Alamo, J., First Transistor Demonstration of Thermal Atomic Layer Etching: InGaAs FinFETs with sub-5 nm Fin-width Featuring in situ ALE-ALD. In *IEDM*, 2018.
26. Hu, C., *Modern Semiconductor Devices for Integrated Circuits*. Prentice Hall: 2010.
27. Mohan, L.; Singh, G.; Kaur, M., FinFET based 6T SRAM Cell for Nanoscaled Technologies. *International Journal of Computer Applications* **2015,** *127* (13), 5.
28. Lee, Y.; DuMont, J. W.; George, S. M., Atomic Layer Etching of HfO_2 Using Sequential, Self-Limiting Thermal Reactions with $Sn(acac)_2$ and HF. *ESC J. Solid State Sci. Technol.* **2015,** *4*, N5013-N5022.
29. Nellis, S. IBM unveils 2-nanometer chip technology for faster computing. https://www.reuters.com/technology/ibm-unveils-2-nanometer-chip-technology-faster-computing-2021-05-06/ (accessed October 26th).
30. Smith, B., *Fundamentals of Fourier Transform Infrared Spectroscopy*. Taylor & Francis Group: 2011.
31. Subramanian, A.; Rodriguez-Saona, L., Fourier Transform Infrared (FTIR) Spectroscopy. *Infrared Spectroscopy for Food Quality Analysis and Control* **2009**, 145-178.

32. Hadjiivanov, K., Identification and Characterization of Surface Hydroxyl Groups by Infrared Spectroscopy. **2014,** *57*, 99-318.
33. Bose, O.; Kemnitz, E.; Lippitz, A.; Unger, W. E. S., C 1s and Au 4f(7/2) Referenced XPS Binding Energy Data Obtained with Different Aluminium Oxides, Hydroxides and Fluorides. *Fresenius J. Anal. Chem.* **1997,** *358* (1-2), 175-179.
34. Chabal, Y. J.; Higashi, G. S.; Raghavachari, K.; Burrows, V. A., Infrared spectroscopy of Si(111) and Si(100) surfaces after HF treatment: Hydrogen termination and surface morphology. *Journal of Vacuum Science & Technology A: Vacuum, Surfaces, and Films* **1989,** *7* (3), 2104-2109.
35. Queeney, K. T.; Weldon, M. K.; Chang, J. P.; Chabal, Y. J.; Gurevich, A. B.; Sapjeta, J.; Opila, R. L., Infrared spectroscopic analysis of the Si/SiO2 interface structure of thermally oxidized silicon. *J. Appl. Phys.* **2000,** *87* (3), 1322-1330.
36. Dupuie, J. L.; Gulari, E., The low temperature catalyzed chemical vapor deposition and characterization of aluminum nitride thin films. *Journal of Vacuum Science & Technology A: Vacuum, Surfaces, and Films* **1992,** *10* (1), 18-28.
37. Lu, Y. F.; Ren, Z. M.; Chong, T. C.; Cheong, B. A.; Chow, S. K.; Wang, J. P., Ion-assisted pulsed laser deposition of aluminum nitride thin films. *Journal of Applied Physics* **2000,** *87* (3), 1540-1542.
38. Ragolski, A., History of Infrared Detectors. *OPTO–ELECTRONICS REVIEW* **2012,** *20* (3), 279–308.
39. Tompkins, H.; Hilfiker, J., *Spectroscopic ellipsometry Practical Application to Thin Film Characterization-Momentum Press (2016).pdf*>. Momentum Press: 2016; p 197.
40. Wagner, J. M., *X-ray Photoelectron Spectroscopy*. Nova Science Publishers: 2011.
41. Roodenko, K.; Halls, M. D.; Gogte, Y.; Seitz, O.; Veyan, J. F.; Chabal, Y. J., Nature of Hydrophilic Aluminum Fluoride and Oxyaluminum Fluoride Surfaces Resulting from XeF_2 Treatment of Al and Al_2O_3. *J. Phys. Chem. C* **2011,** *115* (43), 21351-21357.
42. Sherwood, P. M. A., Introduction to Studies of Aluminum and its Compounds by XPS. *Surface Science Spectra* **1998,** *5* (1), 1-3.
43. Tougaard, S., Improved XPS analysis by visual inspection of the survey spectrum. *Surface and Interface Analysis* **2018,** *50* (6), 657-666.
44. Matsuura, T.; Murota, J.; Sawada, Y.; Ohmi, T., Self-Limited Layer-by-Layer Etching of Si by Alternated Chlorine Adsorption and Ar^+ Ion Irradiation *Appl. Phys. Lett.* **1993,** *63* (20), 2803-2805.
45. Park, S. D.; Lee, D. H.; Yeom, G. Y., Atomic Layer Etching of Si(100) and Si(111) Using Cl_2 and Ar Neutral Beam. *Electrochem Solid St* **2005,** *8* (8), C106-C109.
46. Sakaue, H.; Iseda, S.; Asami, K.; Yamamoto, J.; Hirose, M.; Horiike, Y., Atomic Layer Controlled Digital Etching of Silicon. *Jpn. J. Appl. Phys. 1* **1990,** *29* (11), 2648-2652.
47. Sugiyama, T.; Matsuura, T.; Murota, J., Atomic-Layer Etching of Ge Using an Ultraclean ECR Plasma. *Appl. Surf. Sci.* **1997,** *112*, 187-190.
48. Lim, W. S.; Park, S. D.; Park, B. J.; Yeom, G. Y., Atomic Layer Etching of (100)/(111) GaAs with Chlorine and Low Angle Forward Reflected Ne Neutral Beam. *Surf. Coat. Tech.* **2008,** *202* (22-23), 5701-5704.
49. Metzler, D.; Bruce, R. L.; Engelmann, S.; Joseph, E. A.; Oehrlein, G. S., Fluorocarbon Assisted Atomic Layer Etching of SiO_2 Using Cyclic Ar/C_4F_8 Plasma. *J. Vac. Sci. Technol. A* **2014,** *32* (2), 020603.

50. Metzler, D.; Li, C.; Engelmann, S.; Bruce, R. L.; Joseph, E. A.; Oehrlein, G. S., Fluorocarbon Assisted Atomic Layer Etching of SiO_2 and Si Using Cyclic Ar/C_4F_8 and Ar/CHF_3 Plasma. *J. Vac. Sci. Technol. A* **2016,** *34* (1), 01b101.
51. Park, J. B.; Lim, W. S.; Park, B. J.; Park, I. H.; Kim, Y. W.; Yeom, G. Y., Atomic Layer Etching of Ultra-Thin HfO_2 Film for Gate Oxide in MOSFET Sevices. *J. Phys. D-Appl. Phys.* **2009,** *42* (5), 055202.
52. Li, C.; Metzler, D.; Lai, C. S.; Hudson, E. A.; Oehrlein, G. S., Fluorocarbon Based Atomic Layer Etching of Si_3N_4 and Etching Selectivity of SiO_2 Over Si_3N_4. *J. Vac. Sci. Technol. A* **2016,** *34* (4), 041307.
53. Kim, Y. Y.; Lim, W. S.; Park, J. B.; Yeom, G. Y., Layer by Layer Etching of the Highly Oriented Pyrolythic Graphite by Using Atomic Layer Etching. *J. Electrochem. Soc.* **2011,** *158* (12), D710-D714.
54. Vogli, E.; Metzler, D.; Oehrlein, G. S., Feasibility of Atomic Layer Etching of Polymer Material Based on Sequential O_2 Exposure and Ar Low-Pressure Plasma-Etching. *Appl. Phys. Lett.* **2013,** *102* (25), 253105.
55. Lee, Y.; George, S. M., Atomic Layer Etching of Al_2O_3 Using Sequential, Self-Limiting Thermal Reactions with $Sn(acac)_2$ and HF. *ACS Nano* **2015,** *9*, 2061-2070.
56. George, S. M.; Lee, Y., Prospects for Thermal Atomic Layer Etching Using Sequential, Self-Limiting Fluorination and Ligand-Exchange Reactions. *ACS Nano* **2016,** *10* (5), 4889-4894.
57. Lee, Y.; George, S. M., Thermal Atomic Layer Etching of Titanium Nitride Using Sequential, Self-Limiting Reactions: Oxidation to TiO2 and Fluorination to Volatile TiF4. *Chem. Mater.* **2017,** *29* (19), 8202-8210.
58. DuMont, J. W.; George, S. M., Competition Between Al_2O_3 Atomic Layer Etching and AlF_3 Atomic Layer Deposition Using Sequential Exposures of Trimethylaluminum and Hydrogen Fluoride. *J Chem Phys* **2017,** *146* (5), 052819.
59. Lee, Y.; DuMont, J. W.; George, S. M., Mechanism of Thermal Al_2O_3 Atomic Layer Etching Using Sequential Reactions with $Sn(acac)_2$ and HF. *Chem. Mater.* **2015,** *27* (10), 3648-3657.
60. Lee, Y.; George, S. M., Thermal Atomic Layer Etching of HfO_2 Using HF for Fluorination and $TiCl_4$ for Ligand-Exchange. *J. Vac. Sci. Technol. A* **2018,** *36*, 061504.
61. Johnson, N. R.; George, S. M., WO3 and W Thermal Atomic Layer Etching Using "Conversion-Fluorination" and "Oxidation-Conversion-Fluorination" Mechanisms. *ACS Appl. Mater. Interfaces* **2017,** *9* (39), 34435-34447.
62. Xie, W. Y.; Lemaire, P. C.; Parsons, G. N., Thermally Driven Self-Limiting Atomic Layer Etching of Metallic Tungsten Using WF_6 and O_2. *ACS Appl. Mater. Interfaces* **2018,** *10* (10), 9147-9154.
63. Johnson, N. R.; Sun, H. X.; Sharma, K.; George, S. M., Thermal Atomic Layer Etching of Crystalline Aluminum Nitride Using Sequential, Self-limiting Hydrogen Fluoride and $Sn(acac)_2$ Reactions and Enhancement by H_2 and Ar Plasmas. *J. Vac. Sci. Technol. A* **2016,** *34* (5), 050603.
64. Faraz, T.; Roozeboom, F.; Knoops, H. C. M.; Kessels, W. M. M., Atomic Layer Etching: What Can We Learn from Atomic Layer Deposition? *ECS J. Solid State Sci. Technol.* **2015,** *4* (6), N5023-N5032.

65. George, S. M., Atomic Layer Deposition: An Overview. *Chem. Rev.* **2010,** *110* (1), 111-131.
66. Quan, J. L.; Teng, B. T.; Wen, X. D.; Zhao, Y.; Liu, R.; Luo, M. F., Hydrogen Fluoride Adsorption and Reaction on the alpha-Al_2O_3(0001) Surface: A Density Functional Theory Study. *J. Chem. Phys.* **2012,** *136* (11), 114701.
67. Wirth, J.; Schacht, J.; Saalfrank, P.; Paulus, B., Fluorination of the Hydroxylated alpha-Al_2O_3 (0001) and Its Implications for Water Adsorption: A Theoretical Study. *J. Phys. Chem. C* **2016,** *120* (18), 9713-9718.
68. Natarajan, S. K.; Elliott, S. D., Modeling the Chemical Mechanism of the Thermal Atomic Layer Etch of Aluminum Oxide: A Density Functional Theory Study of Reactions during HF Exposure. *Chem. Mater.* **2018,** *30* (17), 5912-5922.
69. Bendada, A.; Webb, G.; Winfield, J. M., Fluorination of Gamma-Alumina by Sulphur Tetrafluoride, Thionyl Fluoride, Carbonyl Fluoride or Anhydrous Hydrogen Fluoride: A Radiotracer Study. *Eur. J. Solid State Inorg. Chem.* **1996,** *33* (9), 907-916.
70. Kemnitz, E.; Menz, D. H., Fluorinated Metal Oxides and Metal Fluorides as Heterogeneous Catalysts. *Prog. Solid State Chem.* **1998,** *26* (2), 97-153.
71. Elam, J. W.; Groner, M. D.; George, S. M., Viscous Flow Reactor with Quartz Crystal Microbalance for Thin Film Growth by Atomic Layer Deposition. *Rev. Sci. Instrum.* **2002,** *73*, 2981–2987.
72. DuMont, J. W.; George, S. M., Pyrolysis of Alucone Molecular Layer Deposition Films Studied Using In Situ Transmission Fourier Transform Infrared Spectroscopy. *J Phys Chem C* **2015,** *119* (26), 14603-14612.
73. Hess, D. W.; Deal, B. E., Kinetics of Thermal Oxidation of Silicon in O_2-N_2 Mixtures at 1200 C. *J. Electrochem. Soc.* **1975,** *122* (4), 579-581.
74. Kamigaki, Y.; Itoh, Y., Thermal Oxidation of Silicon in Various Oxygen Partial Pressures Diluted by Nitrogen. *J. Appl. Phys.* **1977,** *48* (7), 2891-2896.
75. Deal, B. E.; Grove, A. S., General Relationship for Thermal Oxidation of Silicon. *J. Appl. Phys.* **1965,** *36* (12), 3770-3778.
76. Moulder, J. F.; Stickle, W. F.; Sobol, P. E.; Bomben, K. D., *Handbook of X-ray Photoelectron Spectroscopy*. Perkin-Elmer Corporation, Physical Electronics Division: Eden Praire, Minnesota, 1992.
77. Mangolini, F.; McClimon, J. B.; Rose, F.; Carpick, R. W., Accounting for Nanometer-Thick Adventitious Carbon Contamination in X-Ray Absorption Spectra of Carbon-Based Materials. *Anal. Chem.* **2014,** *86* (24), 12258-12265.
78. Fadley, C. S.; Baird, R. J.; Siekhaus, W.; Novakov, T.; Bergstrom, S. A., Surface Analysis and Angular Distributions in X-ray Photoelectron Spectroscopy. *J. Electron. Spectrosc. Relat. Phenom.* **1974,** *4* (2), 93-137.
79. McCafferty, E.; Wightman, J. P., An X-ray Photoelectron Spectroscopy Sputter Profile Study of the Native Air-Formed Oxide Film on Titanium. *Appl. Surf. Sci.* **1999,** *143* (1-4), 92-100.
80. Seah, M. P.; Dench, W. A., Quantitative Electron Spectroscopy of Surfaces: A Standard Data Base for Electron Inelastic Mean Free Paths in Solids. *Surf. Interface Anal.* **1979,** *1*, 2-11.
81. Tanuma, S.; Powell, C. J.; Penn, D. R., Calculations of Electron Inelastic Mean Free Paths for 31 Materials. *Surf. Interface Anal.* **1988,** *11* (11), 577-589.

82. Ferguson, J. D.; Weimer, A. W.; George, S. M., Atomic layer deposition of ultrathin and conformal Al2O3 films on BN particles. *Thin Solid Films* **2000,** *371* (1-2), 95-104.
83. Jost, W., *Diffusion in Solids, Liquids, Gases*. Academic Press Inc. Publishers: New York, 1952.
84. Massoud, H. Z.; Plummer, J. D.; Irene, E. A., Thermal-Oxidation of Silicon in Dry Oxygen Growth-Rate Enhancement in the Thin Regime .1. Experimental Results. *J Electrochem Soc* **1985,** *132* (11), 2685-2693.
85. Fischer, A.; Routzahn, A.; George, S. M.; Lill, T., Thermal atomic layer etching: A review. *J. Vac. Sci. Technol. A* **2021,** *39* (3), 030801.
86. Fischer, A.; Routzahn, A.; Lee, Y.; Lill, T.; George, S. M., Thermal etching of AlF3 and thermal atomic layer etching of Al2O3. *J. Vac. Sci. Technol. A* **2020,** *38* (2), 022603.
87. Lee, Y.; DuMont, J. W.; Cavanagh, A. S.; George, S. M., Atomic Layer Deposition of AlF3 Using Trimethylaluminum and Hydrogen Fluoride. *J. Phys. Chem. C* **2015,** *119* (25), 14185-14194.
88. Lee, Y.; George, S. M., Atomic Layer Etching of Al_2O_3 Using Sequential, Self-limiting Thermal Reactions with $Sn(acac)_2$ and Hydrogen Fluoride. *ACS Nano* **2015,** *9*, 2061-2070.
89. Lee, Y.; Huffman, C.; George, S. M., Selectivity in Thermal Atomic Layer Etching Using Sequential, Self-Limiting Fluorination and Ligand-Exchange Reactions. *Chem. Mater.* **2016,** *28*, 7657-7665.
90. Hickman, A. L.; Chaudhuri, R.; Bader, S. J.; Nomoto, K.; Li, L.; Hwang, J. C. M.; Grace Xing, H.; Jena, D., Next generation electronics on the ultrawide-bandgap aluminum nitride platform. *Semiconductor Science and Technology* **2021,** *36* (4), 044001.
91. Yang, J.; Si, C.; Han, G.; Zhang, M.; Ma, L.; Zhao, Y.; Ning, J., Researching the Aluminum Nitride Etching Process for Application in MEMS Resonators. *Micromachines* **2015,** *6* (2), 281-290.
92. DuMont, J. W.; George, S. M., Pyrolysis of Alucone Molecular Layer Deposition Films Studied Using In Situ Transmission Fourier Transform Infrared Spectroscopy. *J. Phys. Chem. C* **2015,** *119* (26), 14603-14612.
93. Joo, H.-Y.; Kim, H. J.; Kim, S. J.; Kim, S. Y., Spectrophotometric analysis of aluminum nitride thin films. *Journal of Vacuum Science & Technology A: Vacuum, Surfaces, and Films* **1999,** *17* (3), 862-870.
94. Easwarakhanthan, T.; Hussain, S. S.; Pigeat, P., Spectroellipsometric investigation of optical, morphological, and structural properties of reactively sputtered polycrystalline AlN films. *Journal of Vacuum Science & Technology A: Vacuum, Surfaces, and Films* **2010,** *28* (3), 495-501.
95. Ren, Z. M.; Lu, Y. F.; Ni, H. Q.; Liew, T. Y. F.; Cheong, B. A.; Chow, S. K.; Ng, M. L.; Wang, J. P., Room temperature synthesis of c-AlN thin films by nitrogen-ion-assisted pulsed laser deposition. *Journal of Applied Physics* **2000,** *88* (12), 7346-7350.
96. Catherine, Y.; Talebian, A., Plasma Deposition of Aluminum Oxide Films. *Journal of Electronic Materials* **1988,** *17* (2), 127-134.
97. Frank, M. M.; Chabal, Y. J.; Wilk, G. D., Nucleation and interface formation mechanisms in atomic layer deposition of gate oxides. *Applied Physics Letters* **2003,** *82* (26), 4758-4760.

98. Myers, T. J.; Cano, A. M.; Lancaster, D. K.; Clancey, J. W.; George, S. M., Conversion reactions in atomic layer processing with emphasis on ZnO conversion to Al2O3 by trimethylaluminum. *Journal of Vacuum Science & Technology A* **2021,** *39* (2), 021001.
99. Murdzek, J. A.; George, S. M., Effect of crystallinity on thermal atomic layer etching of hafnium oxide, zirconium oxide, and hafnium zirconium oxide. *Journal of Vacuum Science & Technology A* **2020,** *38* (2), 022608.
100. Murdzek, J. A.; Rajashekhar, A.; Makala, R. S.; George, S. M., Thermal atomic layer etching of amorphous and crystalline Al2O3 films. *Journal of Vacuum Science & Technology A* **2021,** *39* (4), 042602.
101. Lii-Rosales, A.; Cavanagh, A. S.; Fischer, A.; Lill, T.; George, S. M., Spontaneous Etching of Metal Fluorides Using Ligand-Exchange Reactions: Landscape Revealed by Mass Spectrometry. *Chem. Mater.* **2021,** *doi.org/10.1021/acs.chemmater.1c01950*.
102. Ramos, R.; Cunge, G.; Pelissier, B.; Joubert, O., Cleaning aluminum fluoride coatings from plasma reactor walls in SiCl4/Cl2plasmas. *Plasma Sources Science and Technology* **2007,** *16* (4), 711-715.
103. Rosenberger, L.; Baird, R.; McCullen, E.; Auner, G.; Shreve, G., XPS analysis of aluminum nitride films deposited by plasma source molecular beam epitaxy. *Surface and Interface Analysis* **2008,** *40* (9), 1254-1261.
104. Miller, A. C.; Simmons, G. W., Copper by XPS. *Surface Science Spectra* **1993,** *2* (1), 55-60.
105. Haynes, W. M., *CRC Handbook of Chemistry and Physics (92nd ed.)*. CRC Press: 2011.
106. Chittock, N. J.; Vos, M. F. J.; Faraz, T.; Kessels, W. M. M.; Knoops, H. C. M.; Mackus, A. J. M., Isotropic plasma atomic layer etching of Al2O3 using a fluorine containing plasma and Al(CH3)3. *Applied Physics Letters* **2020,** *117* (16), 162107.
107. Lii-Rosales, A.; Cavanagh, A. S.; Fischer, A.; Lill, T.; George, S. M., Spontaneous Etching of Metal Fluorides Using Ligand-Exchange Reactions: Landscape Revealed by Mass Spectrometry. *Chemistry of Materials* **2021,** *33*, 7719−7730.
108. Parsons, J. L., Vibrational Spectra of Orthorhombic Metaboric Acid. *J. Chem. Phys.* **1960,** *33* (6), 1860-1866.
109. Ibbotson, D. E.; Mucha, J. A.; Flamm, D. L.; Cook, J. M., PLASMALESS DRY ETCHING OF SILICON WITH FLUORINE-CONTAINING COMPOUNDS. *J. Appl. Phys.* **1984,** *56* (10), 2939-2942.
110. Winters, H. F.; Coburn, J. W., ETCHING OF SILICON WITH XEF2 VAPOR. *Appl. Phys. Lett.* **1979,** *34* (1), 70-73.
111. Kovacs, G. T. A.; Maluf, N. I.; Petersen, K. E., Bulk micromachining of silicon. *Proc. IEEE* **1998,** *86* (8), 1536-1551.
112. Williams, K. R.; Gupta, K.; Wasilik, M., Etch rates for micromachining processing - Part II. *J. Microelectromech. Syst.* **2003,** *12* (6), 761-778.
113. Williams, K. R.; Muller, R. S., Etch rates for micromachining processing. *J. Microelectromech. Syst.* **1996,** *5* (4), 256-269.
114. Arana, L. R.; de Mas, N.; Schmidt, R.; Franz, A. J.; Schmidt, M. A.; Jensen, K. F., Isotropic etching of silicon in fluorine gas for MEMS micromachining. *J. Micromech. Microeng.* **2007,** *17* (2), 384-392.
115. Winters, H. F., THE ETCHING OF W(111) WITH XEF2. *J. Vac. Sci. Technol. A* **1985,** *3* (3), 700-704.

116. Winters, H. F., ETCH PRODUCTS FROM THE REACTION ON CL-2 WITH AL(100) AND CU(100) AND XEF2 WITH W(111) AND NB. *J. Vac. Sci. Technol. B* **1985,** *3* (1), 9-15.
117. Winters, H. F., THE ETCHING OF CU(100) WITH CL-2. *J. Vac. Sci. Technol. A* **1985,** *3* (3), 786-790.
118. Chen, J. K. C.; Altieri, N. D.; Kim, T.; Chen, E.; Lill, T.; Shen, M. H.; Chang, J. P., Directional etch of magnetic and noble metals. II. Organic chemical vapor etch. *J. Vac. Sci. Technol. A* **2017,** *35* (5), 05c305.
119. George, M. A.; Hess, D. W.; Beck, S. E.; Ivankovits, J. C.; Bohling, D. A.; Lane, A. P., REACTION OF 1,1,1,5,5,5-HEXAFLUORO-2,4-PENTANEDIONE (H(+)HFAC) WITH CUO, CU2O, AND CU FILMS. *J. Electrochem. Soc.* **1995,** *142* (3), 961-965.
120. George, M. A.; Hess, D. W.; Beck, S. E.; Young, K.; Bohling, D. A.; Voloshin, G.; Lane, A. P., Reaction of 1,1,1,5,5,5-hexafluoro-2,4-pentanedione (H(+)hfac) with iron and iron oxide thin films. *J. Electrochem. Soc.* **1996,** *143* (10), 3257-3266.
121. Helms, C. R.; Deal, B. E., Mechanisms of the HF/H2O vapor phase etching of SiO2. *J. Vac. Sci. Technol. A* **1991,** *10* (4), 806-811.
122. Mullins, R.; Natarajan, S. K.; Elliott, S. D.; Nolan, M., Self-Limiting Temperature Window for Thermal Atomic Layer Etching of HfO2 and ZrO2 Based on the Atomic-Scale Mechanism. *Chem. Mater.* **2020,** *32* (8), 3414-3426.
123. Perdew, J. P.; Burke, K.; Ernzerhof, M., Generalized Gradient Approximation Made Simple. *Phys. Rev. Lett.* **1996,** *77* (18), 3865-3868.
124. Kresse, G.; Furthmuller, J., Efficient iterative schemes for ab initio total-energy calculations using a plane-wave basis set. *Phys. Rev. B* **1996,** *54* (16), 11169-11186.
125. Kresse, G.; Joubert, D., From ultrasoft pseudopotentials to the projector augmented-wave method. *Phys. Rev. B* **1999,** *59* (3), 1758-1775.
126. Blöchl, P. E., Projector augmented-wave method. *Phys. Rev. B* **1994,** *50* (24), 17953-17979.
127. Togo, A.; Tanaka, I., First Principles Phonon Calculations in Materials Science. *Scr. Mater.* **2015,** *108*, 1-5.
128. Persson, K., Materials Data on B2O3 (SG:152). Materials Project., 2014.
129. Putkonen, M.; Niinistö, L., Atomic layer deposition of B2O3 thin films at room temperature. *Thin Solid Films* **2006,** *514* (1-2), 145-149.
130. Ogden, J. S.; Young, N. A., THE CHARACTERIZATION OF MOLECULAR BORIC-ACID BY MASS-SPECTROMETRY AND MATRIX-ISOLATION INFRARED-SPECTROSCOPY. *J. Chem. Soc., Dalton Trans.* **1988,** (6), 1645-1652.
131. Tenney, A. S.; Wong, J., VIBRATIONAL-SPECTRA OF VAPOR-DEPOSITED BINARY BOROSILICATE GLASSES. *J. Chem. Phys.* **1972,** *56* (11), 5516-+.
132. Vick, G. L.; Whittle, K. M., Solid Solubility and Diffusion Coefficients of Boron in Silicon. *J. Electrochem. Soc.* **1969,** *116* (8), 1142-1144.
133. Peak, D.; Luther, G. W.; Sparks, D. L., ATR-FTIR spectroscopic studies of boric acid adsorption on hydrous ferric oxide. *Geochim. Cosmochim. Acta* **2003,** *67* (14), 2551-2560.
134. Scruby, R. E.; Lacher, J. R.; Park, J. D., The Infrared Spectrum of Boron Trichloride. *J. Chem. Phys.* **1951,** *19* (3), 386-387.
135. Gong, Y.; Zhou, M. F., Matrix isolation infrared spectroscopic and theoretical study of the hydrolysis of boron dioxide in solid argon. *J. Phys. Chem. A* **2008,** *112* (25), 5670-5675.

136. Ayotte, P.; Hebert, M.; Marchand, P., Why is hydrofluoric acid a weak acid? *J. Chem. Phys.* **2005,** *123* (18).
137. DuMont, J. W.; George, S. M., Competition between Al2O3 atomic layer etching and AlF3 atomic layer deposition using sequential exposures of trimethylaluminum and hydrogen fluoride. *J. Chem. Phys.* **2017,** *146* (5).
138. Dows, D. A., INFRARED SPECTRUM OF CRYSTALLINE BORON TRIFLUORIDE. *J. Chem. Phys.* **1959,** *31* (6), 1637-1639.
139. Nxumalo, L. M.; Ford, T. A., INFRARED-SPECTRUM OF THE BORON-TRIFLUORIDE DIMER. *Vib. Spectrosc.* **1994,** *6* (3), 333-343.
140. Saenz, P.; Cachau, R. E.; Seoane, G.; Kieninger, M.; Ventura, O. N., A New Perspective in the Lewis Acid Catalyzed Ring Opening of Epoxides. Theoretical Study of Some Complexes of Methanol, Acetic Acid, Dimethyl Ether, Diethyl Ether, and Ethylene Oxide with Boron Trifluoride. *J. Phys. Chem. A* **2006,** *110*, 11734-11751.
141. Ultee, C. J., Infrared Studies of the B2O3–BF3 System. *J. Chem. Phys.* **1964,** *40* (12), 3746-3747.
142. Porter, R. F.; Bidinosti, D. R.; Watterson, K. F., Mass Spectrometric Study of the Reactions of BF3(g) with BCl3(g), B(OH)3(g), and B2O3(1). *J. Chem. Phys.* **1962,** *36* (8), 2104-2108.
143. Bidinosti, D. R.; Coatsworth, L. L., Mass spectrometric study of the reaction of BF3 with B2O3; the identification and heat of formation of B2OF4. *Can. J. Chem.* **1970,** *48*, 2484-2487.
144. Puurunen, R. L., Surface chemistry of atomic layer deposition: A case study for the trimethylaluminum/water process. *J. Appl. Phys.* **2005,** *97*, 121301.
145. Elliott, S. D., Atomic-Scale Simulation of ALD Chemistry. *Semicond. Sci. Technol.* **2012,** *27*, 74008.
146. Kim, H.; Lee, H. B. R.; Maeng, W. J., Applications of Atomic Layer Deposition to Nanofabrication and Emerging Nanodevices. *Thin Solid Films* **2009,** *517* (8), 2563-2580.
147. Knez, M.; Niesch, K.; Niinisto, L., Synthesis and Surface Engineering of Complex Nanostructures by Atomic Layer Deposition. *Adv. Mater.* **2007,** *19* (21), 3425-3438.
148. Carver, C. T.; Plombon, J. J.; Romero, P. E.; Suri, S.; Tronic, T. A.; Turkot, R. B., Atomic Layer Etching: An Industry Perspective. *ECS J. Solid State Sci. Technol.* **2015,** *4* (6), N5005-N5009.
149. Kanarik, K. J.; Tan, S.; Gottscho, R. A., Atomic Layer Etching: Rethinking the Art of Etch. In *Journal of Physical Chemistry Letters*, American Chemical Society: 2018; Vol. 9, pp 4814-4821.
150. Song, S. K.; Saare, H.; Parsons, G. N., Integrated Isothermal Atomic Layer Deposition/Atomic Layer Etching Supercycles for Area-Selective Deposition of TiO_2. *Chem. Mater.* **2019,** *31* (13), 4793-4804.
151. Tan, S.; Yang, W.; Kanarik, K. J.; Lill, T.; Vahedi, V.; Marks, J.; Gottscho, R. A., Highly Selective Directional Atomic Layer Etching of Silicon. *ECS J. Solid State Sci. Technol.* **2015,** *4*, N5010-N5012.
152. Mullins, R.; Kondati Natarajan, S.; Elliott, S. D.; Nolan, M., Self-Limiting Temperature Window for Thermal Atomic Layer Etching of HfO_2 and ZrO_2 Based on the Atomic-Scale Mechanism *Chem. Mater.* **2020,** *32*, 3414-3426.

153. Filatova, E. A.; Hausmann, D.; Elliott, S. D., Investigating Routes Toward Atomic Layer Deposition of Silicon Carbide: Ab initio Screening of Potential Silicon and Carbon Precursors *J. Vac. Sci. Technol. A* **2017,** *35*, 01B103.
154. Lee, Y.; George, S. M., Thermal Atomic Layer Etching of HfO_2 Using HF for Fluorination and $TiCl_4$ for Ligand-Exchange *J. Vac. Sci. Technol. A* **2018,** *36*, 061504.
155. Xie, W.; Lemaire, P. C.; Parsons, G. N., Thermally Driven Self-Limiting Atomic Layer Etching of Metallic Tungsten Using WF_6 and O_2. *ACS Appl. Mater. Interfaces* **2018,** *10*, 9147-9154.
156. Lemaire, P. C.; Parsons, G. N., Thermal Selective Vapor Etching of TiO2: Chemical Vapor Etching via WF6 and Self-Limiting Atomic Layer Etching Using WF6 and BCl3. *Chemistry of Materials* **2017,** *29*, 6653-6665.
157. Chase, M. W., NIST-JANAF Thermochemical Tables, 4th Edition.
158. Kondati Natarajan, S.; Elliott, S. D., Modeling the Chemical Mechanism of the Thermal Atomic Layer Etch of Aluminum Oxide: A Density Functional Theory Study of Reactions during HF Exposure. *Chem. Mater.* **2018,** *30*, 5912-5922.
159. Diebold, U., The Surface Science of Titanium Dioxide. *Surf. Sci. Rep.* **2003,** *48* (5-8), 53-229.
160. Fujishima, A.; Zhang, X. T.; Tryk, D. A., TiO_2 Photocatalysis and Related Surface Phenomena. *Surf. Sci. Rep.* **2008,** *63* (12), 515-582.
161. Wong, H. S. P.; Lee, H. Y.; Yu, S. M.; Chen, Y. S.; Wu, Y.; Chen, P. S.; Lee, B.; Chen, F. T.; Tsai, M. J., Metal-Oxide RRAM. *Proc. IEEE* **2012,** *100* (6), 1951-1970.
162. Niemelä, J.-P.; Marin, G.; Karppinen, M., Titanium Dioxide Thin Films by Atomic Layer Deposition: A Review. *Semicond. Sci. Technol.* **2017,** *32*, 093005.
163. Ritala, M.; Leskela, M.; Nykanen, E.; Soininen, P.; Niinisto, L., Growth of Titanium Dioxide Thin Films by Atomic Layer Epitaxy. *Thin Solid Films* **1993,** *225* (1-2), 288-295.
164. Lee, Y.; George, S. M., Thermal Atomic Layer Etching of Titanium Nitride Using Sequential, Self-limiting Reactions: Oxidation to TiO_2 and Fluorination to Volatile TiF_4. *Chem. Mater.* **2017,** *29*, 8202-8210.
165. Blochl, P. E., Projector Augmented-Wave Method. *Phys. Rev. B* **1994,** *50* (24), 17953-17979.
166. Kääriäinen, M. L.; Kääriäinen, T. O.; Cameron, D. C., Titanium Dioxide Thin Films, Their Structure and its Effect on Their Photoactivity and Photocatalytic Properties. *Thin Solid Films* **2009,** *517*, 6666-6670.
167. Balasubramani, S. G.; Chen, G. P.; Coriani, S.; Diedenhofen, M.; Frank, M. S.; Franzke, Y. J.; Furche, F.; Grotjahn, R.; Harding, M. E.; Hättig, C.; Hellweg, A.; Helmich-Paris, B.; Holzer, C.; Huniar, U.; Kaupp, M.; Marefat Khah, A.; Karbalaei Khani, S.; Müller, T.; Mack, F.; Nguyen, B. D.; Parker, S. M.; Perlt, E.; Rappoport, D.; Reiter, K.; Roy, S.; Rückert, M.; Schmitz, G.; Sierka, M.; Tapavicza, E.; Tew, D. P.; Van Wüllen, C.; Voora, V. K.; Weigend, F.; Wodyński, A.; Yu, J. M., TURBOMOLE: Modular Program Suite for Ab initio Quantum-Chemical and Condensed-Matter Simulations. *J. Chem. Phys.* **2020,** *152*, 184107.
168. DuMont, J. W.; George, S. M., Pyrolysis of Alucone Molecular Layer Deposition Films Studied Using in Situ Transmission Fourier Transform Infrared Spectroscopy. *J. Phys. Chem. C* **2015,** *119*, 14603-14612.

169. Ferguson, J. D.; Yoder, A. R.; Weimer, A. W.; George, S. M., TiO_2 Atomic Layer Deposition on ZrO_2 Particles Using Alternating Exposures of $TiCl_4$ and H_2O. *Appl. Surf. Sci.* **2004,** *226* (4), 393-404.
170. Saric, I.; Peter, R.; Piltaver, I. K.; Badovinac, I. J.; Salamon, K.; Petravic, M., Residual Chlorine in TiO_2 Films Grown at Low Temperatures by Plasma Enhanced Atomic Layer Deposition. *Thin Solid Films* **2017,** *628*, 142-147.
171. Lii-Rosales, A.; Cavanagh, A. S.; Fischer, A.; Lill, T.; George, S. M., Spontaneous Etching of Metal Fluorides Using Ligand-Exchange Reactions: Landscape Revealed by Mass Spectrometry. *Chem. Mater.* **2021,** *Submitted*.